LAWRENCE
LIVERMORE
NATIONAL
LABORATORY

UCRL-TH-221650

Superconducting High Resolution Fast-Neutron Spectrometers

Ionel Dragos Hau

May 26, 2006

This work was performed under the auspices of the U.S. Department of Energy by University of California, Lawrence Livermore National Laboratory under Contract W-7405-Eng-48.

Superconducting High Resolution Fast-Neutron Spectrometers

by

Ionel Dragos Hau

GRAD (Technical Institute of Iasi) 1997

M.S. (University of California, Berkeley) 2002

A dissertation submitted in partial satisfaction of the requirements

for the degree of

Doctor of Philosophy

in

Engineering - Nuclear Engineering

in the

GRADUATE DIVISION

of the

UNIVERSITY OF CALIFORNIA, BERKELEY

Committee in charge:

Professor Jasmina Vujic, Chair

Professor Stanley Prussin

Professor Bernard Sadoulet

Doctor Stephan Friedrich

Spring 2006

The dissertation of Ionel Dragos Hau is approved:

Chair	Date
	Date
	Date
	Date

University of California, Berkeley
Spring 2006

Superconducting High Resolution Fast-Neutron Spectrometers

by
Ionel Dragos Hau

ABSTRACT

Superconducting High Resolution Fast-Neutron Spectrometers

by

Ionel Dragos Hau

Doctor of Philosophy in Engineering – Nuclear Engineering

University of California, Berkeley

Professor Jasmina Vujic, Chair

Superconducting high resolution fast-neutron calorimetric spectrometers based on ^{6}LiF and TiB_2 absorbers have been developed. These novel cryogenic spectrometers measure the temperature rise produced in exothermal (n, α) reactions with fast neutrons in ^{6}Li and ^{10}B-loaded materials with heat capacity C operating at temperatures T close to 0.1 K. Temperature variations on the order of 0.5 mK are measured with a Mo/Cu thin film multilayer operated in the transition region between its superconducting and its normal state. The advantage of calorimetry for high resolution spectroscopy is due to the small phonon excitation energies k_BT on the order of μeV that serve as signal carriers, resulting in an energy resolution $\Delta E \approx (k_BT^2C)^{1/2}$, which can be well below 10 keV.

An energy resolution of 5.5 keV has been obtained with a Mo/Cu superconducting sensor and a TiB_2 absorber using thermal neutrons from a ^{252}Cf neutron source. This resolution is sufficient to observe the effect of recoil nuclei broadening in neutron spectra, which has been related to the lifetime of the first excited state in ^{7}Li. Fast-neutron spectra obtained with a ^{6}Li-enriched LiF absorber show an energy resolution of 16 keV FWHM, and a response in agreement with the ^{6}Li(n, α)^{3}H reaction cross section and Monte Carlo

simulations for energies up to several MeV. The energy resolution of order of a few keV makes this novel instrument applicable to fast-neutron transmission spectroscopy based on the unique elemental signature provided by the neutron absorption and scattering resonances. The optimization of the energy resolution based on analytical and numerical models of the detector response is discussed in the context of these applications.

ACKNOWLEDGMENTS

This thesis has been an endeavor, which would have not been possible without the kind support of my professors, advisors, friends and family. I would like to thank first to those people in the Nuclear Engineering Department at UC Berkeley who made my studentship an enriching educational experience and who helped me see new avenues in my career: Profesor Jasmina Vujic, my academic adviser, Professor Stanley Prussin, and to Lisa Zemelman, the graduate secretary. I thank Professor Bernard Sadoulet in the Physics Department for his data analysis suggestions. My thanks go to the people in the University Relations Program (URP) and to my colleagues in the Advanced Detector Group at Lawrence Livermore National Laboratory (LLNL) who contributed to making this thesis possible. The SEGRF fellowship offered by LLNL was the most valuable resource that kept me on the right track with the project, so thank you Simon Labov, Harry Radousky and Paul Dickinson. My special thanks go to Stephan Friedrich, my research adviser at LLNL, for his enthusiasm and his tireless effort in guiding me with the experimental and theoretical work and to Thomas Niedermayr, with whom I spent most of the time working in the laboratory. Thank you Shafinaz Ali, Owen Drury, and Stephane Terracol, from whom I learned so much and thank you Jan Batteux for your technical support in the laboratory. I am indebted to Zane Bell and Arnold Burger for their experimental suggestions and for providing the detector materials. The help of Kris Petersen and Joanne Allen was invaluable in dealing with the administrative adventures at LLNL. In the end, my gratitude goes to my family in Romania and to my wife Claudia who all have encouraged and supported me, and prayed for me throughout my doctoral studies.

TABLE OF CONTENTS

LIST OF FIGURES

Chapter 1. Introduction

Chapter 2. Neutron Interactions in TiB_2 and LiF

Chapter 3. Calorimeter Theory

Chapter 4. Experimental Setup

Chapter 5. Experimental Results with a Prototype TiB_2 Absorber

Chapter 6. Fast-Neutron Spectroscopy with LiF absorbers

LIST OF TABLES

Chapter 1. Introduction

This chapter provides an overview of fast-neutron spectroscopy instrumentation along with their current applications and potential applications of instrumentation with high energy resolution. Fast neutron spectroscopy refers to measuring the kinetic energy of fast neutrons. These neutrons are measured either directly after emission from a source or after undergoing interactions inside a sample, and spectroscopy can be thus used to infer the properties of the source or of the intervening nuclei. This dissertation describes a novel fast-neutron spectrometer operated at very low temperatures, which offers high energy resolution and a simple response function, developed in the Advanced Detector Group at Lawrence Livermore National Laboratory. Applications of this technology are discussed in the context of the advantages of high energy resolution this novel instrument offers.

1.1 Fast-neutron spectrometers

Since its discovery in 1932 by J. Chadwick [Cha 32], various methods for detecting neutrons and measuring their kinetic energy have been devised [Kno 99], [Bro 02], [Peu 00]. Neutrons are usually detected by inducing nuclear reactions that produce energetic charged particles, and by collecting the resulting electrical charges or photons. The interaction of neutrons with nuclei is a complex process. It involves (n, n) elastic and (n, n') inelastic scattering, absorption by (n, α) reactions, radiative capture in (n, γ) reactions, charged particle reactions such as (n, p) or (n, ^{2}H), neutron-producing reactions such as (n, 2n) and (n, 3n) and nuclear fission reactions with heavy elements. Such interactions are characterized by energy-dependent microscopic neutron cross sections

$\sigma(E)$, in units of cm^2, that are unique for each neutron-nucleus pair [END 06]. The product of target nuclei number density N and $\sigma(E)$ is called the macroscopic cross section Σ and it has units of cm^{-1}. The macroscopic cross section Σ is a probability per unit path length that a neutron interacts with target material. The product between the neutron flux Φ in units of neutron/cm^2/s and Σ represents a reaction rate $R = \Phi\Sigma$ in units of reactions/cm^3/s.

Precise spectroscopy of fast neutrons with energy of order 1 MeV and above is challenging due to the fact that the interaction cross sections are only on the order of a few barns to tens of barns at best in this energy range, which significantly reduces the reaction rate and thus the detection efficiency.

An additional challenge for precise fast-neutron spectroscopy results from the fact that current instrumentation has either low energy resolution ΔE, or low detection efficiency, or that the response function is complicated.

Fast-neutron spectrometers based on organic scintillators (liquid or plastic) convert the kinetic energy of the neutron into visible light through a reaction that produces charged particles. For example, hydrogen-containing scintillators use the (n, p) reaction, which has a cross section of about 4.2 barns at 1 MeV. The energy deposited in the scintillator material by the recoil proton and the recoil nucleus is transferred through ionizations to electrical charges that excite the atoms and produce visible light photons collected with photomultiplier tubes. These instruments have among the highest detection efficiency for fast-neutrons but offer a resolving power $E/\Delta E$ only on the order of 10.

^{3}He gas proportional counters and ionization chambers employ the $^3He(n,p)^3H$ exothermal reaction to detect neutrons, with a reaction Q-value of 0.764 MeV. The

charges produced by the energetic reaction products are collected inside the chamber by electrically polarized electrodes. Designs that include an ion grid to prevent avalanche ion formation in an ionization chamber have better stability and provide an $E/\Delta E \sim 50$ for 1 MeV neutrons [Kno 99], [Bro 02]. The low ^{3}He number density in the gas contributes to low detection efficiency. The energy response of a ^{3}He gas detector is affected by the wall effect which is produced when the reaction products strike the chamber wall and deposit less energy in the gas. This results in a complicated response function that in addition is affected by the position of the neutron interaction inside the gas.

Organic scintillators and ^{3}He gas chambers collect either light or electrical charges produced by incoming neutrons. The energy resolution of scintillator detectors is limited by statistical fluctuations in both the number of the initial scintillation phonons and the number of the photoelectrons produced in the photomultiplier tube. The energy resolution of charge-collecting detectors is limited by the statistical fluctuations in the number of electrical charges collected.

An alternative method for neutron spectroscopy is based on determining the kinetic energy of the neutron $E_n = (1/2)m_n v_n^2$ from the measurements of the time-of-flight (TOF) that a neutron with a velocity $v_n = L/\Delta t$ takes to traverse a flight path of length L. A start moment is marked when the neutron is generated at the beginning of the flight path (source), while a highly efficient neutron detector (with detection area S) at the other end of the flight path is determining the arrival moment of the neutron. The precise measurement of the time of flight Δt can result in an resolving power $E/\Delta E >> 1000$, limited only by the practical flight path length. But the longer the flight path, the lower the solid angle $\Omega = S/4\pi L^2$ and thus the lower the total detection efficiency. For high

energy resolution applications, the TOF method is by far the most accurate technique, often employing flight paths with lengths of order of hundreds of meters [Col 98].

For an overview of fast-neutron spectrometers used today in various applications, one can plot their intrinsic detection efficiency versus the resolving power E/ΔE (Fig. 1.1). The 'ideal' neutron spectrometer would have 100% intrinsic detection efficiency and E/ΔE >> 1000.

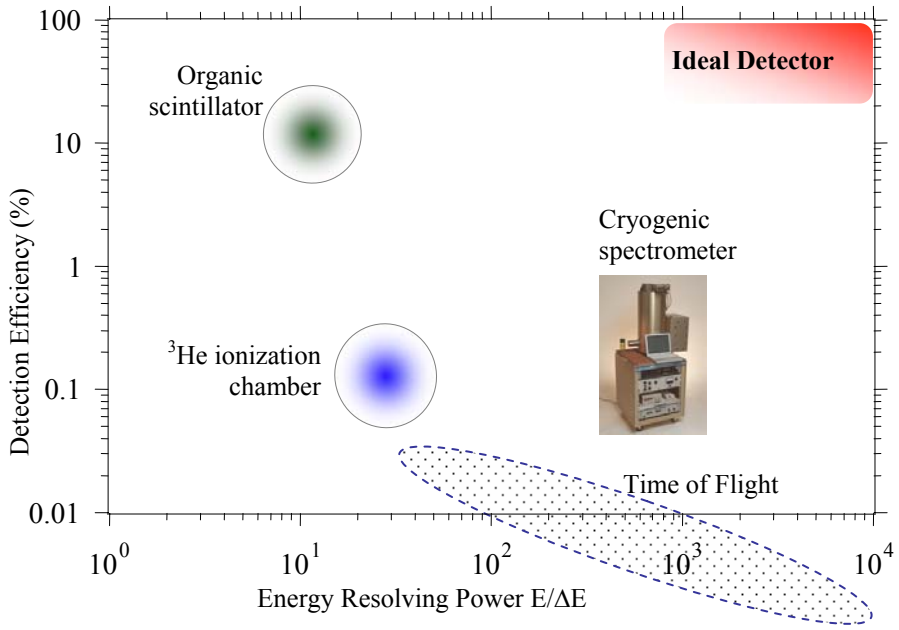

Figure 1.1. Neutron spectrometers comparison.

In this dissertation, we introduce a novel technique for fast-neutron spectroscopy. It is based on calorimetry, i.e. on measuring the energy of the fast-neutrons from the increase in the temperature of a material upon neutron absorption in an exoenergetic nuclear reaction. The Full Width Half-Maximum (FWHM) energy resolution of the calorimeter is given by [Mat 82]:

$$\Delta E_{FWHM} \approx 2.355(k_B T^2 C)^{1/2} \qquad (1.1)$$

where k_B is the Boltzmann constant, C is the heat capacity of the calorimeter and T is the operating temperature. In the case of a fast-neutron calorimeter, a theoretical energy resolution on the order of a few keV can be obtained by operating the calorimeter at $T \approx 0.1$ K with heat capacities of a few nJ/K. One of the advantages of the method is that it collects and measures heat (phonons), for which the excitation energy per signal carrier is much lower than for electrical charges or scintillation photons, which translates into improved energy resolution. On the other hand, in order to obtain high energy resolution, the detection system has to be operated at low temperatures.

1.2 Cryogenic radiation detectors

The idea of nuclear and atomic radiation spectroscopy by calorimetric methods is not new. As early as 1903, Curie used room temperature calorimetry to measure the heat produced by self-absorbed radiation from a radioactive sample [Cur 03]. The advantage of lowering the temperature of the absorber in order to obtain higher sensitivity was suggested in 1935 [Sim 35], while the possible use of the transition edge in a superconductor for radiometric purposes was first proposed in 1939 [Goe 39]. In 1942, Andrews et al. describe a bolometer to measure infra-red radiation with a tantalum sensor ($T_c = 4.48$ K) [And 42], and in 1949 Andrews also describes the use of superconducting 'columbium' strips (niobium) to detect α-particles from a polonium source [And 49]. As an interesting coincidence, the associated 'columbium' article was published next to a report about fast-neutron spectroscopy with ^{6}Li-loaded photographic emulsions. (Fig. 1.2).

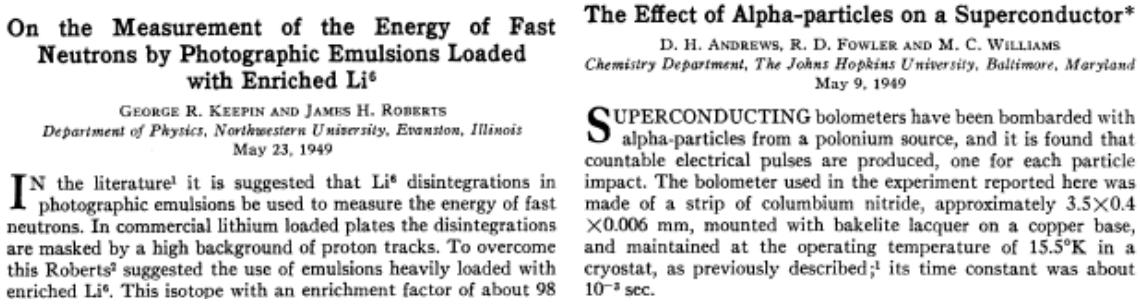

On the Measurement of the Energy of Fast Neutrons by Photographic Emulsions Loaded with Enriched Li^6

GEORGE R. KEEPIN AND JAMES H. ROBERTS
Department of Physics, Northwestern University, Evanston, Illinois
May 23, 1949

IN the literature[1] it is suggested that Li^6 disintegrations in photographic emulsions be used to measure the energy of fast neutrons. In commercial lithium loaded plates the disintegrations are masked by a high background of proton tracks. To overcome this Roberts[2] suggested the use of emulsions heavily loaded with enriched Li^6. This isotope with an enrichment factor of about 98

The Effect of Alpha-particles on a Superconductor*

D. H. ANDREWS, R. D. FOWLER AND M. C. WILLIAMS
Chemistry Department, The Johns Hopkins University, Baltimore, Maryland
May 9, 1949

SUPERCONDUCTING bolometers have been bombarded with alpha-particles from a polonium source, and it is found that countable electrical pulses are produced, one for each particle impact. The bolometer used in the experiment reported here was made of a strip of columbium nitride, approximately $3.5\times0.4\times0.006$ mm, mounted with bakelite lacquer on a copper base, and maintained at the operating temperature of 15.5°K in a cryostat, as previously described;[1] its time constant was about 10^{-3} sec.

Figure 1.2. The article by Andrews (right) in *Phys. Rev.* **76**, 154–155 (1949). Reproduced with permission from Physical Review.

In the following decades, both superconducting and semiconducting sensors have been developed as sensitive photon and particle detectors. In 1961, a gallium-doped single-crystal germanium bolometer operated at 2 K is described for infra-red and microwave applications [Low 61]. Experimental neutrino physics and dark matter searches in cosmology have motivated the development of cryogenic sensors since the early 1980's and have lead to the large underground experiments such as CDMS, CRESST and EDELWEISS [Ake 04], [Dru 84], [Fab 03], [Goo 85], [Pre 87], [Sad 99]. The field of x-ray astrophysics, that offers a window to understanding the high energy events in the universe, has driven the development of semiconducting and superconducting calorimeters [Bei 03], [Irw 95], [Mos 84], [Pol 04]. In the field of nuclear radiation metrology and particle spectroscopy, the work of de Marcillac et al. [Mar 93] focused on calorimeter development for dark matter research and for radiation metrology with LiF and silicon absorbers. An energy resolution of 16 keV FWHM is reported at a temperature of 35 mK, measured with a carbon resistor thermometer, but the measurements were limited to thermal neutrons and alpha particles. More recently, Silver et al. have reported an energy resolution of 39 keV FWHM obtained with LiF neutron

absorbers with NTD thermometer at 330 mK with a response to monoenergetic neutron beams with energies up to 7.2 MeV [Sil 02].

The Advanced Detector Group (ADG) at Lawrence Livermore National Laboratory (LLNL), is developing superconducting gamma and fast-neutron calorimeters for fundamental science and national security applications [Cho 00], [Cho 01], [Cun 02], [Ull 03], [Ter 04]. In our experiments, the temperature is measured with superconducting transition edge sensors (TES) as thermometers. Our goal is to develop a spectrometer with an energy resolution less than 0.1% for fast-neutrons up to 5 MeV kinetic energy with an efficiency of at least 1% for applications in fast-neutron resonance spectroscopy.

1.3 Motivation for high energy resolution in fast-neutron spectroscopy

High resolution neutron spectroscopy has applications in nuclear science, material characterization and nuclear non-proliferation [Kno 99], [Rei 91]. Fast neutrons with kinetic energies from fractions of keV to MeVs are emitted for example in deuterium-deuterium (D-D) and deuterium-tritium (D-T) fusion reactions and in spontaneous or induced fission reactions of ^{252}Cf or ^{235}U. Deuterium ions are accelerated by a potential of about 300 keV onto deuterium or tritium targets and produce monoenergetic neutrons with energies of 2.44 MeV (D-D reaction) and 14.1 MeV (D-T reaction). Neutrons emitted in fission reactions have continuous energy distributions that can be theoretically described by Maxwellian distribution [Cie 83].

Because the neutron has zero electric charge, in some cases it can penetrate deep into matter, somewhat similar to high energy gamma-rays. This property makes neutrons an attractive probing tool for determining the properties of matter. High resolution

measurements of the kinetic energy of the neutron provide information about the type of neutron source and about the properties of the intervening nuclei in the materials between the neutron source and the spectrometer. They can, for example, measure the spectral characteristics of (α, n) neutron sources such as ^{239}Pu/Be. The initial energy distribution of the neutron flux incident on any sample is altered by the neutron interaction with the nuclei in elastic and inelastic scattering or radiative capture interactions which have cross sections that present resonant structures. As a result, when examining the sample in transmission, fewer neutrons will be present with energies corresponding to the energy of the interaction resonances [END 06] (Fig. 1.3).

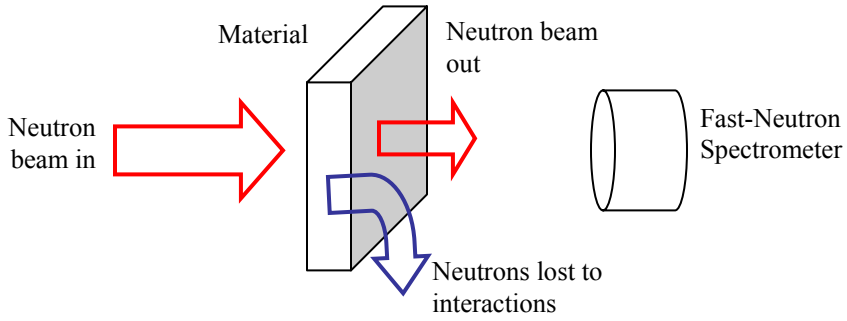

Figure 1.3. Schematic of the neutron transmission spectroscopy experiment.

A high resolution fast-neutron spectrometer allows the identification and quantification of certain low atomic number compounds by locating the position (centroid) and the amplitude (depth) produced by their neutron interaction resonances, in a fashion similar to high-resolution gamma-ray spectroscopy with a high purity Ge spectrometer. For each type of nucleus in the sample, the position and the depth of the associated resonances provide unique elemental signatures. These signatures of the neutron interactions in the sample and the associated detector can be modeled with numerical transport methods

such as Monte Carlo N-Particle (MCNP) code. This work uses the MCNP computer code versions 4C and Polimi [Bri 93], [Poz 03].

The following examples illustrate the potential of high energy resolution fast-neutron spectrometry to detect fissile materials, drugs and explosives based on the spectral signatures of the elements based on passive and active interrogation techniques [Rei 91]. In a first example, consider the presence of oxygen in a spherical plutonium sample with a diameter of 4 cm placed in free space. Neutrons emitted by spontaneous or induced fission of the Pu nuclei, interact with the Pu and O nuclei in the same sample and a fraction of them leak out of the sphere. Two different material compositions are independently simulated with MCNP: metallic Pu with 93% ^{239}Pu and 7% ^{240}Pu, which corresponds to the so called weapons grade plutonium and PuO_2, in which Pu isotopic composition is 93% ^{239}Pu and 7% ^{240}Pu and oxygen is 100% ^{16}O [Alb 97]. In both cases, the leakage spectrum is determined at the surface of each sphere. The simulation assumes that the neutrons are initially generated uniformly in the spherical volume, and they are spontaneously emitted by the ^{240}Pu isotope only with a Watt energy distribution given by $f(E) = \exp(-E/0.799)\sinh(4.903E)^{1/2}$ [Cie 83]. Due to the fissions with ^{239}Pu, the initial neutrons are multiplied with net multiplication factors of 1.46 for PuO_2 and of 2.33 for metallic Pu. No additional neutron production from (α, n) reactions with ^{16}O are simulated. The MCNP code tallies the neutrons that reach the surface of the sphere in an energy-dependent neutron flux averaged over the area of the sphere (F2 tally) in 500 energy bins of 10 keV each, in the energy range from 1 keV to 5 MeV. The error per energy bin is between 2% and 6%. The plot in Fig. 1.4 shows the leakage spectrum of the neutrons emitted per energy bin for both metallic Pu and PuO_2 in the energy range up to 4

MeV. The elastic cross section of ^{16}O is plotted on the same figure with the MCNP simulation in order to show the correspondence between the dips in the neutron spectrum of PuO_2 and the position of the resonances in ^{16}O. The neutron energy distribution from metallic Pu is closely described by the Watt distribution. In the case of PuO_2, the dips (troughs) in the spectrum are due to neutron interaction with ^{16}O. Neutron interaction resonances in ^{16}O result in creation of dips (troughs) in the spectrum at the location of a resonance, due to the higher interaction probability of the neutrons in this energy range.

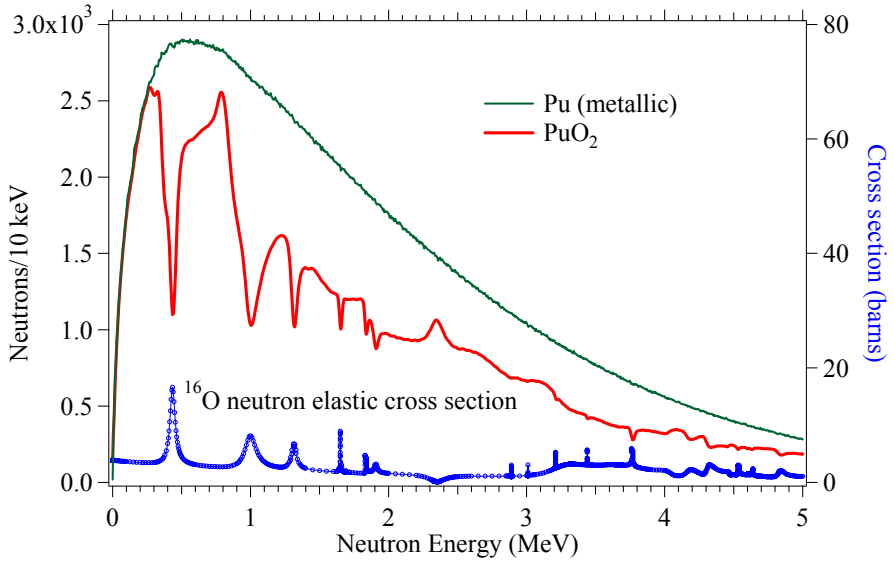

Figure 1.4. MCNP simulation of the neutron spectra of PuO_2 and metallic Pu. The elastic cross section of ^{16}O is included in the plot for comparison (bottom spectrum, right axis).

The ^{16}O resonances in Fig 1.4 have widths ranging from about 200 keV to a few keV. For low atomic number nuclei, the resonances are typically hundreds of keV apart and quantifying their effect in the leakage spectrum requires an energy resolution of a few keV. The amount of PuO_2 in mixed metallic Pu and PuO_2 samples can also be quantified with a high resolution instrument. This is illustrated in the MCNP simulation presented in Fig. 1.5, which considers a metallic Pu sphere with diameter of 2 cm, placed in free space. The Pu sphere has a thin layer of PuO_2 all over its surface and the leakage

spectrum is simulated over the area of the outer sphere. The ratio of PuO_2 layer volume to the total volume of the metallic Pu sphere results in a fraction f of PuO_2 by volume. The MCNP simulation considers three values of f, i.e. 1%, 10% and 20%, which corresponds to thicknesses of 0.13 mm, 0.64 mm and 1.12 mm of the PuO_2 layer.

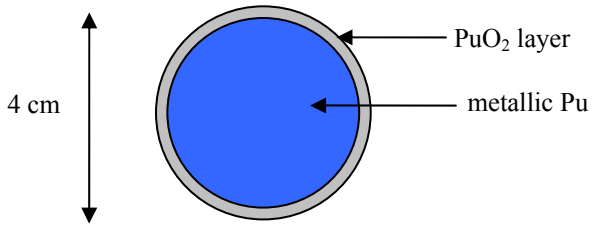

Figure 1.5. Simulation geometry of spherical metallic Pu sample with thin PuO_2 layer.

The isotopic composition of metallic plutonium is 94% ^{239}Pu and 6% ^{240}Pu. The initial Watt spectrum from ^{240}Pu is altered and the leakage spectrum shows that resonances due to oxygen do not produce any effect on the energy distribution when f = 2% but they become visible when f = 10% and f = 20% (Fig. 1.6).

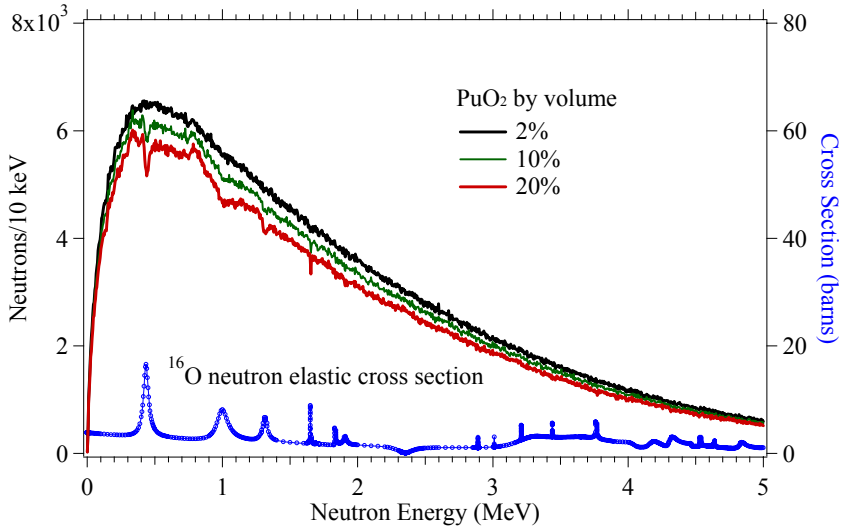

Figure 1.6. MCNP simulation of the neutron spectra of metallic Pu with different PuO_2 fractions. The elastic cross section of ^{16}O is included in the plot for comparison (bottom spectrum, right axis).

The resonances in ^{16}O have correspondents in the dips in the spectrum, which is more clearly observed for f = 20%. The additional dip in this spectrum at about 0.4 MeV is due to inelastic interaction with ^{239}Pu while the larger dip at about 0.7 MeV is due to inelastic interaction with ^{240}Pu.

The effect of shielding on the neutron spectrum of nuclear materials is is examined in the following simulation [Shu 00]. The neutron leakage spectrum of a spherical PuO_2 with a diameter of 4 cm shielded with a spherical shield of 5 cm of lead (Fig. 1.7) resembles the distribution of unshielded PuO_2 from Fig. 1.4, with the dips in the spectrum produced by ^{16}O at the same location (Fig. 1.8). The MCNP simulation assumes that both spheres with a total diameter of 14 cm are in free space.

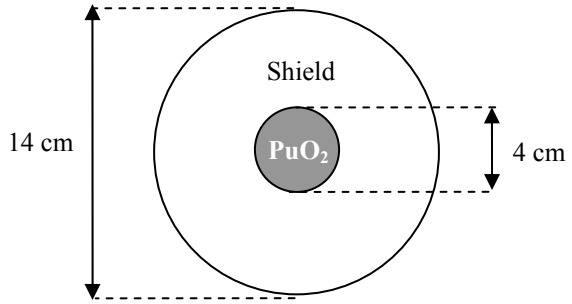

Figure 1.7. Simulation geometry of shielded PuO_2 sphere.

The isotopic composition of PuO_2 is 94% ^{239}Pu, 6% ^{240}Pu and 100% ^{16}O. The shield is assumed to be 100% ^{208}Pb. In this case, the energy bins are 5 keV wide, equivalent to an energy resolution of 25 keV FWHM. The leakage spectrum is shown in Fig 1.8 comparatively with the total interaction cross section of ^{208}Pb below 5 MeV. The interaction resonances from ^{208}Pb are densely-packed (51 resonances below 1 MeV) and the total cross section is dominated by elastic scattering. They have widths ranging from fractions of keV to about 30 keV and amplitudes up to about 80 barns. These resonances

alter the initial fission spectrum of ^{240}Pu significantly more than the oxygen nuclei in the unshielded PuO_2 sample. Resolving these resonances in the output spectrum requires energy resolution of at least on the order simulated with MCNP (25 keV FWHM).

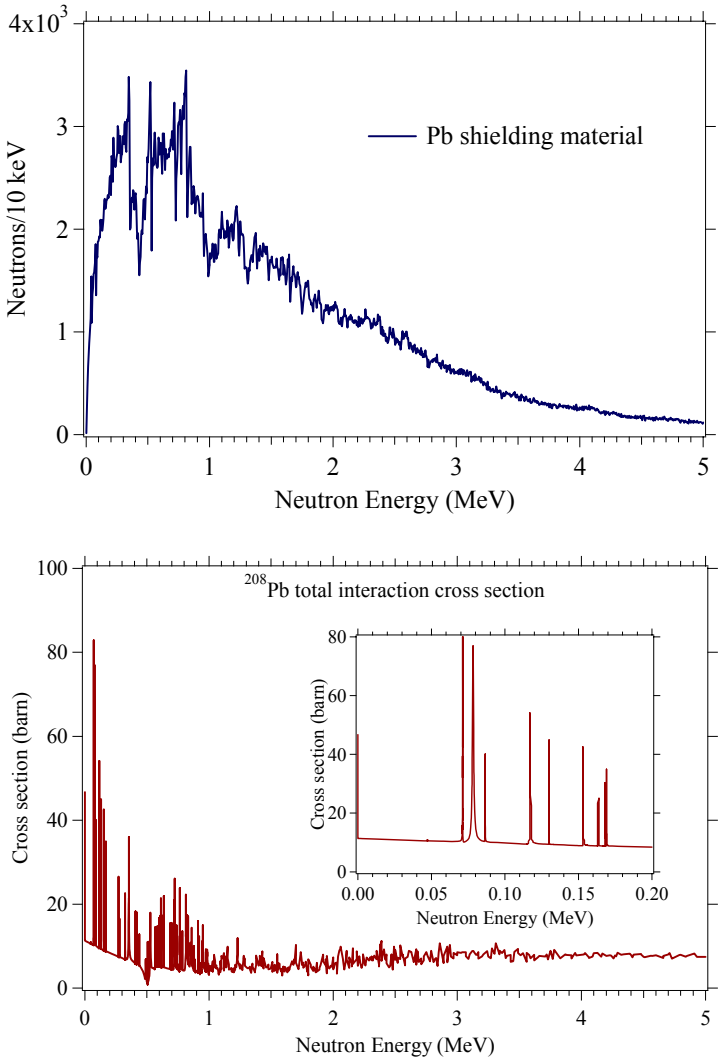

Figure 1.8. MCNP simulation of the effect of Pb shielding on the PuO_2 neutron spectrum for an instrumental energy resolution ΔE_{FWHM} = 25 keV (top). Total interaction cross section of ^{208}Pb (bottom) with insert showing the region below 0.2 MeV.

A second example showing the effect of the shielding around the spherical PuO_2 source consists of a spherical iron shield with thickness of 5 cm as shown in Fig. 1.7. The MCNP simulation assumes natural isotopic composition of iron, with ^{56}Fe having the

dominant abundance (97.6%), followed by ^{54}Fe (5.8%) and ^{57}Fe (2.1%). The isotopic composition of PuO_2 is 94% ^{239}Pu, 6% ^{240}Pu and 100% ^{16}O. The energy bins are 5 keV wide. The energy distribution of the neutron flux at the surface of the iron shield is shown in Fig 1.9 comparatively with the total interaction cross section of ^{56}Fe below 5 MeV.

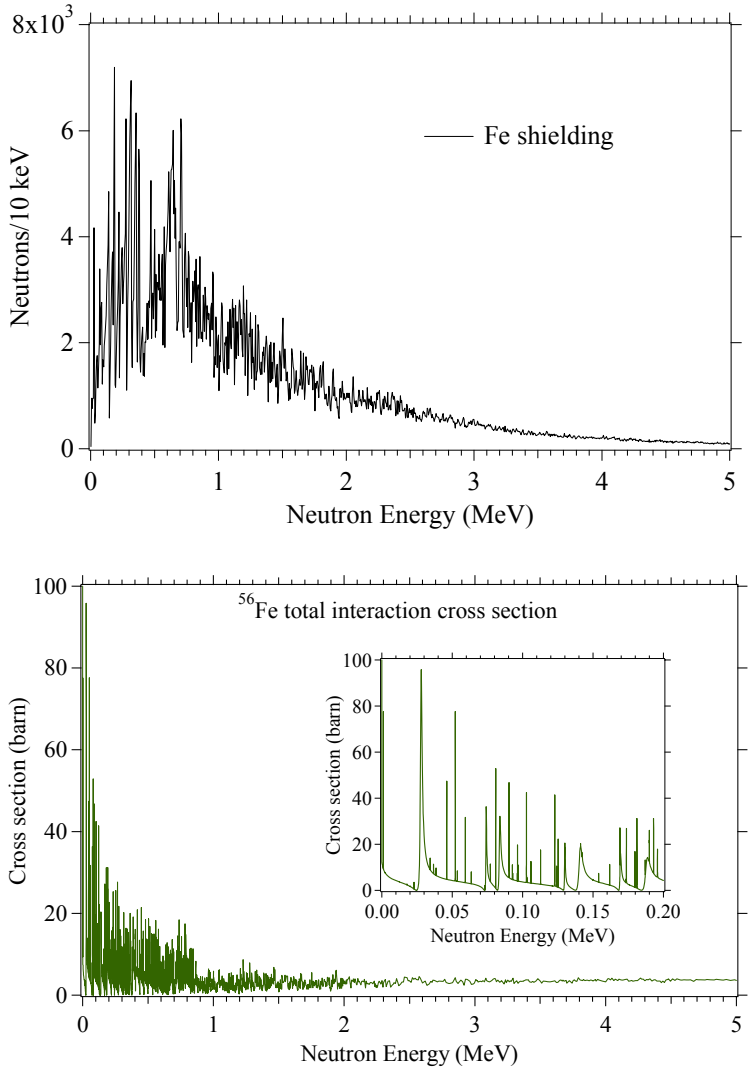

Figure 1.9. MCNP simulation of the effect of Fe shielding on the PuO_2 neutron spectrum for an instrumental energy resolution ΔE_{FWHM} = 25 keV (top). Total interaction cross section of ^{56}Fe (bottom) with insert showing the region below 0.2 MeV.

The iron shield produces large fluctuations in the output flux due to the interaction resonances from ^{56}Fe, which are even more densely-packed than in ^{208}Pb (192 resonances below 1 MeV) and are dominated by elastic scattering. Similarly to ^{208}Pb, the resonances in ^{56}Fe have widths ranging from fractions of keV to about 30 keV and amplitudes up to about 100 barns. These resonances alter the initial fission spectrum of ^{240}Pu significantly more than the ^{16}O nuclei in the unshielded PuO_2 sample. In this case, even if the errors are between 4% and 7% per energy bin, it is difficult to visualize the effect of the resonances from ^{56}Fe. Resolving these resonances in the output spectrum is nevertheless challenging and it requires energy resolution of at least on the order simulated with MCNP (25 keV FWHM).

The last example in this Section that illustrates potential applications of high resolution fast-neutron spectrometry is obtained from MCNP simulations of materials containing C, N and O having natural isotopic composition. The simulation geometry assumes a cylindrical target 6 cm in diameter with a height of 5 cm, oriented in the direction of the y-axis (Fig. 1.10). An ideal monodirectional neutron beam irradiating the sample is simulated in MCNP assuming that neutrons are generated on the input surface in the positive direction of the y-axis and that they have uniform energy distribution form zero to 4 MeV.

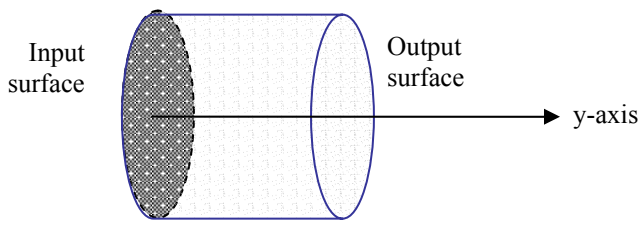

Figure 1.10. MCNP simulation geometry for materials containing C, N and O.

The effect of the sample is studied by determining the characteristics of the transmitted neutron beam at the other end of the cylinder. MCNP tallies the neutrons that reach the output surface of the cylinder in an energy-dependent neutron flux averaged over the circular output area (F2 tally) in 400 energy bins of 10 keV each, in the energy range from 1 keV to 4 MeV. Three different materials with natural isotopic composition have been simulated: TNT (explosive) with chemical formula $C_6H_2CH_3(NO_2)_3$, cocaine (drug) with chemical formula $C_{17}H_{21}NO_4$ and water (reference material) with chemical formula H_2O [Lid 99]. The effect of these materials on the input neutron spectrum is shown in Fig. 1.11. The errors are on the order of 4% per each 10 keV energy bin.

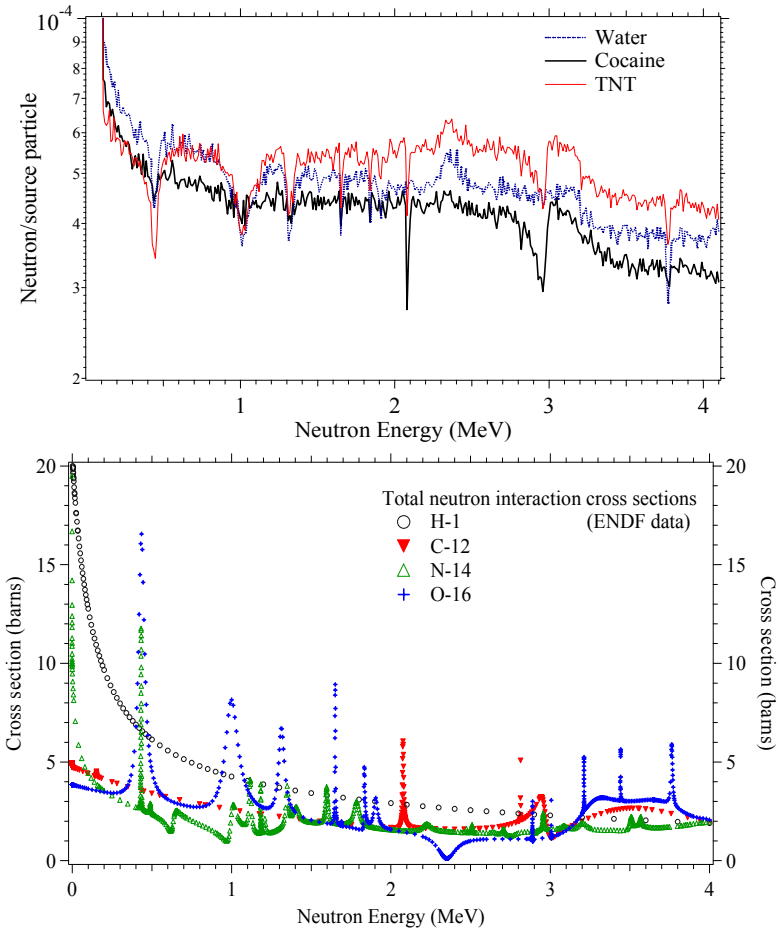

Figure 1.11. Top: MCNP simulation of neutron transmission spectroscopy in samples containing low atomic number elements (H, C, N, O). Bottom: Neutron interaction cross sections for ^{12}C, ^{14}N and ^{16}O. The cross section of ^{1}H (with no resonances) is included for comparison. Data from ENDF [END 06].

The total interaction cross sections in Fig. 1.12 are dominated by elastic scattering with cross sections on the order of a few barns. Inelastic interaction cross sections have minor contribution to the total cross section below 4 MeV, mostly due to ^{14}N which has the first excited state at 2.3 MeV with $\sigma_{(n, n')} \approx 0.01$ barns, while C and O have their first excited states at energies above 4 MeV. The neutron thermalizing effect of each compound is reflected in the energy spread at energies below 300 keV, with water showing stronger neutron thermalization effect than TNT or cocaine. However, resolving the resonances in the output spectrum requires an energy resolution of at least on the order simulated with MCNP (25 keV FWHM), which can be used to identify C, N and O compounds based on the relative amplitude of the dips in the neutron spectrum, eventually in conjunction with gamma-ray spectrometry [Goz 95], [Lov 95]. Similar approaches to using the scattering resonances of low-Z elements for compound identification are based on fast-neutron resonance spectroscopy with imaging capabilities but with no energy resolution capability [Che 02].

All these examples based on MCNP simulations illustrate the potential of neutron resonance spectroscopy for characterizing the neutron source and some of the low-Z and high-Z materials in the vicinity of the source [Rei 91. The wide resonances could be identified with active or passive interrogation techniques with a 'classical' neutron spectrometer such as a ^{3}He detector or organic scintillator with energy resolution on the order of tens of keV, but the identification of resonances with widths on the order of 5-10 keV or lower, requires higher energy resolution.

1.4 Thesis Outline

This thesis presents the theory, the design and the performance of neutron spectrometers based on exothermic (n, α) reactions in ^{10}B and ^{6}Li compounds, currently under development in the Advanced Detector Group at Lawrence Livermore National Laboratory. The initial motivation for this work is in the area of fast-neutron resonance spectroscopy. Future applications that can benefit from high energy resolution lie in the areas of nuclear physics and nuclear data (direct energy level measurements, delayed neutrons experiments), nuclear waste management, or in the area of neutron dosimetry for radiation therapy or astrobiology (astronaut doses).

Chapter 2 of this thesis discusses neutron interaction cross sections in TiB_2 and LiF together with MCNP simulations of neutron transport in these materials in order to predict the spectral response in the thermal and MeV energy ranges.

Chapter 3 contains the time-domain and frequency-domain analysis of the electro-thermal models of the simple and composite calorimeters in order to understand the pulse formation and the noise components that limit the energy resolution of the fast-neutron calorimeters.

Chapter 4 describes the experimental setup that includes the fabrication and installation of the absorbers, the readout electronics, and the cryogenic apparatus for generating low temperatures.

Chapter 5 presents neutron spectra obtained with a prototype TiB_2 absorber irradiated with thermal neutrons for characterizing its energy resolution. These spectra have been analyzed to determine the lifetime of the first excited state in ^{7}Li from the broadening of the 2.31 MeV line in TiB_2.

Chapter 6 focuses on optimizing the energy resolution of large volume ^{6}LiF-based neutron spectrometers. The experimental results are compared with MCNP simulations to identify spectral features and to determine the limiting energy resolution of the instrument. The measured spectrum can be deconvolved through the response matrix of the detector to reconstruct the input energy spectrum. This study also shows the possibility to increase the efficiency of the spectrometer by adjusting the thermal parameters of the detector with no significant degradation in energy resolution.

Chapter 7 summarizes the results and outlines possible future development to increase the spectrometer sensitivity.

Chapter 2. Neutron Interactions in TiB_2 and LiF

Neutrons are generally detected indirectly through nuclear reactions that result in emission of prompt energetic particles or through the transfer of some of their kinetic energy to recoil nuclei. Both the reaction products and the recoiling nuclei ionize the material surrounding the interaction point. Exoergic nuclear reactions release heavy charged particles with a range of a few tens of micrometers that can be completely stopped inside an absorber. One such exoergic reaction is the (n,α), which in some cases releases the reaction energy (Q-value) on the order of a few MeV. The energy liberated in the X(n, α)Y reaction by the nuclei with mass m is:

$$Q = (m_n + m_X - m_\alpha - m_Y)c^2 \tag{2.1}$$

where c is the speed of light.

The energy deposited in the absorber following (n,α) reaction is the sum of the Q-value and the kinetic energy E_n of the neutron:

$$E_{deposited} = E_n + Q \tag{2.2}$$

With Q-value on the order of a few MeV, it is possible to discriminate between gamma rays and neutrons since the neutron response will be shifted towards higher energy by the amount of the Q-value. This is of particular interest since fission neutron sources also emit gamma rays, usually in much higher proportion [Cie 83]. Ideally, the total energy from (n, α) reaction is completely deposited inside the absorber and measured so that:

$$E_{measured} = E_{deposited} \tag{2.3}$$

2.1 Neutron reactions and cross sections for TiB_2 and LiF

Exothermal (n,α) reactions of interest are with ^{6}Li and ^{10}B isotopes. These isotopes are used for the conversion of both slow (thermal) and fast neutrons into detectable particles [Kno 99]. The reactions are $^{10}B(n, \alpha)^{7}Li$, with Q = 2.79 MeV and $^{6}Li(n, \alpha)^{3}H$, with Q = 4.782 MeV. About 94% of all $^{10}B(n, \alpha)^{7}Li$ reactions lead to the first excited state of ^{7}Li at 478 keV, while the remaining 6% produce ^{7}Li in its ground state. The excited state of ^{7}Li decays promptly with the emission of 478 keV gamma-rays. In the $^{6}Li(n, \alpha)^{3}H$ reaction there is no branching and ^{3}H is produced in the ground state.

Besides the neutron detectors described in Chapter 1, the (n,α) reactions with ^{10}B and ^{6}Li isotopes are employed in various instruments such as BF_3 (gas) proportional tubes, boron-lined counters (solid coating), or boron-loaded plastic scintilators. Lithium-loaded scintillators such as LiI crystals doped with Eu and scintillators obtained by incorporating Li into glass have widespread applications. These materials can be used either with the natural isotopic composition of ^{10}B (19.9%) and ^{6}Li (7.6%) or they can have these two isotopes enriched to levels close to 90-95%. In any case, there is a wide selection of available boron and lithium compounds that can be used for fast-neutron spectroscopy [Bel 05], [Peu 00]. In selecting a neutron absorber compound, the (n,α) reaction should be dominant and the average atomic number Z of the compound should be low in order to reduce gamma-ray absorption.

In particular, LiF and TiB_2 compounds have been tested as neutron absorbers because they are stable, solid state materials that pose no hazards. These two compounds have been chosen because of their ^{6}Li and ^{10}B content, with large (n, α) reaction cross sections [END 06]. Additionally, the isotopic content of ^{6}Li and ^{10}B in LiF and TiB_2 can be

increased by enriching the natural isotopic composition with factors of 5 to 12 to about 90 – 95%, which ensures an increased (n, α) reaction rate per unit volume of absorber. A selected set of physical parameters for LiF and TiB_2 is presented in Table 2.1.

Table 2.1. Isotopic composition and physical parameters of TiB_2 and LiF

Parameter	**TiB_2**	**LiF**
Natural isotopic composition (% per atom type)	^{46}Ti (8.2), ^{47}Ti (7.4), ^{48}Ti (73.8), ^{49}Ti (5.4), ^{50}Ti (5.2) ^{10}B (19.9), ^{11}B (80.1)	^{6}Li (7.6), ^{7}Li (92.4) ^{19}F (100)
Density ρ (g/cm^3)	4.52	2.64
Number density N(nuclei/cm^3)	6.13×10^{22}	3.37×10^{22}
Molar mass M (g/mol)	69.50	25.93

In this Chapter, we present a summary of the neutron reactions in LiF and TiB_2, including the (n, α) reactions, and the expected detector response to neutrons. However, besides the (n, α) reaction, there are other reactions such as elastic and inelastic scattering, and radiative capture that influence the energy deposition in the detector. The reactions that we will focus on in this Chapter, are summarized in Table 2.2, where ${}^{A}_{Z}X$ represents the nucleus with atomic mass number A and atomic number Z .

Table 2.2. Reactions of importance for energy deposition in the absorber

Neutron Reaction	**Microscopic cross section**	**Reaction formula**	**Energy deposition**
(n,α)	$\sigma_{(n,\alpha)}$	${}^{1}_{0}n+{}^{A}_{Z}X\rightarrow{}^{4}_{2}He+{}^{A-3}_{Z-2}Y+Q$	complete
Elastic scattering (n, n)	$\sigma_{(n,n)}$	${}^{1}_{0}n+{}^{A}_{Z}X\rightarrow\left({}^{A+1}_{Z}X\right)^{*}\rightarrow{}^{1}_{0}n+{}^{A}_{Z}X$	partial
Inelastic scattering (n, n')	$\sigma_{(n,n')}$	${}^{1}_{0}n+{}^{A}_{Z}X\rightarrow\left({}^{A+1}_{Z}X\right)^{*}\rightarrow{}^{1}_{0}n+{}^{A}_{Z}X+\gamma$	partial
Radiative capture (n, γ)	$\sigma_{(n,\gamma)}$	${}^{1}_{0}n+{}^{A}_{Z}X\rightarrow\left({}^{A+1}_{Z}X\right)^{*}\rightarrow{}^{A+1}_{Z}X+\gamma$	partial

The total interaction cross section $\sigma_{(n,\,total)}$ is given by:

$$\sigma_{(n,\,total)}=\sigma_{(n,\alpha)}+\sigma_{(n,n)}+\sigma_{(n,n')}+\sigma_{(n,\gamma)}+\ldots \tag{2.4}$$

The elastic and inelastic scattering reactions involve the re-emission of neutrons with lower energy, while radiative capture reactions result in the emission of gamma rays.

2.1.1 Characteristics of (n,α) reactions with ^{6}Li and ^{10}B

The expected detector response to thermal neutrons is sketched in Fig. 2.1 for TiB_2 and LiF, with the peaks located at the Q-values of the reactions. Fast neutrons with kinetic energy E_n are producing shifted pulses at a deposited energy $E_{deposited} = E_n + Q$. The shift in energy is shown only for the $^{6}Li(n, \alpha)^{3}H$ reaction. Due to the simple response to neutrons and the high Q-value, the reaction with ^{6}Li provides a simple spectral unfolding which on the first order depends only on the (n, α) reaction cross section.

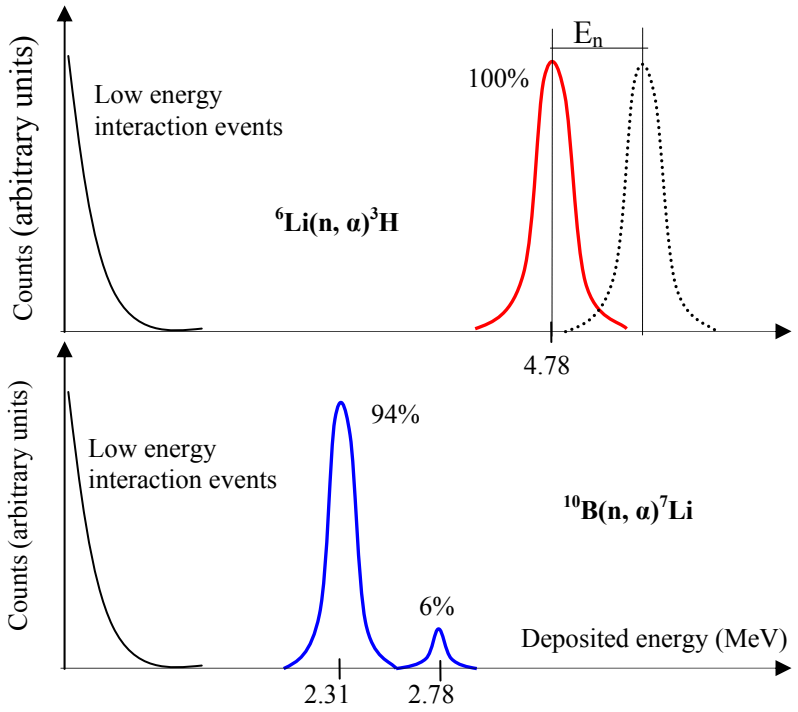

Figure 2.1. Expected response to thermal neutrons shown at the Q-value for each reaction. Fast neutrons produce a shift in the response with an amount E_n (top sketch).

In the neutron reaction with ^{10}B, the response is more complicated than in the case of ^{6}Li due to the branching into two reaction channels. For this reason, TiB_2 is more suitable for characterizing the energy resolution of a calorimetric spectrometer by using thermal neutrons. Thus, LiF is the absorber of choice for fast-neutron spectroscopy because of its single Q-value.

Figure 2.2-A shows the cross sections for $^{6}Li(n, \alpha)^{3}H$ and $^{10}B(n, \alpha)^{7}Li$ reactions as function of neutron energy [Kno 99], [END 06]. The fast-neutron region of the cross section is presented in detail in Fig. 2.2-B.

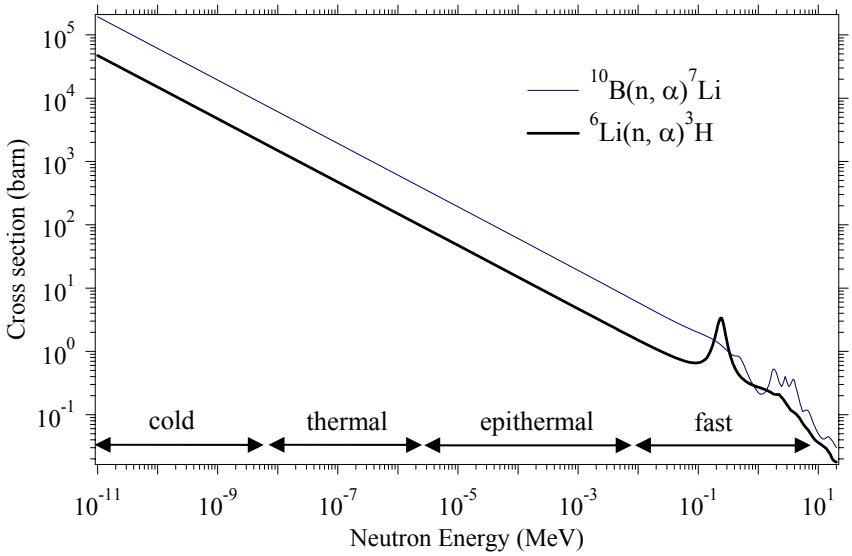

Figure 2.2-A. (n, α) reaction cross sections over the energy range available in literature.

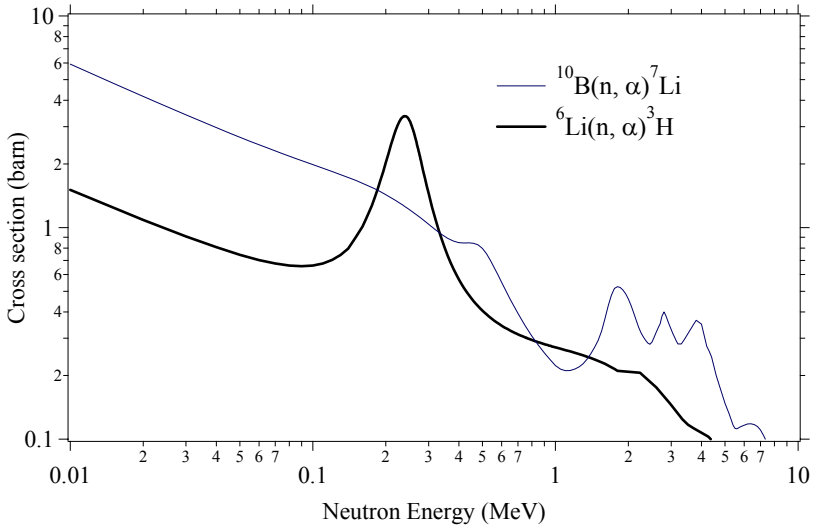

Figure 2.2-B. The resonant absorption structures above 10 keV, in the fast neutron region (from Fig 2.2.A.)

At thermal (~ 25 meV) and epithermal neutron energies, $\sigma_{(n,\alpha)}(E) \sim E^{-1/2}$ is on the order of thousands of barns and no resonance structure is present up to about 100 keV. In the

energy range above 10 keV, which is considered the fast-neutron region, the average cross-section is on the order of a few barns.

2.1.2 Elastic and inelastic scattering interaction mechanisms

In order to understand the energy deposition mechanisms, two fundamental interactions are being considered: elastic (potential) scattering and compound nucleus formation which results in elastic and inelastic interactions [Lam 66], [Dud 76]. Elastic (potential) scattering of the neutron on a nucleus occurs with neutrons of any energy. This is a process in which both the kinetic energy and the total momentum are conserved, similar to the collision process of two billiard balls. The neutron with initial kinetic energy E_n does not penetrate the ${}^{A}_{Z}X$ nucleus, which remains in its ground state and it behaves like a single rigid body. The maximum energy loss occurs in a head-on collision, which results in a neutron with kinetic energy $\left(E_n^{'}\right)_{potential}$ and a recoil nucleus with kinetic energy $E_{recoil}^{'}$ described by:

$$\left(E_n^{'}\right)_{potential} = \left(\frac{A-1}{A+1}\right)E_n \quad \text{and} \quad E_{recoil}^{'} = \frac{4A}{(A+1)^2}E_n \tag{2.5}$$

After the interaction, the energy $E_n = \left(E_n^{'}\right)_{potential} + E_{recoil}^{'}$ is deposited in the material if, for example, the neutron is absorbed in an (n, α) reaction and the recoil nucleus deposits the energy $E_{recoil}^{'}$ in a short range on the order of a few μm. For neutron energies above a threshold at $E_{n,min} = [(A+1)^2/4A]Q$, the energy deposited by the recoil nucleus has the same value as the Q-value of the (n, α) reaction, which can interfere with the energy deposited at the Q-value. For ^{6}Li, ^{7}Li and ^{19}F, this interference occurs for neutron

energies above 9.5 MeV, while for ^{10}B, ^{11}B and Ti isotopes, the energy deposited by the recoil ion becomes significant for neutron energies above 7 MeV.

If the neutron is absorbed by the ${}^{A}_{Z}X$ nucleus, a compound nucleus ${}^{A+1}_{Z}X$ is formed (Fig. 2.3).

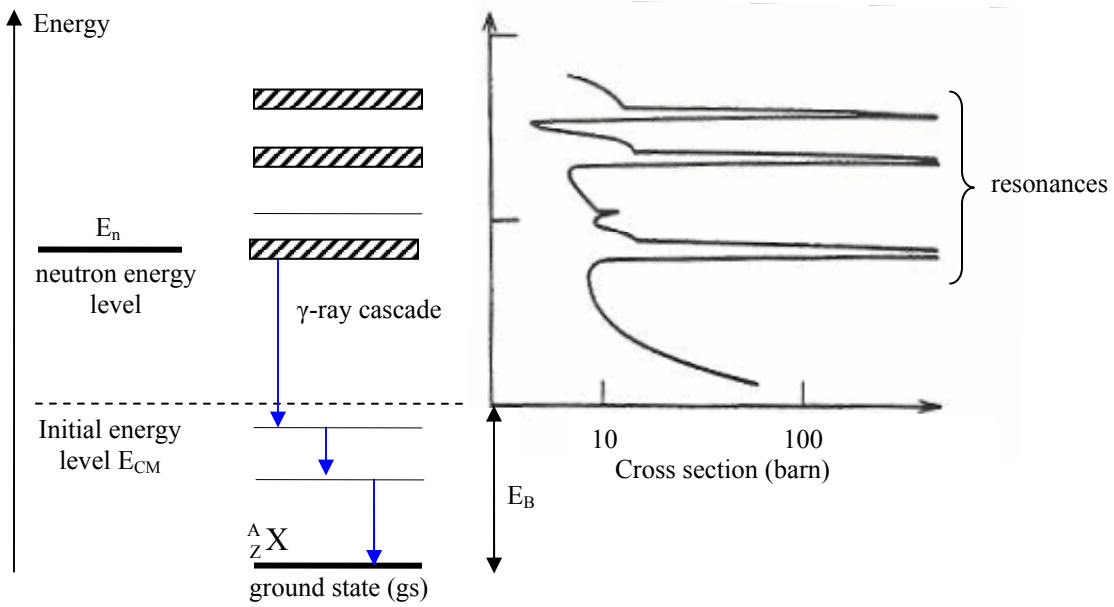

Figure 2.3. Compound nucleus energy level diagram (from [Dud 76]).

From the conservation laws for momentum and energy, the total kinetic energy in the center-of-mass system is $E_{CM} = (A/A+1)E_n$. The energy E_{CM} plus the binding energy E_B of the neutron is brought into the compound nucleus system, which is excited at $E_{CM} + E_B$ above its ground level. The probability for the formation of the compound nucleus is very high for certain neutron energies, which corresponds to interaction resonances (Fig. 2.3). The compound nucleus decays to its ground state by three possible ways: gamma-ray emission in cascade (radiative capture), by emission of another neutron or by emission of a group of nucleons. In the case of radiative capture, the time scale of the decay process from each energy level is described by the mean lifetime $\tau = \hbar / \Gamma_i$ which depends on the

width Γ_i of each energy level E_i, where ħ is the reduced Planck constant h/2π. For prompt gamma-ray emission with $\tau \approx 10^{-15} - 10^{-12}$ s, Γ_i is between a few meV to a few eV.

Reactions that results in the re-emission of the neutron are:

a) elastic neutron scattering, when the neutron is re-emitted and the residual ${}^{A}_{Z}X$ nucleus is returned to the ground state. In this case, the kinetic energy $\left(E_n^{'}\right)_{elastic}$ of the outcoming neutron is calculated from the conservation of the linear momentum and energy for a projectile (neutron) and a target (${}^{A}_{Z}X$ nucleus) at rest in the laboratory coordinate system. The energy distribution is influenced by the large interaction cross sections in the vicinity of the energy levels in the compound ${}^{A+1}_{Z}X$ nucleus. As a result, the elastic scattering cross section shows distinct resonances at neutron energies close to the energy levels in the ${}^{A+1}_{Z}X$ nucleus. An example of such resonances is presented in Fig 2.3. An elastically-scattered neutron that is subsequently absorbed in an (n, α) reaction deposits an energy equal to Q + $\left(E_n^{'}\right)_{elastic}$, while the recoil nucleus deposits its kinetic energy in a short range on the order of a few μm.

b) inelastic neutron scattering, in which the residual ${}^{A}_{Z}X$ nucleus is left in an excited state with energy E_{ex}, followed by the emission of gamma-rays if the transition rules permit it. This is an endoergic reaction, and, at the threshold, inelastic neutron scattering occurs when $E_{CM} \geq E_{ex}$. In the laboratory system, this reaction takes place if the neutron has at least an energy $E_{threshold} \geq [(A+1)/A]E_{ex}$. Neutrons with E_n above the threshold are re-emitted with kinetic energies $\left(E_n^{'}\right)_{inelastic} = E_n - [(A+1)/A]E_{ex.}$ If $E_n = E_{threshold}$, the initial energy of the neutron is used to excite the energy level at E_{ex} and the

neutron is re-emitted with kinetic energy close to zero which have higher probability to be captured or to participate in an (n, α) reaction releasing an energy $Q + \left(E_n^{'}\right)_{inelastic}$.

2.1.3 Resonant elastic and inelastic scattering and radiative capture cross sections

The microscopic cross sections described previously for low-energy neutron spectroscopy are presented for the naturally-occurring isotopes in LiF and TiB_2, with data from [END 06]. The total inelastic neutron scattering cross section $\sigma_{inelastic}$ is obtained as a sum over the inelastic interaction cross sections of the corresponding every energy level in the nucleus:

$$\sigma_{inelastic} = \sigma_{(n,n')1} + \sigma_{(n,n')2} + \sigma_{(n,n')3} + \ldots \quad (2.6)$$

Up to about 100 keV, the total interaction cross section in ^{6}Li (Fig. 2.4) is dominated by the (n, α) reaction, as shown in Fig. 2.2-A. The elastic scattering cross section has a constant value below 100 keV and then a resonance in the 240 keV region. The threshold for the inelastic scattering is reached at E_n = 1.75 MeV, which corresponds to the first excited state at 1.5 MeV in ^{6}Li, produced by the (n, n') reaction.

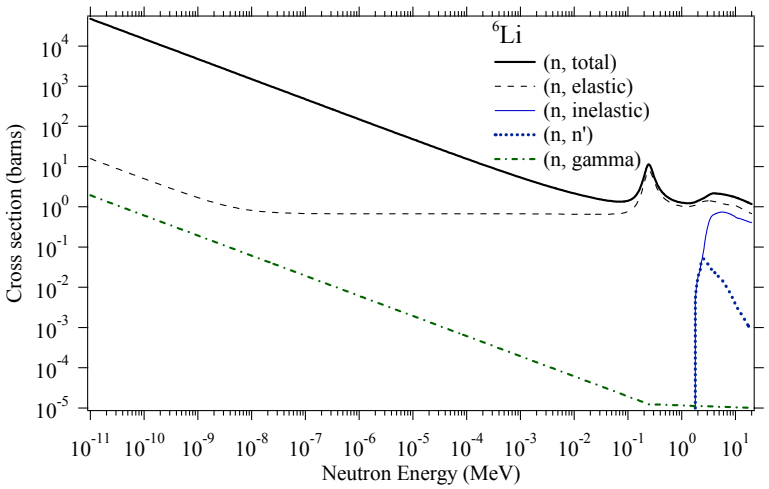

Figure 2.4. Neutron interaction cross sections in ^{6}Li.

Other (n, n') cross sections corresponding to superior energy levels (2, 3, ...) in ^{6}Li are included in Fig. 2.4 in the (n, inelastic) cross section. The radiative (n, gamma) capture cross section is larger in the thermal region and it is on the order of a few μbarn in the MeV region which results in very low gamma ray emission from ^{6}Li.

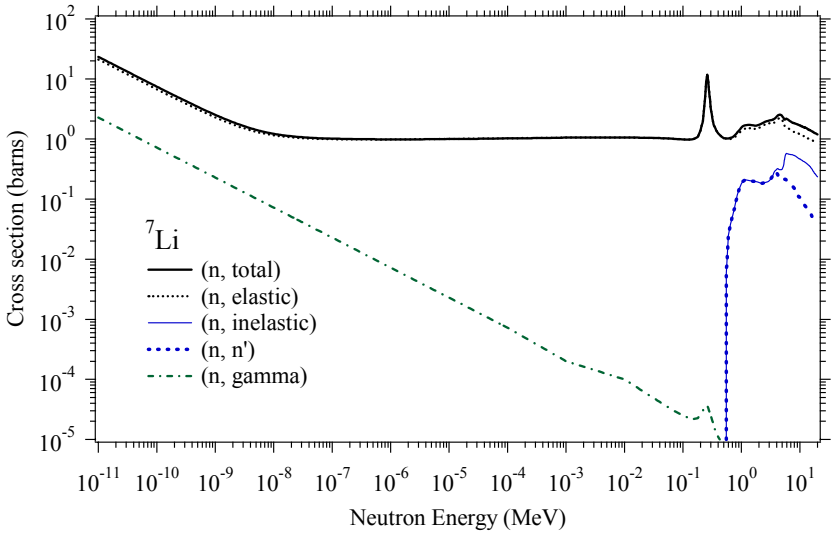

Figure 2.5. Neutron interaction cross sections in ^{7}Li.

The total interaction cross section in ^{7}Li is dominated by elastic scattering (Fig. 2.5). The inelastic scattering threshold is located at E_n = 0.546 MeV which corresponds to the first excited state at 0.477 MeV. The radiative capture cross section is similar to that in ^{6}Li, being on the order of μbarns the MeV region.

The cross sections of ^{19}F are more complex than for Li isotopes (Fig. 2.6). The elastic cross section dominates over the total cross section, with a few notable resonances located at 27.1, 49.0 and 98 keV respectively with a maximum cross section of 127 barns. The inelastic component has cross sections about two to three orders of magnitude lower, with a sharp edge at E_n = 116.2 keV, corresponding to the first excited level at 109.9 keV. The second excited energy level in ^{19}F (not shown in Fig. 2.6) is located at 197.1 keV,

which corresponds the threshold at E_n = 207.5 keV. The radiative capture cross section is of 0.5 barn for thermal neutrons and it peaks at the resonance at 27.1 keV. By comparison with the smooth cross sections from ^{6}Li and ^{7}Li, the resonant structures in ^{19}F can significantly alter the neutron energy distribution in LiF absorbers.

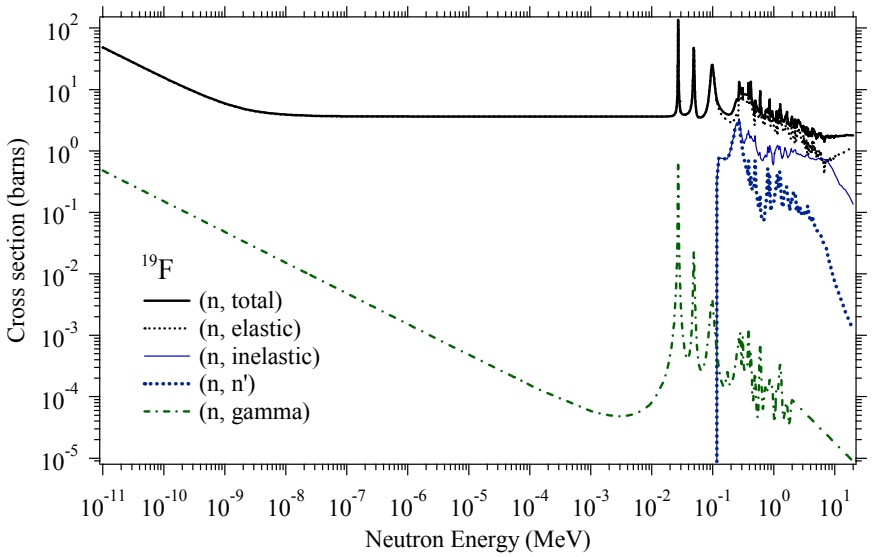

Figure 2.6. Neutron interaction cross sections of ^{19}F.

In TiB_2, the ^{10}B, ^{11}B, ^{46}Ti and ^{48}Ti isotopes are being considered. Similarly to ^{6}Li, the total interaction cross section in ^{10}B (Fig. 2.7) is dominated by the (n, α) reaction, as shown also in Fig. 2.2-A. Above about 100 keV, the elastic interaction cross section is dominant over the inelastic and radiative capture cross sections. The first excited level in ^{10}B at 0.718 MeV produces the threshold in the inelastic cross section at E_n = 0.790 MeV.

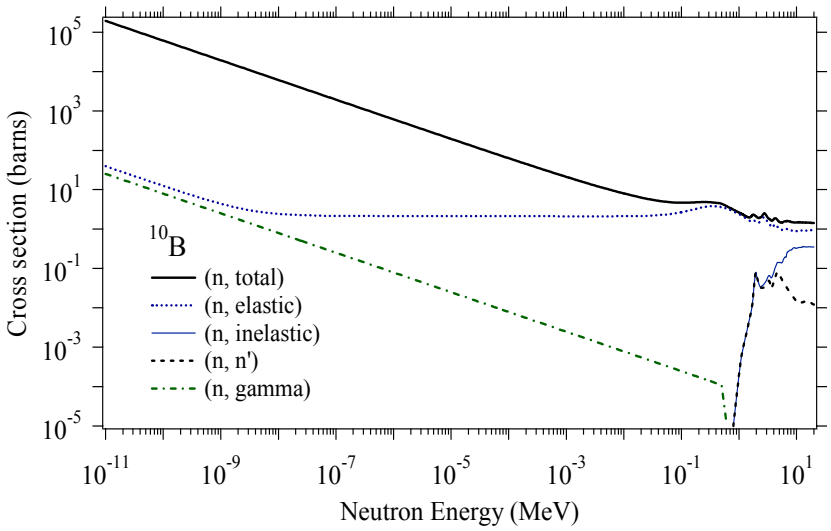

Figure 2.7. Neutron interaction cross sections of ^{10}B.

In ^{11}B, the cross section is dominated by elastic scattering (Fig. 2.8). The radiative capture cross section shows a narrow peak at about 20 keV. The inelastic scattering cross section has a sharp edge at E_n = 2.32 MeV, corresponding to the first excited state at 2.12 MeV.

The data available for ^{48}Ti starts at 0.3 MeV, with the inelastic cross section edge at about 1.0 MeV (Fig. 2.9). By comparison, ^{46}Ti has a large radiative capture cross section for thermal neutrons (Fig. 2.10). In ^{46}Ti, a large number of radiative capture resonances are present between 1 keV and about 200 keV, which alter significantly the energy distribution of the neutrons incident on the TiB_2 absorber. The inelastic scattering edge in ^{46}Ti occurs at 0.9 MeV.

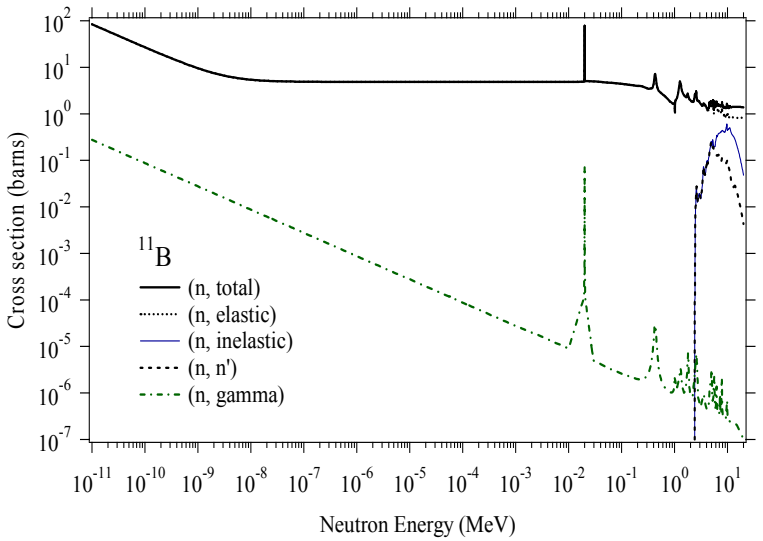

Figure 2.8. Neutron interaction cross sections of ^{11}B.

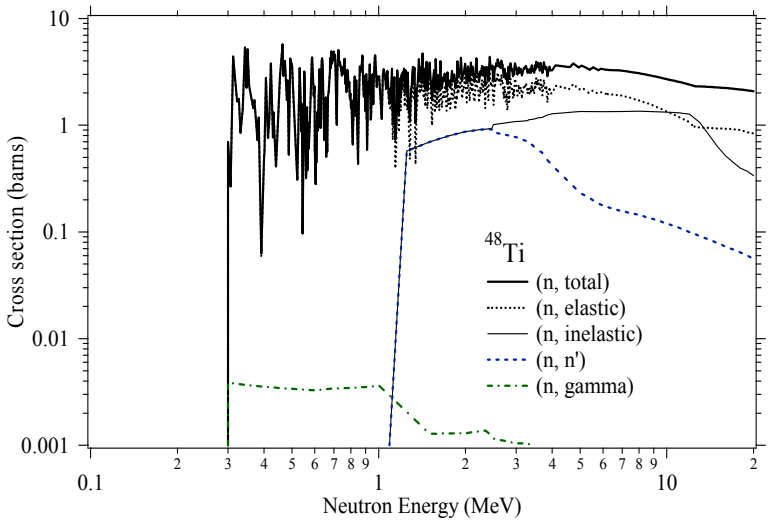

Figure 2.9 . Neutron interaction cross sections of ^{48}Ti.

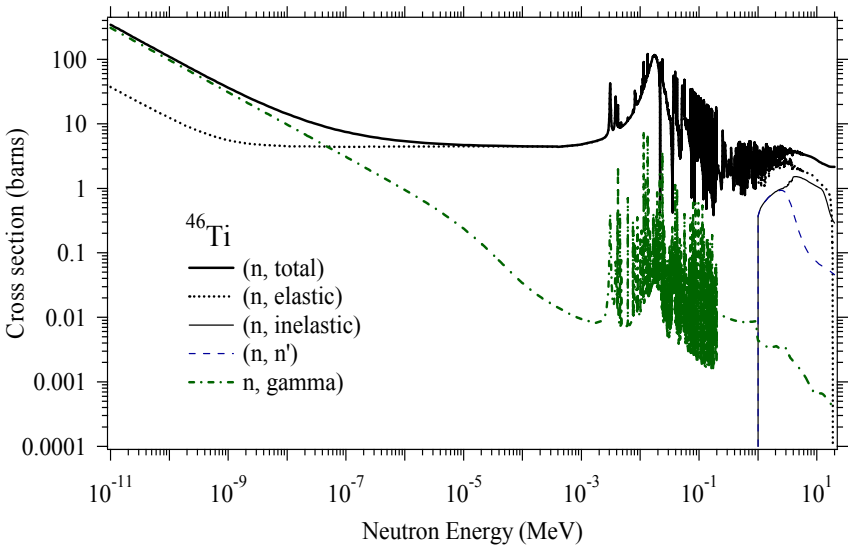

Figure 2.10. Neutron interaction cross sections of ^{46}Ti.

A type of reaction which was not discussed is the secondary neutron emission by (α, n) reaction [Rei 91]. The α-particle emitted in an (n, α) reaction can produce secondary neutrons when interacting with the ^{6}Li, ^{7}Li and the ^{19}F nuclei in LiF or with ^{10}B or ^{11}B in TiB_2. Because both the α-particle and the target nucleus are positively charged, this reaction takes place if the α-particle has enough energy to overcome the Coulomb barrier of the target nucleus and to exceed the threshold energy of the reaction [How 81]. This condition is not met for the nuclei in LiF. In this case, the (α, n) reaction has negative Q-value on the order of about -2 MeV and a threshold energy of minimum 2.36 MeV. Thus, the α-particle emitted with E_α = 2.05 MeV from the ^{6}Li(n, α)^{3}H reaction cannot produce secondary neutrons in (α, n) reactions.

For ^{10}B and ^{11}B, the (α, n) reaction has Q > 0, with zero threshold energy for the α-particle. However, the (α, n) reaction cross section with either ^{10}B or ^{11}B is on the order of 0.01 barns for the 1.47 MeV α-particle resulted from ^{10}B(n, α)^{7}Li reaction, which in the end produces a negligible contribution to the total number of neutrons.

2.2 Intrinsic absorption and interaction probabilities

The intrinsic absorption probability ε_{int} of a narrow parallel neutron beam with energy E entering a neutron absorber slab with thickness Δx is calculated with the following formula [Lam 66]:

$$\varepsilon_{int} = 1 - \Phi/\Phi_0 = 1 - \exp(-N\sigma\Delta x) < 1 \qquad (2.7)$$

where Φ_0 is the initial incoming flux of the parallel beam of neutrons and Φ is the flux of the outcoming parallel beam in the geometry in Fig. 2.11-A. $N = \rho N_A/M$ is the number density of the target atoms calculated from the density ρ and the molar mass M, with N_A the Avogadro number. In a more realistic geometry (Fig. 2.11-B) that applies to (2.7), the incoming neutron flux is not a parallel beam due to scatterings in the materials surrounding the absorber. A more accurate calculation of ε_{int} which takes into account a non-directional neutron flux (Fig. 2.11-B) is made with Monte Carlo methods and it is presented in Section 2.4.

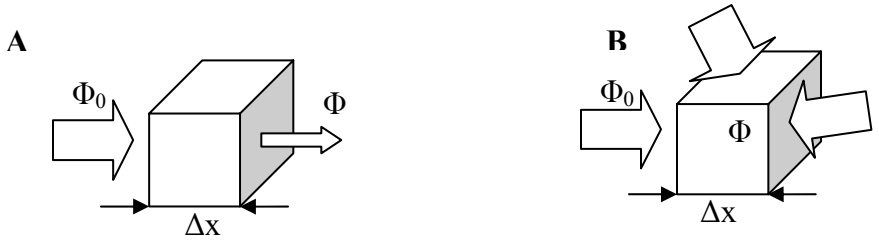

Figure 2.11. Geometry for absorption probability calculation. A - ideal beam geometry with directional neutron flux for analytical calculation. B – real geometry with non-directional neutron flux for Monte Carlo numerical simulation

As N and Δx are independent of energy, the absorption probability depends on the cross section $\sigma = \sigma(E)$ and in the first order predicts the energy response. As an example, the absorption probability ε_{int} of the (n, α) reaction is calculated with (2.7) in the geometry in

Fig 2.11-A with $\Delta x = 1$ cm for LiF and TiB_2 absorbers with natural isotopic composition (Fig. 2.12).

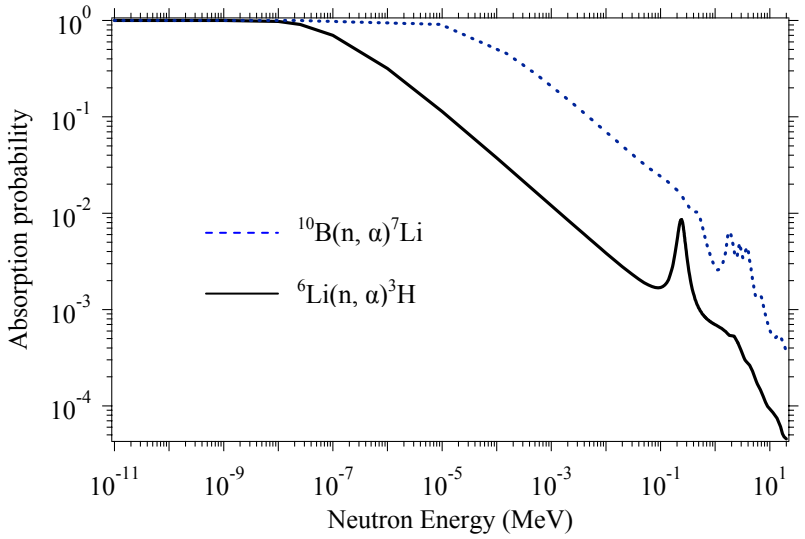

Figure 2.12. Neutron absorption probability in 1 cm thick LiF and TiB_2 absorbers with natural isotopic composition.

The resonant absorption structures above 100 keV noticed in the (n, α) reaction cross section (Fig. 2.2-A and Fig. 2.2-B) are present in the theoretical response in Fig. 2.12. Cold and thermal neutrons are 100% absorbed in 1 cm LiF and TiB_2. In the fast-neutron range, the absorption probability follows the structure in the cross section. At 240 keV, at the resonance in the $^{6}Li(n, \alpha)^{3}H$ reactions cross section, the efficiency is $\varepsilon_{int} = 0.85\%$ in LiF with natural isotopic composition. ε_{int} drops to below 0.1% at neutron energies > 400 keV. The (n, α) reaction in TiB_2 is a factor of 5 to 10 more efficient for fast neutrons than in LiF. The intrinsic detection efficiency ε_{int} can be increased by changing the isotopic composition of the absorber. For example, LiF crystals can be grown enriched in the ^{6}Li isotope from 7.6% natural composition to about 93% (a factor of 12 enrichment). Instead of natural composition TiB_2, one can use a pure boron metallic absorber that is enriched

to about 95% in ^{10}B [Bel 05], [Lan 05]. The effect of isotopic enrichment on ε_{int} calculated with equation (2.7) is presented in Fig. 2.13 for a LiF absorber.

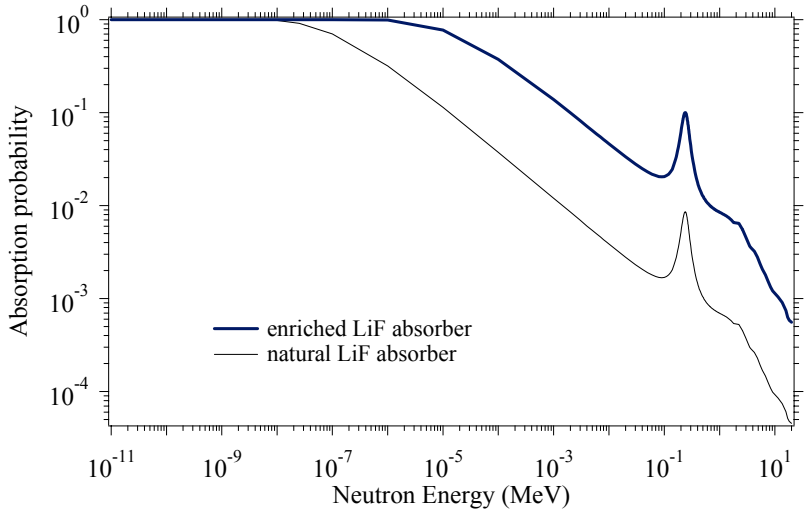

Figure 2.13. Comparison of absorption probability in natural LiF and 93% ^{6}Li-enriched ^{6}LiF absorbers. The absorber thickness is $\Delta x = 1$ cm.

As shown in Fig. 2.13, the isotopic enrichment has the effect of extending the 100% (n, α) reaction probability range to the epithermal neutron region. In the fast neutron region, ε_{int} increases by one order of magnitude with isotopic enrichment. For example, at the 240 keV peak, the efficiency is ε_{int} = 10% instead of 0.85% for natural isotopic composition.

It is important to quantify the gamma-ray absorption in LiF in order to see its contribution to the total energy deposited in the absorber. The intrinsic absorption probability for gamma-rays is calculated as:

$$\varepsilon_{int,\ gamma} = 1 - e^{-(\mu/\rho)\rho\Delta x} \tag{2.8}$$

where (μ/ρ) in cm^2/g is the mass energy absorption coefficient [XCO 06]. As an example, the photon absorption probability in LiF is presented in Fig. 2.14. It can be seen from Fig. 2.14 that gamma-ray photons up to 20 keV are completely photoabsorbed in 1 cm-thick

LiF. Photons with energies above 50 keV are predominantly scattered and thus they deposit less energy than their initial value. The 109 keV photon emitted by the first excited level in ^{19}F is absorbed with an efficiency of about 1%, comparable to the absorption of a neutron in the same energy range. By comparison, the 197 keV photon emitted from the second excited level in ^{19}F is absorbed with only 0.1 % efficiency. Gamma-rays emitted from the first excited states in ^{6}Li (1.5 MeV) and ^{7}Li (0.477 MeV) have photoabsorption probabilities below 0.1% and they do not contribute significantly to energy deposition in LiF.

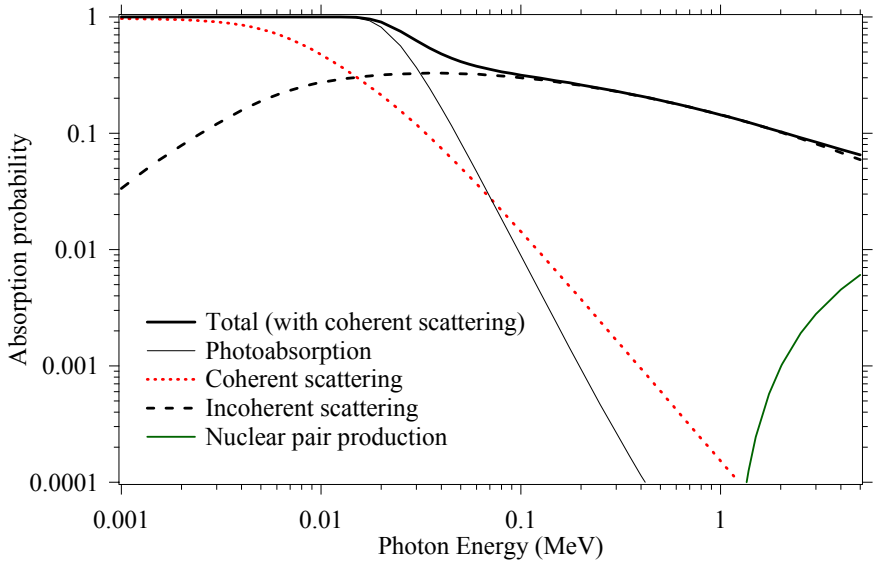

Figure 2.14. Photon interaction probability in 1 cm-thick LiF

Even in the event of full energy deposition, the energy deposited by a single independent gamma-ray photon produced by excited ^{19}F is about two orders of magnitude smaller than the Q-value of the (n, α) reaction with ^{6}Li. In an inelastic interaction, the kinetic energy of the neutron E_n is fully deposited in the absorber only if the scattered neutron is captured and the photon deposits its energy in the absorber at the same time. The pair

production above the threshold at 1.022 MeV does not play a significant role in the gamma-ray absorption, as the electron and the positron either escape out of the absorber or produce 511 keV gammas by annihilation, which are self-absorbed with $\varepsilon_{int,\ gamma} < 0.01\%$.

2.3 Neutron mean-free-path and reaction products range

The total energy $E_{total} = E_n + Q$ resulting from the (n,α) reaction is distributed among the reaction products. In order to determine E_{total}, the reaction products must deposit their energy completely in the volume of the absorber. Thus, for a complete energy deposition, the range of the reaction products should be shorter than the physical size of the absorber. The (n,α) reactions occur in the volume of the absorber at locations that depend on the energy of the neutron. The mean-free-path <mfp> of the neutron in the absorber is calculated as $<mfp> = (N\sigma)^{-1}$, and is independent of the thickness of the absorber [Kno 99], [Dud 76]. Figure 2.15 shows the mean-free-path of the (n,α) reaction as a function of energy in TiB_2 and LiF. At low neutron energy, where the absorption probability is higher, <mfp> ranges from micrometers to millimeters. This implies that, if the absorber has linear dimensions larger than <mfp>, thermal neutrons will interact in the absorber with a higher probability in an outer layer, which we call the Slow Neutron Skin Effect (SNSE). For fast neutrons, <mfp> is on the order of centimeters and tens of centimeters, which ensures uniform illumination of the volume of the absorber and uniform spatial distribution of the (n,α) reactions within the absorber. Thus, the fast-neutron part of the spectrum is not affected by the SNSE.

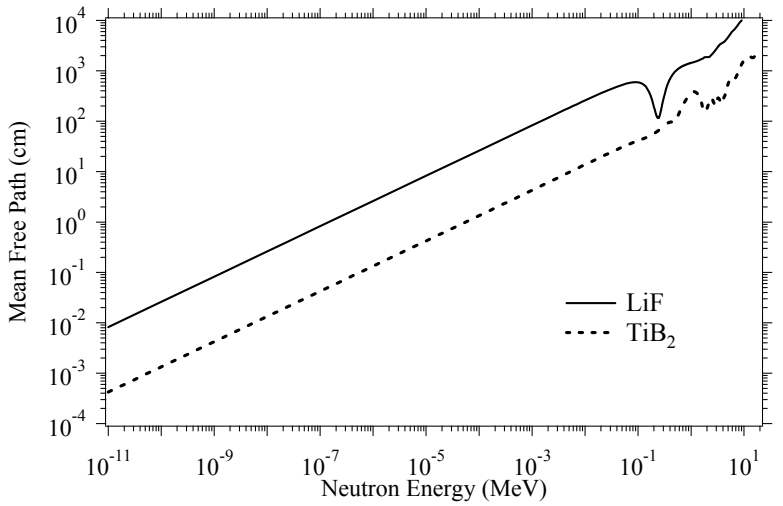

Figure 2.15. Neutron (n,α) mean-free-path <mfp> in natural isotopic composition LiF and TiB_2.

The biggest impact of the SNSE is on the formation of the thermal peak. From equation (2.7), it results that 99% neutron absorption takes place in a layer with thickness $\Delta x_{99\%}$ = <mfp>ln(0.01) = 4.6<mfp>. Also it is interesting to see the effect of the isotopic enrichment on the <mfp>. As the number density N of (n,α)-reacting nuclei increases, the mean free path decreases, which is visualized in Fig 2.16 for LiF absorber.

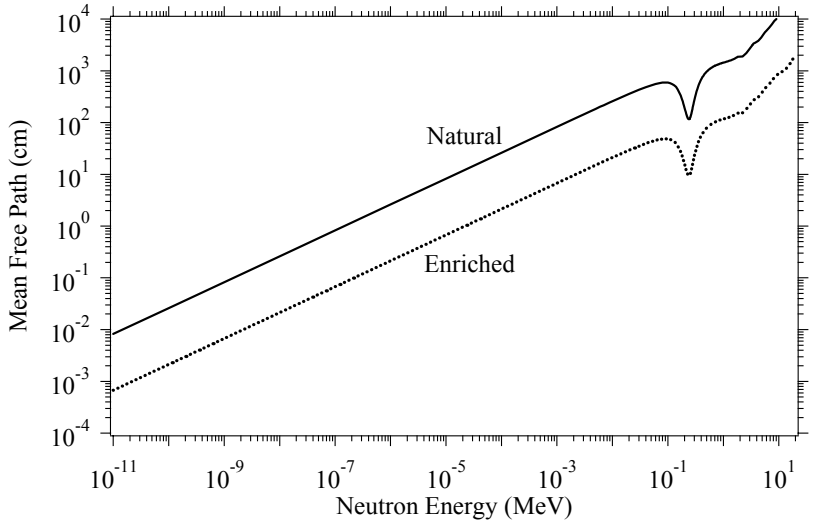

Figure 2.16. Neutron (n,α) mean-free-path comparison for natural LiF and 93% ^{6}Li-enriched ^{6}LiF absorbers.

A factor of 12 in ^{6}Li enrichment produces a factor of 12 reduction of the neutron mean free path, with the fast neutrons being unaffected by the enrichment, because their <mfp> still remains one order of magnitude larger than the size of the absorber, which ensures uniform (n,α) reactions within the absorber.

For enriched ^{6}LiF crystal with linear dimension of centimeters, cold and thermal neutrons with energies below ~10^{-7} MeV are absorbed in a layer of up to 200 μm at the surface of the absorber. Thus, the more the neutron flux is thermalized, the smaller its mean-free-path is. This translates into a larger spread of the thermal neutron absorption peak due to energy loss at the surface. Thus, the enrichment has the effect of extending the energy range over which the SNSE takes place. In practice, the thermal peak can be reduced with special experimental care in order to reduce the amount of moderating low-Z materials from around the cryostat. However, thermal and cold neutrons can still be produced when they interact with the low temperature stages in the measurement system.

Typically, the stopping range of an energetic α-particle or a heavy ion with MeV kinetic energies is in the range of 1-100 μm in a material with density of the order of 2 - 4 g/cm^3, depending on the particle energy [Kno 99], [Zie 77]. This ensures that the reaction products stop in the volume of the absorber and the total energy E_n + Q available from the (n,α) reaction is completely deposited in the absorber. When the neutron energy is low (e.g. thermal neutrons or below), the reaction products are emitted in opposite directions. According to the conservation laws for momentum and energy for the X(n, α)Y reaction, each reaction product carries a kinetic energy $E_\alpha = m_Y Q/(m_\alpha+m_y)$ and $E_Y = m_\alpha Q/(m_\alpha+m_y)$ respectively, where m_α and m_Y stand for the masses of the α-particle and Y nucleus. Table 2.3 presents a summary of the reaction product parameters when

the (n,α) reaction takes place with thermal neutrons. The average ion ranges are obtained from the TRansport of Ions in Matter (TRIM) software, developed by Ziegler et al. [Zie 77].

Table 2.3. Ion ranges in TiB_2 and LiF absorbers calculated with TRIM

Reaction	Absorber compound	Reaction product (ion)	Ion Energy E_0 (MeV)	Average Ion Range R_{ion} (μm)
$^{10}B(n, \alpha)^{7}Li$	TiB_2	^{7}Li	0.84	3.8
$^{10}B(n, \alpha)^{7}Li$	TiB_2	^{4}He	1.47	1.9
$^{6}Li(n, \alpha)^{3}H$	LiF	^{3}H	2.73	33.8
$^{6}Li(n, \alpha)^{3}H$	LiF	^{4}He	2.05	6.1

Because of the larger ion range of the reaction products in LiF, the SNSE is more intense in LiF than in TiB_2 and also stronger in enriched ^{6}LiF than in natural LiF. By comparing the data in Table 2.3 with Fig. 2.15 and Fig. 2.16, it can be concluded that the SNSE is produced in TiB_2 when the neutron energy is below 10^{-11} MeV (in the cold and ultra-cold region), whereas in enriched LiF the SNSE is produced even with thermal neutrons. If the 99% absorption layer has the thickness smaller than the range of the ion, then the ion deposits only partial energy in the absorber. Figure 2.17 shows snapshots from TRIM simulations for the ^{3}H and ^{4}He ions resulted from the $^{6}Li(n, \alpha)^{3}H$ reaction with thermal neutrons, assuming that the ions are produced as a narrow beam in the positive direction of the y-axis with the origin at the surface of the LiF absorber.

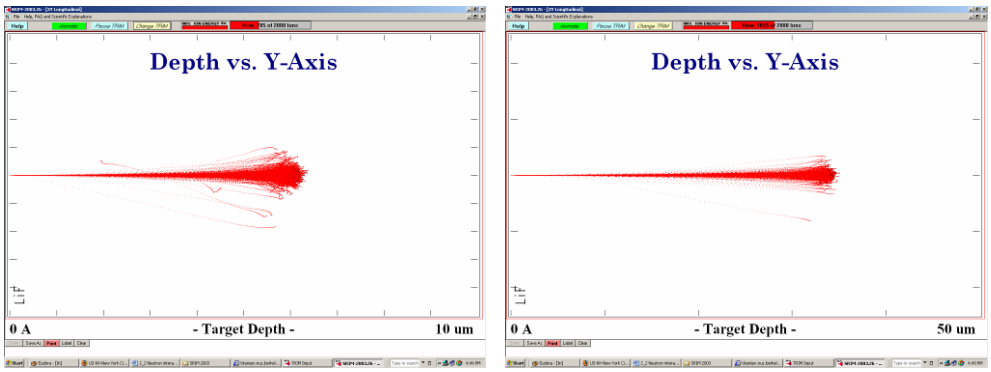

Figure 2.17. TRIM simulation of the range of the ions resulting from the $^{6}Li(n, \alpha)^{3}H$ reaction in LiF.

A schematic description of the SNSE is shown in Fig. 2.18. When the ion range is comparable with the depth of the neutron absorption from the surface (given by 4.6<mfp>), then it is possible for the ion to end its trajectory outside of the absorber (case b in Fig. 2.18) or to completely escape from the absorber with no energy deposition.

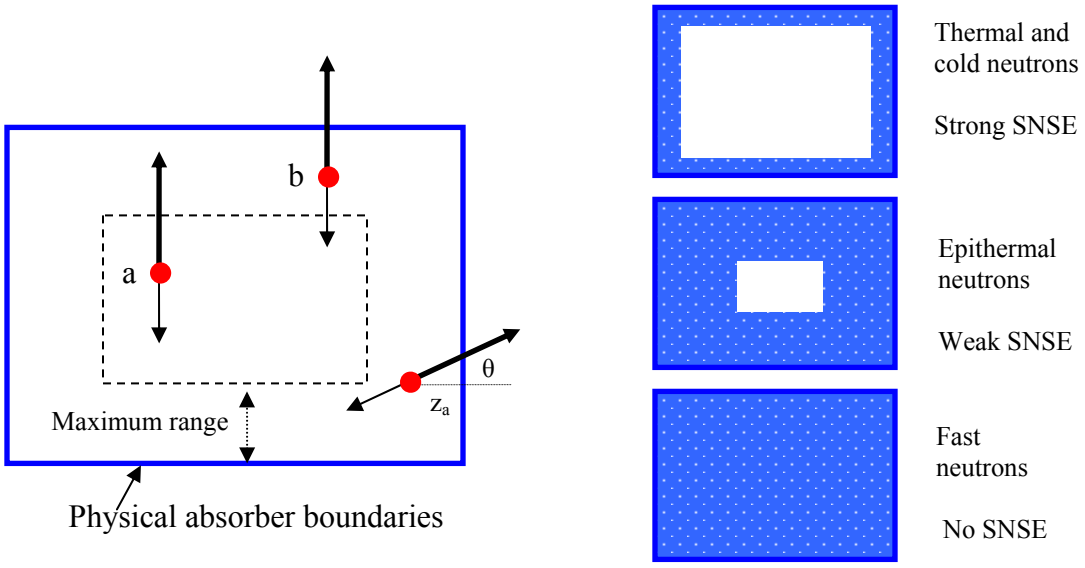

Figure 2.18. Schematic representation of the Slow Neutron Skin Effect (SNSE). Arrows represent the range of the reaction products. a – complete energy deposition (from fast neutrons that can access central regions in the absorber), b – partial energy deposition (from thermal or cold neutrons). The regions accessible inside the absorber at different neutron energies are presented to the right (shaded).

For fast neutrons that produce uniform irradiation in the volume of the absorber, the maximum fraction of the volume f_{max} from which the reaction products can partially escape is directly proportional to the ion range R_{ion}. This is shown by considering a cubic absorber with side length L and volume $V = L^3$. The volume V_{ion} from which ions having the range R_{ion} can escape is $6L^2R_{ion}$, which results in a fraction $f_{max} = 6R_{ion}/L$. In a cubic LiF absorber with 1 cm^3 volume and with R_{ion} = 33.8 μm, the fraction is $f_{max} \sim 2\%$ whereas in 1 cm^3 TiB_2 absorber with R_{ion} = 3.8 μm, the fraction is $f_{max} \sim 0.2\%$.

A semi-quantitative calculation of the energy lost at the surface is presented in the following example for an enriched LiF absorber: consider an absorption <mfp> on the order of 30 – 40 μm, comparable to the range of the 2.73 MeV ^{3}H ion obtained from TRIM. This <mfp> corresponds to a neutron energy of about 2 meV (Fig. 2.16). With the ion range data in Table 2.3 and the energy loss mechanism described in Fig. 2.18, the energy loss at the surface has been numerically simulated as a function of neutron energy in a range from 10^{-11} MeV to 10^{-9} MeV.

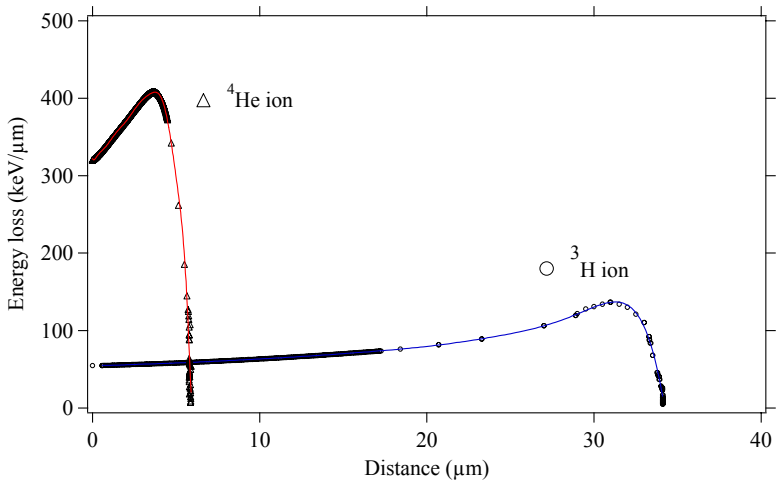

Figure 2.19. Energy loss curves of ^{3}H and ^{4}He ions from $^{6}Li(n, \alpha)^{3}H$ reaction in LiF.

In the algorithm, the thermal and epithermal absorption cross section (Fig. 2.2-A) is fit with a function given by $\sigma(E) = 1.4 + 0.205E^{-1/2}$ barns, with the energy in MeV. The <mfp> is calculated from <mfp> = $(N\sigma(E))^{-1}$ and the 99% absorption depth z_a is calculated using the 4.6<mfp> formula. One ion (^{3}H or ^{4}He) with its initial energy E_0 and known range R_{ion} from Table 2.3 is selected and it is projected towards the surface at a random angle θ with respect to the normal to the surface while the other ion resulting from the reaction is projected in the opposite direction. The distance to the surface is $d_a = z_a/\cos\theta$ (Fig. 2.18). If $d_a \geq R_{ion}$, then the ion energy is completely absorbed in the LiF

crystal. The total deposited energy is obtained by summing E_0 and the energy of the pair ion projected inside the crystal (^{4}He or ^{3}H). If $d_a < R_{ion}$, then the ion partially deposits energy in the crystal and its exit energy $E(d_a)$ is calculated from the fit of the energy loss curves for ^{3}H and ^{4}He in LiF, obtained from TRIM (Fig. 2.19). The solid curves in Fig. 2.19 are obtained by fitting the TRIM data with a 9th degree polynomial. The integrated area under each curve has a value equal to the total energy of the ion from Table 2.3.

The results of the numerical simulation are shown in Fig. 2.20. In each case, the lower energy region of the thermal peak (half-peak) is reconstructed. About 35% of the total neutrons with E = 10^{-11} MeV contribute to the tail, compared to only about 21% for neutrons with E = 10^{-10} MeV. When E = 10^{-9} MeV (= 1 meV), about 73% of the total number of events end up depositing energy at Q = 4.782 MeV with no low-energy tail right below this energy; the remaining 27% of the events deposit energy below ~ 4.2 MeV. However, we should not forget that the shape of the half-peak depends not only on the energy loss at the surface in absorption events, but also on the energy deposition resulting from elastic and inelastic scattering events. The neutron scattering followed by absorption in will be presented in Section 2.4.

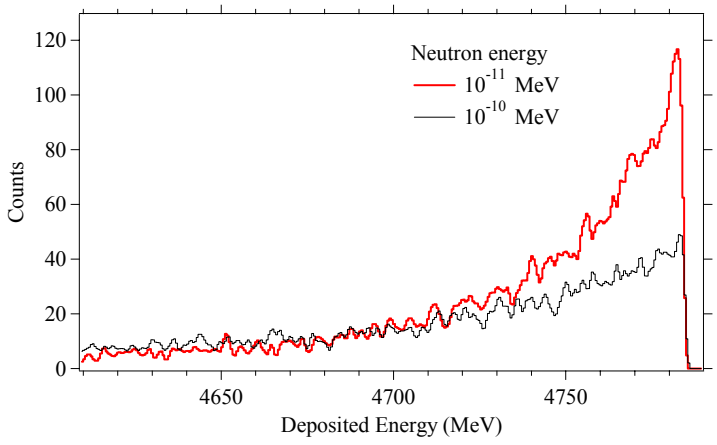

Figure 2.20. Numerical simulation of the low energy part of the thermal peak in 92% ^{6}Li-enriched ^{6}LiF absorber (energy loss half-peak).

A better quantification of the energy spread is made starting from the total number of events located in the Half Width Half Maximum (HWHM) and the Half Width Tenth Maximum (HWTM) of energy deposition half-peaks, where HWHM = FWHM/2. For each energy interval (bin) ΔE of the neutron flux, we define the fractions $f_{HWHM} < 1$ and $f_{HWTM} < 1$ as:

$$f_{HWHM} = \frac{\sum_{HWHM} N(E)}{N} \qquad \text{and} \qquad f_{HWTM} = \frac{\sum_{HWTM} N(E)}{N} \tag{2.9}$$

Where N(E) are the number of events in the HWHM and HWTM respectively, and N is the total number of detected events over the whole energy range. The fraction of events $f_i(E)$ in the HWHM coming from each ΔE depends on the fraction $f_N(E)$ of the initial neutron events in ΔE:

$$f_i(E) = f_{HWHM} f_N(E) \tag{2.10}$$

While f_{HWHM} and f_{HWTM} can be determined with equation (2.9) using the data in Fig. 2.20 (also see Table 2.4), $f_N(E)$ is obtained from Monte Carlo simulations of the neutron transport with MCNP in the actual measurement geometry.

Table 2.4. Event fraction in HWHM and HWTM of the half-peaks

Energy bin (MeV)	**HWHM (keV)**	**HWTM (keV)**	f_{HWHM}	f_{HWTM}
$10^{-11} – 10^{-10}$	19.2 ± 0.9	142 ± 12	0.100 ± 0.016	0.162 ± 0.020
$10^{-10} – 10^{-9}$	49.4 ± 2.6	177 ± 18	0.062 ± 0.010	0.143 ± 0.018

The overall values of the HWHM and the HWTM are calculated as a weighted average of each individual value:

$$\text{HWHM} = \frac{\sum_i (\text{HWHM})_i f_i(E)}{\sum_i f_i(E)} \quad \text{and} \quad \text{HWTM} = \frac{\sum_i (\text{HWTM})_i f_i(E)}{\sum_i f_i(E)} \tag{2.11}$$

This semi-quantitative estimate predicts the formation of the lower energy half of the thermal peak. However, this approach based solely on the neutron absorption mean free path does not completely describe all the energy loss mechanisms from the LiF absorber. For example, additional energy loss due to LiF scintillation reported in [Bir 64], [Dzo 04], [Mar 93] is not included in this model.

2.4 Theoretical response and MCNP neutron transport simulations of the neutron absorbers

The total microscopic cross section for any type of reaction for an A_nB_m compound is given by [Lam 66]:

$$\sigma = n\sigma_A + m\sigma_B \tag{2.12}$$

A modified form of equation (2.7) can be applied to calculate the intrinsic interaction probability for a directional (collimated) neutron beam with uniform energy distribution as shown in Fig. 2.11.

In a simplistic model, the (n, α) neutron reaction contributes to the reduction of the neutron flux, while the elastic scattering has the effect of bringing a fraction of the non-absorbed neutrons back in the sample volume. The interaction probability is calculated for a two-step process: neutron scattering with ^{19}F followed by (n, α) reaction with ^{6}Li. Using equation (2.7), ε_{int} can be expressed as:

$$\varepsilon_{int} = \exp\left(-N\sigma_{scattering}\Delta x\right) \times \left\{1 - \exp\left(-N\sigma_{(n,\alpha)}\Delta x\right)\right\} \tag{2.13}$$

When using $\sigma_{scattering} = \sigma_{(n,n')} + \sigma_{(n,\gamma)}$ for ^{19}F, at 27 keV (first radiative capture resonance), the probability of the two-step process is of 0.98 × 0.031 = 0.03 (Fig. 2.21). For the peak at 0.270 MeV in the inelastic cross section of ^{19}F, ε_{int} = 0.41 × 0.13 = 0.05. As a result, both these resonances have no effect on the detector response, which is dominated by the (n,α) reaction. A much stronger effect is obtained when the elastic scattering cross section of ^{19}F is taken into account, in which case $\sigma_{scattering} = \sigma_{elastic}$. At 27 keV, the interaction probability is of 0.01 × 0.031 = 0.00031, a reduction of two orders of magnitude. The overall theoretical response is given by the (n,α) absorption reaction modulated by the elastic scattering cross section that produce dips at the location of the resonance. The (n,α) reaction with ^{6}Li produces neutron absorption that is most relevant in the thermal and epithermal tail (below 50 keV) and in the 240 keV absorption peak.

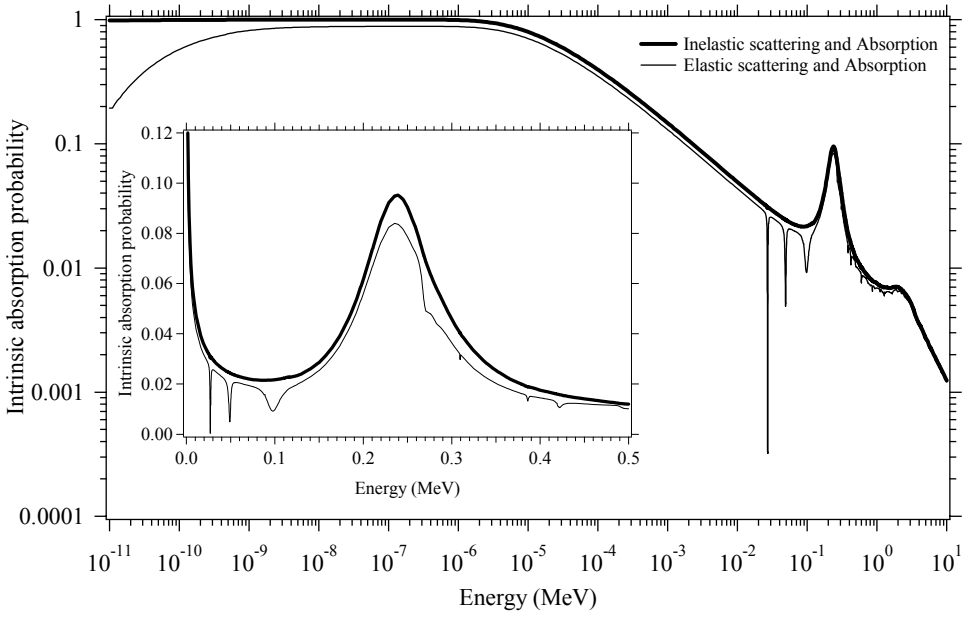

Figure 2.21. Theoretical intrinsic response of a 1 cm-thick ^{6}LiF absorber. The inset shows the region below 0.5 MeV on a linear scale.

In order to obtain the response of the LiF absorber in terms of deposited energy due to the (n, α) reaction, the energy distribution in Fig. 2.21 must be shifted up in energy with an

amount equal to the Q-value. However, using equation (2.7) to calculate the response of the neutron absorber assumes collimated beam geometry such as in Fig. 2.11-A, in which the neutrons are moving on straight trajectories inside the absorber and their flux is reduced according to an exponential function. In fact, the neutrons interact with the absorber in complex random processes and an analytical calculation that follows their transport is simply impossible. The MCNP-Polimi version [Poz 03] has been used for simulating the energy deposited by neutrons, recoil nuclei and photons at each interaction event. The theoretical result presented in Fig. 2.21 is improved by the numerical simulation which can take into account more complex series of events such as elastic or inelastic scattering followed by (n, α) reaction .

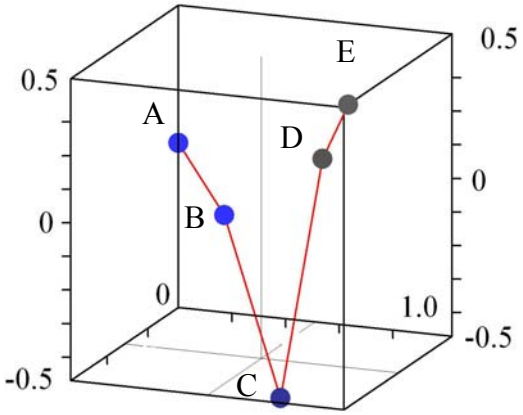

Figure 2.22. MCNP simulation of a neutron interaction history in 1 cm^3 LiF showing a succession of four scattering events followed by (n, α) absorption. The coordinates show the distance in cm.

For example, the spatial location of the events in a single neutron history is simulated with MCNP-Polimi (Fig. 2.22). In chronological order, the events are from A to E: inelastic neutron scattering with ^{19}F, elastic neutron scattering with ^{7}Li, with ^{19}F, inelastic

neutron scattering with ^{19}F, and (n,α) reaction with ^{6}Li. For this history, the total energy effectively deposited in the absorber is of 5.012 MeV.

In terms of energy response, the three-dimensional response matrix R(E) of the neutron absorber is given in the following coordinates: E_n = incident energy distribution, $E_{deposited}$ = deposited energy distribution, N(E) = number of events. Experimentally, only a two-dimensional projection of R(E) is accessible in the ($E_{deposited}$, N(E)) coordinates, which represents the measured spectrum M(E) obtained as the sum per energy bin of all the neutron interactions mentioned before. The original incident spectrum S(E) is inferred from the response matrix R(E), as follows:

$$S = R^{-1} \times M \tag{2.13}$$

The MCNP-Polimi simulations have been performed for 1 cm^3 cubic enriched LiF and natural TiB_2 absorbers in free space in order to obtain the intrinsic response to ^{252}Cf with Watt energy distribution described by:

$$f(E) = Ce^{-E/1.095}\sinh\sqrt{2.926E} \tag{2.14}$$

The simulation assumes that neutrons are generated as a monodirectional beam with uniform spatial distribution on one surface of the cube. Figure 2.23 presents the 3-D response matrix obtained for the enriched LiF absorber, in which each point represents the number of events in 5 keV × 5 keV energy bins from zero to 8 MeV on each energy axis. The total number of events in this simulation is of 65,000, out of which 54,600, i.e. 84% deposit energy below the Q-value of the $^{6}Li(n, \alpha)^{3}H$ reaction at 4.782 MeV. The response matrix presents structure which is better visualized in projections on (E_n, $E_{deposited}$) and ($E_{deposited}$, N(E)) planes.

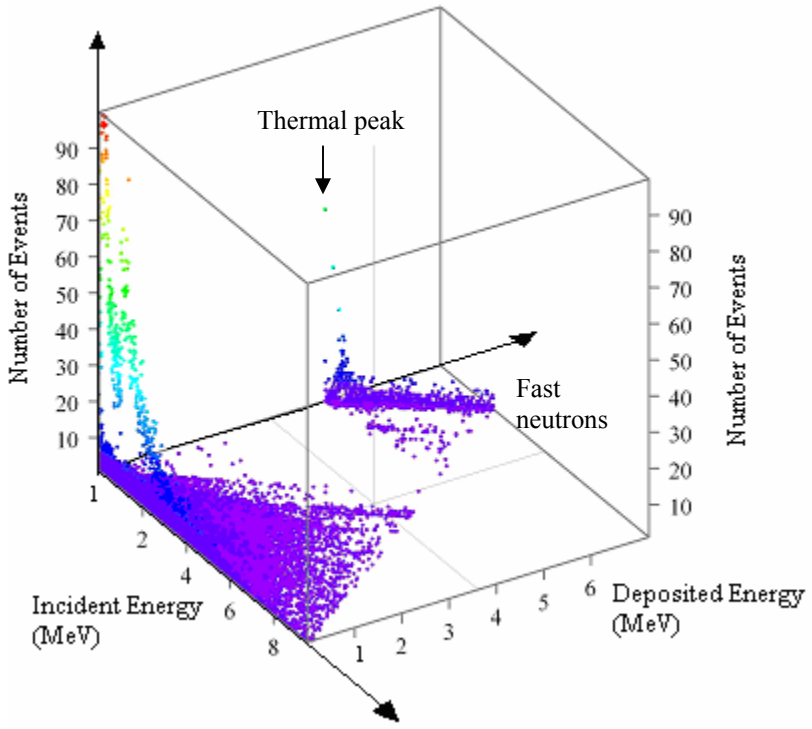

Figure 2.23. MCNP-Polimi 3-D intrinsic response matrix of the ^{6}LiF absorber.

The projection of the response matrix in the (E_n, $E_{deposited}$) plane is shown in Fig. 2.24 for LiF. In this plot, each point corresponds to the sum of energies deposited at each interaction in a single neutron history. In Fig. 2.24, the straight lines with slope = 1 are from reactions in which $E_{deposited} = E_n + Q$. One example is the straight line starting at Q = 4.78 MeV deposited energy which corresponds to direct (n, α) reaction. The thermal peak is located at incident neutron energy $E_n \sim 0$. The two parallel lines that appear right below the Q-value corresponds to the two-step reaction in which neutrons have initially lost their energy in inelastic interactions with the first or the second excited level in ^{19}F at 109 keV and 197 keV respectively, and have subsequently interacted in (n, α) reaction with ^{6}Li. Much weaker lines corresponding to the two-step interaction with the third and fourth energy levels in ^{19}F are visible starting at about 1.4 MeV incident energy. Three

endothermal reactions with slope = 1 are visible: $^{6}Li(n, p)^{6}H$ ($E_{threshold}$ = 3.18 MeV), $^{19}F(n, n+\alpha)^{15}N$ ($E_{threshold}$ = 4.22 MeV), and $^{19}F(n, p)^{19}O$ ($E_{threshold}$ = 4.25 MeV).

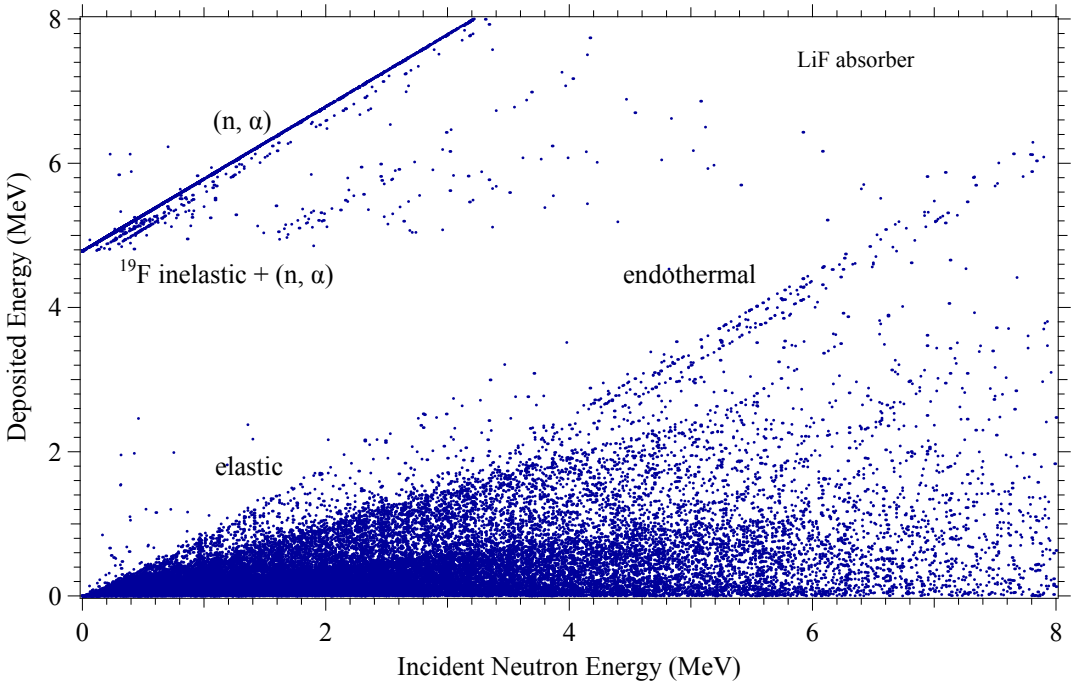

Figure 2.24. MCNP simulation of energy response matrix for LiF.

Events corresponding to elastic (potential) scattering with ^{6}Li, ^{7}Li, and ^{19}F have a maximum slope = $4A/(A+1)^2 < 1$ and they are grouped at deposited energies below 2 MeV. The highest slope corresponds to elastic (potential) scattering with ^{6}Li, while the lowest slope is due to potential scattering with ^{19}F. The MCNP simulation for LiF suggests that interference in the energy deposition above the Q-value is due to incident neutrons with energies above 6.2 MeV originating in the endothermal reactions mentioned before.

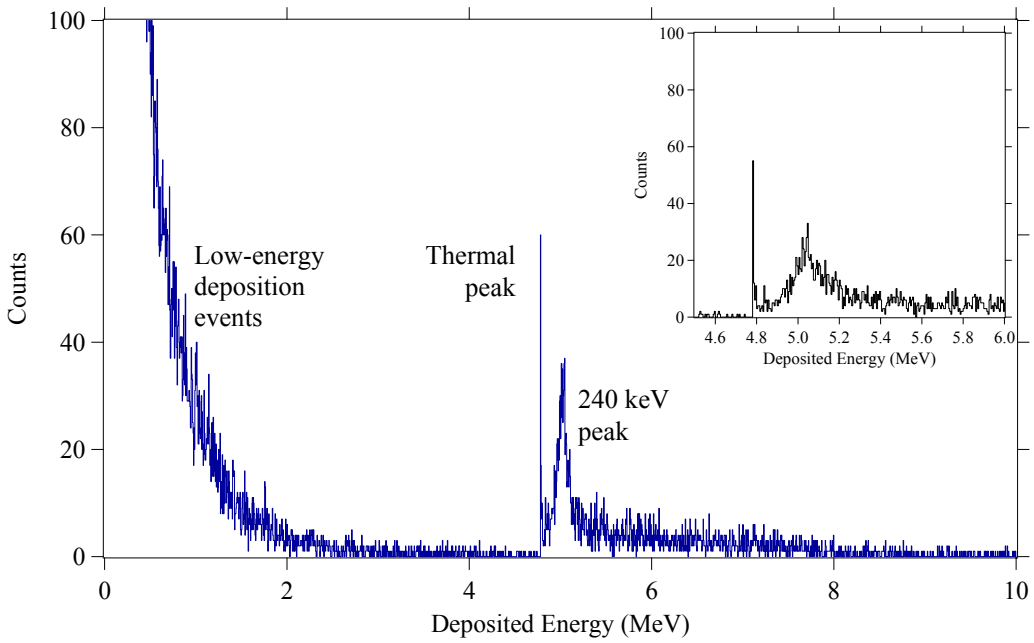

Figure 2.25. MCNP simulation of the expected response of ^{6}LiF to ^{252}Cf neutron source. The inset shows the response between 4.6 and 6 MeV deposited energy.

The projection in the ($E_{deposited}$, N(E)) plane of the response matrix is histogrammed in energy bins 5 keV wide and it shows the expected neutron spectrum from energy deposition in LiF (Fig. 2.25). The spectrum is smoothed with a Gaussian filter with 10 keV FWHM to simulate the instrumental energy resolution. The low-energy elastic scattering events are located below 4.78 MeV, which offers good discrimination for high-energy neutron events which deposit energy above the Q-value. The events between 0 and 4.78 MeV are expected to represent about 84% of the total number, which dominate the reaction rate in LiFIn this simulation, the thermal peak extends to about 52 keV above the Q-value and it has a FWHM of about 26 keV. The resonance peak at 240 keV in the spectrum originates in the (n,α) reaction and it represents the increased absorption in this region.

From the simulation, the intrinsic absorption efficiency for events above the Q-value in the 1 cm^3 ^6LiF absorber is estimated at 2.6% while the analytical calculation estimates about 1.5%. For the TiB_2 absorber with natural isotopic composition (Fig. 2.26), the MCNP simulation renders a more complex picture: the two (n, α) absorption lines originating at Q_1 = 2.31 MeV and Q_2 = 2.78 MeV contribute to the formation of two thermal peaks.

The intense line that originates at $E_{threshold}$ = 1.61 MeV is due to the $^{46}Ti(n, p)^{46}Sc$ endothermal reaction. Right below it, there is the $^{47}Ti(n, \alpha)^{44}Ca$ reaction, which presents a lower reaction rate due to reduced cross section. An other endothermal reaction has $E_{threshold}$ = 4.82 MeV and it is due to the $^{10}B(n, ^2H)^9Be$ reaction. At low incident neutron energies, there are three more endothermal reactions: $^{48}Ti(n, \alpha)^{48}Ca$ with $E_{threshold}$ = 0.08 MeV, $^{10}B(n, p)^{10}Be$ with $E_{threshold}$ = 0.226 MeV and $^{10}B(n, 2\alpha)^3H$ with $E_{threshold}$ = 0.322 MeV. Energy deposition events from elastic (potential) scattering with B and Ti isotopes with a maximum slope = $4A/(A+1)^2 < 1$ and they are grouped at deposited energies below about 1 MeV. Interferences in the thermal peak occur mainly for events resulted from $^{46}Ti(n, p)^{46}Sc$ reaction with neutrons with $E_n > 2$ MeV.

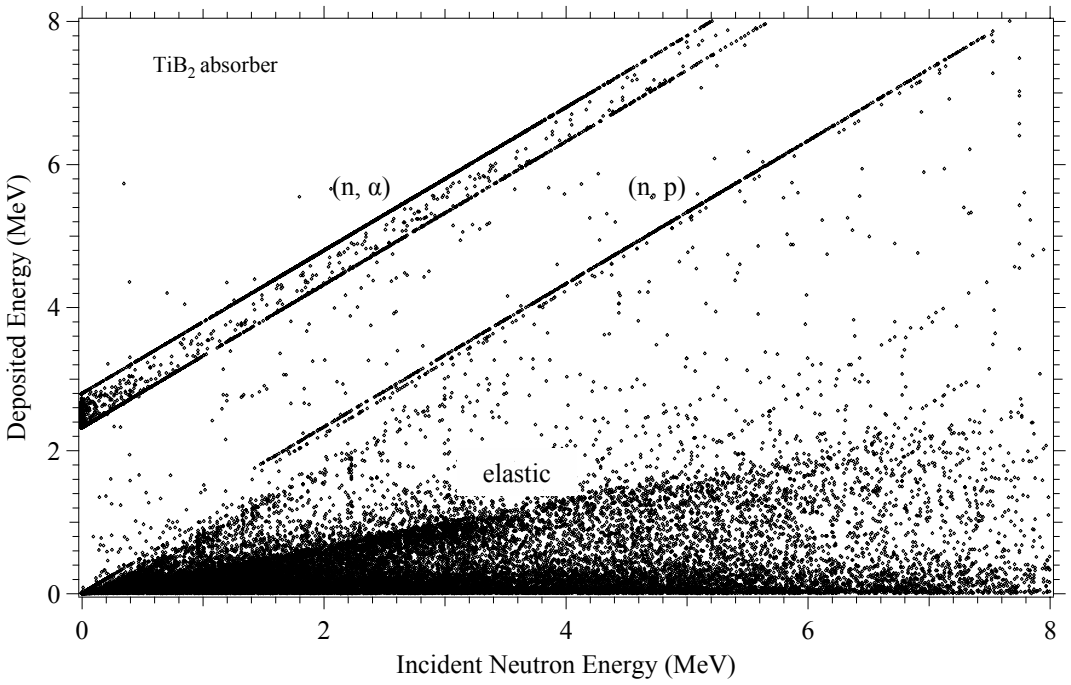

Figure 2.26. MCNP simulation of energy response matrix for TiB_2.

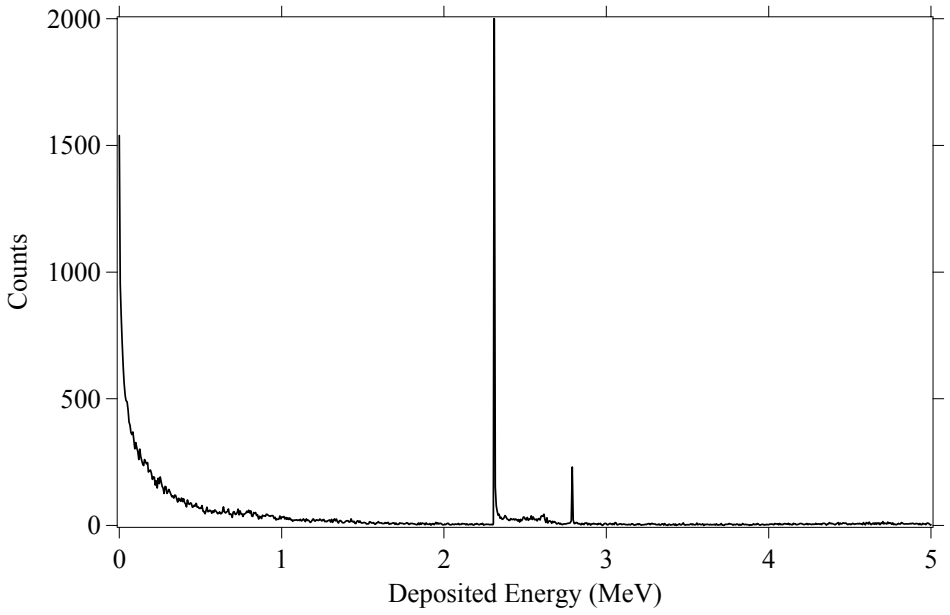

Figure 2.27. MCNP simulation of the expected response of TiB_2 to ^{252}Cf neutron source.

The expected energy deposition response of TiB_2 to neutrons is presented in Fig. 2.27. The long tail corresponding to low-energy events extends to about 1 MeV. The two peaks corresponding to the two decay channels in $^{10}B(n, \alpha)^7Li$ reaction are located at 2.31 MeV and 2.78 MeV respectively and they appear in the ratio of 96/4. Energy discrimination is also possible in the TiB_2 absorber, because the two energy deposition peaks are located at about 1 MeV above the low-energy events tail (Fig. 2.27). The MCNP spectrum is smoothed with a Gaussian filter with 10 keV FWHM to simulate the instrumental energy resolution. The intrinsic absorption efficiency resulted from simulation is of about 6% for events above 2.31 MeV.

From the MCNP-Polimi simulation one can also extract information about the location neutron of the interaction in the absorber, based on the position of the interaction as depicted in Fig. 2.28. This is most interesting for LiF absorbers, as it has been shown previously that the energy loss at the surface contributes to the widening of the thermal peak below the Q-value. When selecting energy deposition events in the range from 4.70 MeV to 4.85 MeV, and histogram their number as function of interaction location in bins 100 μm wide, a fraction of about 26% of the events occur in a layer no thicker than 500 μm (Fig. 2.28).

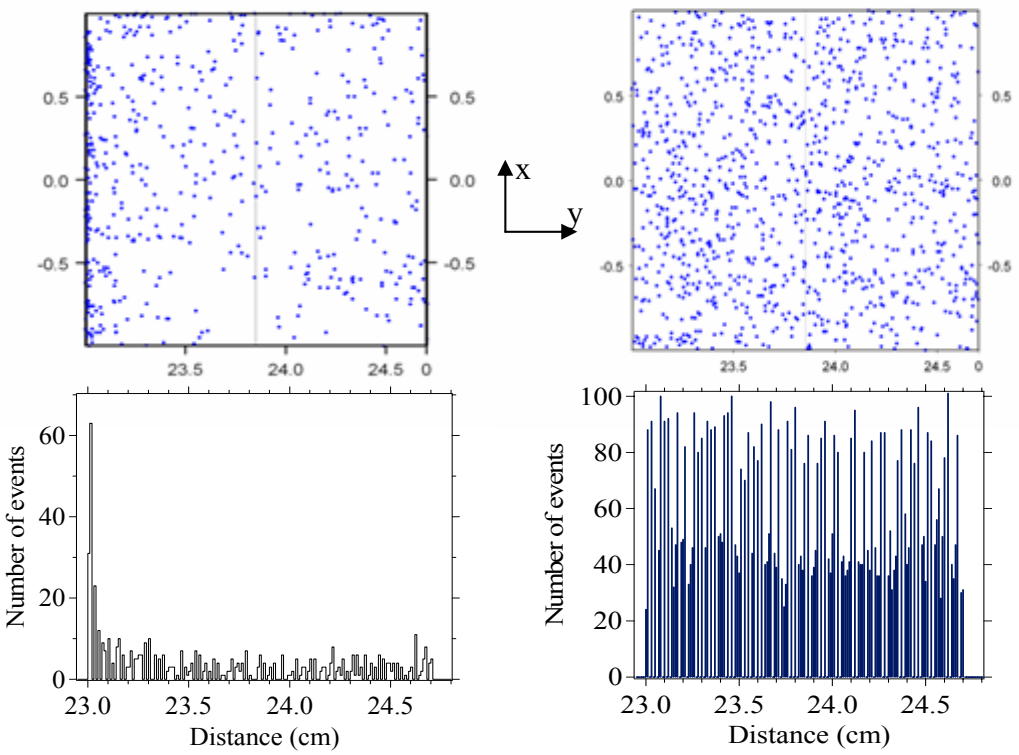

Figure 2.28. Neutron interaction position for energies around the Q-value of the (n, α) reaction in LiF. The neutron source is located at the left of the absorber.

Interaction events from thermal neutrons that deposit energy around the Q-value are grouped towards the input surface of the LiF absorber, while events due to high energy neutrons depositing energy above 4.9 MeV are spread uniformly throughout the absorber (Fig. 2.28 – right).

Chapter 3. Neutron Calorimeter Theory

This chapter describes the analytical model of high resolution fast-neutron spectrometers based on single-neutron calorimetry, i.e. on the measurement of the temperature rise produced by the absorption of a fast neutron.

The advantage of calorimetry for high energy resolution spectroscopy is due to the small excitation energies $\varepsilon = k_B T$ of the phonons that serve as signal carriers in a thermal signal. When the neutron's kinetic energy E_n is completely deposited in an absorber with heat capacity C_{abs}, an average number of high-frequency non-thermal phonons are initially excited in the absorber [Bro 85], [Kit 99]. The high-frequency phonons down-convert in energy in a complicated relaxation cascade until their average temperature is close to the operating temperature T. The initial neutron energy E_n is determined from the measurement of the small increase in the temperature of the absorber $\Delta T = (Q+E_n)/C_{abs.}$ As a consequence, the lower the operating temperature T, the larger the number of phonons that are produced. Assuming a deposited energy $Q + E_n = 4.782$ MeV, after undergoing a few reflections inside the crystal, a large fraction of the high energy phonons convert down in energy (thermalize) to the equilibrium temperature in the crystal lattice at T = 0.1 K resulting in $\varepsilon \approx 8$ μeV, and $N_{phonon} = (Q + E_n)/\varepsilon = C_{abs}T/k_BT \sim 4\times10^{11}$ phonons. If the same energy $Q + E_n = 4.782$ MeV were deposited in a semiconductor such as germanium (with an electron-hole pair excitation energy of 3 eV), it would have created only $\sim1\times10^{6}$ electron-ion pairs. Whereas the electrical charges are collected as an electrical current, the phonons propagate in the material as a heat wave and their effect on the temperature variation is sensed as a continuous function. However,

because we do not measure phonons individually but rather heat pulses, the attention is focused in measuring small fluctuations in the temperature above the thermal level due to particle interaction. Considering that the Poisson statistics still apply, the energy fluctuation δE is given by the energy per phonon $\varepsilon = k_B T$ multiplied with the fluctuation in the number of phonons $\delta N_{phonon} = (N_{phonon})^{1/2} = (C_{abs} T/k_B T)^{1/2}$. In this approximation it results that $\delta E \approx (k_B T^2 C_{abs})^{1/2}$. The complete theoretical expression found in literature for the FWHM energy resolution is given by [Mos 84]:

$$\Delta E_{FWHM} = 2.355\sqrt{4k_B T^2 C_{abs}} \tag{3.1}$$

3.1 Neutron Detection Principle

The operating principle of a calorimeter is illustrated in Fig. 3.1. The calorimeter consists of a radiation absorber with heat capacity C_{abs} that is strongly coupled to a thermometer and initially held at a temperature T_0. A neutron with energy E_n deposits a total energy $E_0 = E_n + Q$ in an exothermic absorption reaction with energy release Q the absorber. This increases the temperature of the absorber by $\Delta T \approx E_0/C_{abs}$, which is subsequently measured by a sensitive thermometer. In the design discussed here, the thermometer consists of a superconducting film held at the transition between its superconducting and normal state (Fig. 3.2), commonly known as a transition edge sensor (TES). The energy deposited in the absorber is eventually transferred to the cold bath through a thermal conductance G, and the system returns to the equilibrium temperature T_0, ready to detect a new particle.

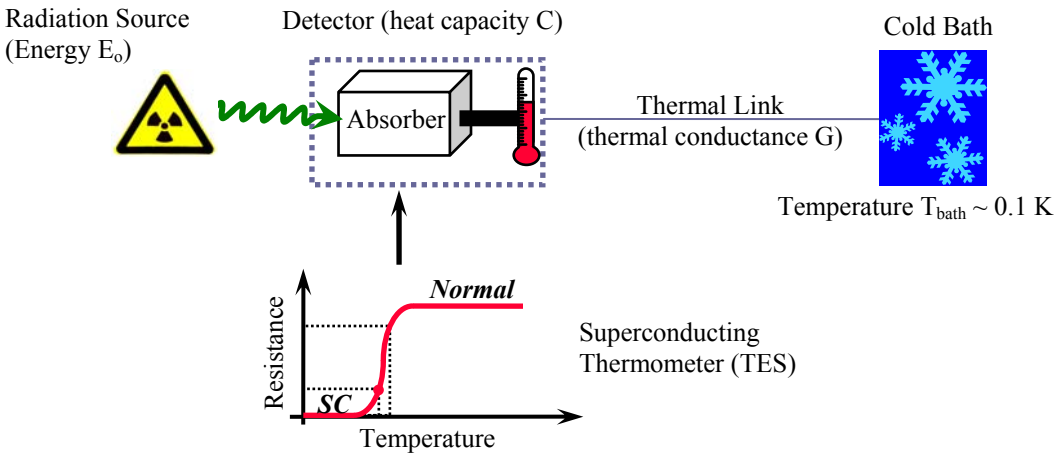

Figure 3.1. General principle of calorimetric radiation detection.

The temperature signal is schematicaly shown in Fig. 3.2. The amplitude of the pulse is $\Delta T \approx E_0/C_{abs}$ and the decay time $\tau = C_{abs}/G$ depends on the absorber heat capacity and on thermal conductance G. Larger absorbers therefore result in higher detection efficiency, smaller signals and larger decay times. This detection principle can be applied to any kind of particle (neutron, electron, ion or α-particle) or electromagnetic radiation (x-ray, γ-ray) that deposits energy in an absorber. In each case, the absorber has to be tailored for the type of particle or radiation intended for detection in order to ensure high absorption efficiency. For example, Sn is a good absorber for detecting gamma-rays [Cun 02] while ^{6}Li and ^{10}B-based absorbers are more efficient for neutrons [Kno 99], [Bel 05]. In order to detect radiation in a certain energy range, the heat capacity C_{abs} must be adjusted so that the temperature increase ΔT does not drive the sensor (TES) out of the range of the resistive transition. As an example, an energy deposition of 4.782 MeV from the ^{6}Li(n, α)^{3}H reaction sensed with a sensor (TES) having ΔT = 1 mK requires a heat capacity of roughly 0.7 nJ/K. Since the absorber heat capacity also sets the limiting energy resolution

of the detector, its size is usually chosen as big as possible for highest efficiency, while still offering enough energy resolution to separate the spectral features of interest.

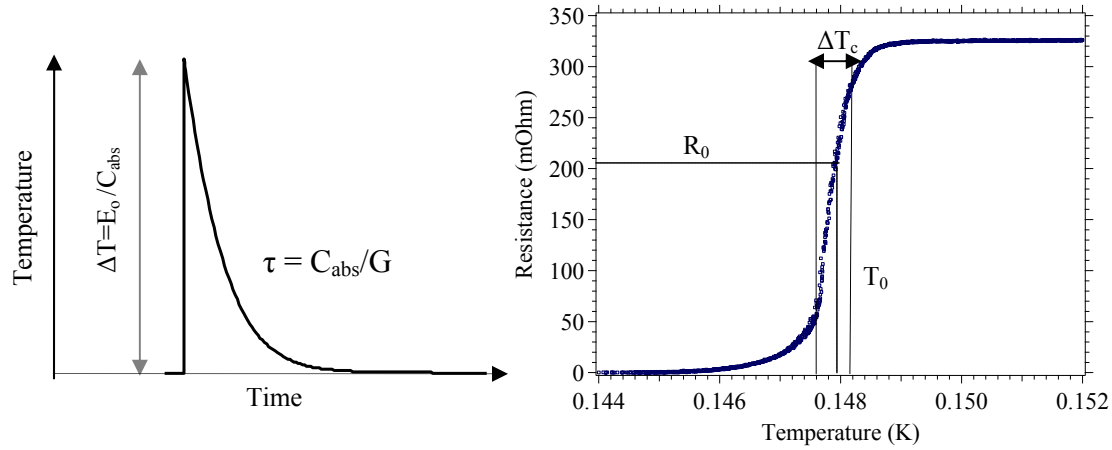

Figure 3.2. Schematic thermal pulse from a calorimeter (left). Experimental superconducting transition with ΔT_c = 0.9 mK and T_c = 148 mK (right).

3.2 Single thermal mass calorimeter model

The transition region of the TES thermometer (Fig. 3.2) is characterized by a sensitivity $\alpha = d(\log R)/d(\log T)$. To first order, $\partial R/\partial T$ is constant at the bias point (T_0, R_0) in the transition. Typical values of α are between 50 and 1000 with the normal resistance R_n ~ 10 - 500 mΩ, depending on the material choices and the deposition process [Ali 05], [Cho 01]. The TES thermometer can therefore be characterized as a thermistor with an electrical resistance R, operated at a voltage bias V and at a current I. When included in an electronic circuit, the TES measures the variation in the resistance with temperature upon the detection of an energetic event.

The calorimeter is modeled here by considering two basic cases:

i. The simple calorimeter, in which the absorber and the thermometer form a single thermal mass with heat capacity C_{abs} (Fig. 3.3).

ii. The composite calorimeter, in with the absorber and the thermometer are treated as two separate thermal masses with a finite thermal conductance between them.

For a simple calorimeter, the thermometer also functions as the radiation absorber, with heat capacity C_{abs}, both coupled to a cold bath at the temperature T_{bath} through a thermal conductance G (Fig. 3.3). In this simple model, the excess phonons produced by photon or particle absorption are assumed to thermalize instantaneously. This means that the phonon energies are reduced to k_BT by anharmonic decay through phonon-electron and phonon-lattice scattering on time scales much faster than the signal rise time [Bro 85], [Lin 00], [Pro 95]. Because of fast ballistic phonon propagation inside the high-quality absorber crystal, one can also neglect any position dependence in the absorber, i.e. the energy measured with the TES is assumed to not depend on the location of the neutron interaction in the volume of the crystal.

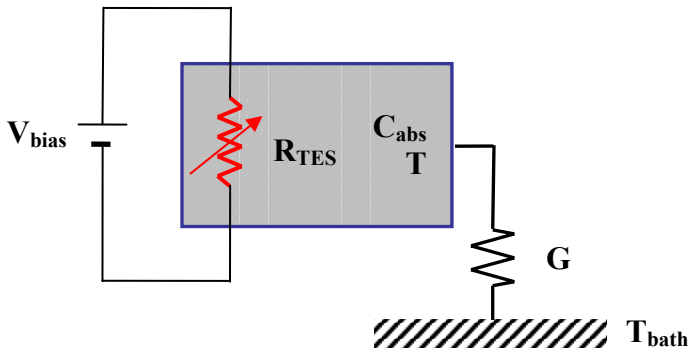

Figure 3.3. Schematic of the coupled electrical and thermal circuits for a single thermal mass calorimeter.

The cooling power of the absorber is $P_{cooling} = G\Delta T$. The rate of change in the temperature of the calorimeter is given by $C(d\Delta T/dt) = - G\Delta T$, with the initial condition $\Delta T(0) = \Delta T_0 \approx E_0/C_{abs}$. The differential equation can be solved by $\Delta T = \Delta T_0 \exp(-t/\tau_0)$.

This equation describes the observed signal waveform in the case that the absorber and the sensor are identical or if the TES has a much smaller heat capacity C_{TES} than the absorber and if the thermal coupling between the absorber and the TES is very strong so that phonons can flow unimpeded between them.

3.2.1 Time domain analysis

The TES is operated stably in the superconducting – normal transition region at the critical temperature $T_c \approx T_0$ by maintaining a cold bath temperature $T_{bath} < T_c$ and heating the TES into the transition to a constant bias point (T_0, R_0). Typically, the TES is DC-biased at voltage V_0 = constant, so that the Joule power $P_{Joule} = V_0^2/R_0$ dissipated in the resistance R_0 is balanced in equilibrium by the cooling power $P_{cooling} = G(T_0 - T_{bath})$, which extracts the heat from the TES sensor. The evolution of temperature T of the absorber described by the power flow in the system according to:

$$C\frac{dT}{dt} = P_{Joule} - P_{cooling} \tag{3.2}$$

When the TES sensor cools, the resistance drops and P_{Joule} increases while $P_{cooling}$ drops. When $P_{cooling} = P_{Joule}$, a stable thermal equilibrium state is reached. The TES is self-biased in the transition at $T_0 = T_{bath} + P_{Joule}/G$ due to the feedback between cooling and Joule heating, an effect known as electro-thermal feedback (ETF) [And 42], [Irw 95], [Irw 96]. Neutron absorption raises the temperature of the calorimeter by an amount $\Delta T_0 \approx E_0/C$. As T increases, R increases and the current I = V/R through the TES drops. This reduces the Joule power dissipated in the TES, to first order by:

$$\Delta P_{Joule} = \frac{\partial P_{Joule}}{\partial T}\Delta T = -\frac{V_0^2}{R^2(T)}\frac{\partial R}{\partial T}\Delta T = -\frac{\alpha P_{Joule}}{T_0}\Delta T \tag{3.3}$$

Similarly, the cooling power becomes $\Delta P_{cooling} = G\Delta T$ results and since the zero order equilibrium terms cancel out, equation (3.2) results in:

$$C\frac{d\Delta T}{dt} = -\left(\frac{\alpha P_{Joule}}{T_0} + G\right)\Delta T \tag{3.4}$$

This differential equation can be solved analytically to describe a transitory temperature signal:

$$\Delta T(t) = \Delta T_0 \exp\left(-t / \tau_{eff}\right) \tag{3.5}$$

$$\tau_{eff} = \frac{C/G}{1+\frac{\alpha P_{Joule}}{GT_0}} \equiv \frac{\tau_0}{1+\frac{G_{ETF}}{G}} < \tau_0 \tag{3.6}$$

Here τ_{eff} is the effective decay time in the presence of ETF. ETF reduces the decay time of the signal below $\tau_0 = C/G$, since the reduction of Joule heating from the bias is faster than the heat flow through the weak link G. This is reflected in equation (3.6), by the term $G_{ETF} = \alpha P_{Joule}/T_0$ which is equivalent to a thermal conductance due to electro-thermal feedback in parallel with G from the weak thermal link, with an effective open-loop gain G_{ETF}/G.

The resulting current upon neutron absorption which provides the signal to be measured, is obtained from the sensitivity of the TES:

$$\Delta I(t) = \frac{\partial I}{\partial T}\Delta T(t) = -\alpha I_0 \frac{\Delta T}{T_0} = -\frac{\alpha I_0}{T_0}\frac{E_0}{C}\exp\left(-t/\tau_{eff}\right) \tag{3.7}$$

where $I_0 = V_0/R_0$. The positive temperature variation in the absorber is converted into negative current pulses due to the positive change of resistance $\partial R/\partial T > 0$ and the DC voltage bias. The resulting current signal $\Delta I(t)$ is proportional to the energy E_0 deposited by neutron absorption, and it is measured with the electrical circuit of the current-

sensitive preamplifiers. In the limit of the extreme electro-thermal feedback with $G_{ETF} >> G$ and thus $\tau_{eff} \approx C/G_{ETF}$, the total deposited energy can be obtained by integrating the signal according to

$$E_{measured} = \int V_0 I(t)dt = V_0 \frac{\alpha I_0}{T_0} \frac{E_0}{C} \tau_{eff} = E_0 \tag{3.8}$$

3.2.2 Frequency domain analysis

The noise characteristics of the calorimeter detector can be analyzed more conveniently in the frequency domain. The Fourier transform $I(\omega) = \int_0^\infty I(t)e^{-j\omega t}dt$, where $j^2 = -1$ with I(t) given by equation (3.7) results in a signal current in frequency space:

$$I_{signal}(\omega) = I_0 \alpha \frac{\Delta T_0}{T_0} \frac{\tau_{eff}}{\sqrt{1 + \omega^2 \tau_{eff}^2}} \tag{3.9}$$

The noise in the system consists of the Johnson current noise $i_{Johnson} = v_n/R_0$ due to the random motion of the electrical charges in the TES with voltage noise density $v_n^2 = 4k_B T R_0$ and an electrical resistance R_0, and the phonon noise due to the random motion of phonons across the thermal conductance G, given by:

$$i_{phonon}(\omega) = -\frac{\alpha I_0}{T_0} T(\omega) \tag{3.10}$$

Here, T(ω) is obtained from the Fourier transform of equation (3.4) which results in:

$$T(\omega) = \frac{p_n(\omega)}{(G_{ETF} + G) + j\omega C} = \frac{p_n(\omega)}{S(\omega)} \tag{3.11}$$

where $p^2_n(\omega) = 4k_B T^2 G$ is the density of the phonon noise and

$$S(\omega) = (G_{ETF} + G) + j\omega C \tag{3.12}$$

is the phonon noise responsivity of the calorimeter.

The two current noise terms add in quadrature and produce a total noise current:

$$i_{total}^2(\omega) = \frac{v_n^2(\omega)}{R_0^2} + \left[\frac{\alpha I_0}{(G + G_{ETF})T_0}\right]^2 \frac{p_n^2(\omega)}{1 + (\omega\tau_{eff})^2} \tag{3.13}$$

The phonon noise has a roll-off at $1/\tau_{eff}$, while Johnson noise is constant. The noise equivalent power (NEP) injected in the TES can be written in terms of i_{total} and the responsivity S as:

$$NEP(\omega) = T(\omega)S(\omega) = \left(\frac{T_0}{\alpha I_0}\right) i_{total} S(\omega) \tag{3.14}$$

For an optimally filtered signal, the limiting energy resolution can be calculated by integrating the noise equivalent power (NEP) from zero to infinite frequency [Mos 84], [Irw 95]:

$$\frac{1}{\Delta E_{FWHM}^2} = \frac{1}{(2.355)^2} \int_0^\infty \frac{4 d\omega}{NEP^2(\omega)} \tag{3.15}$$

From equations (3.12), (3.13) and (3.14), the noise equivalent power results in:

$$NEP^2(\omega) = NEP_0^2 \left\{ \frac{\alpha^2 P_{Joule}}{GT_0} + \left[1 + \left(\frac{G_{ETF}}{G}\right)^2\right] + (\omega\tau_0)^2 \right\} \tag{3.16}$$

where

$$NEP_0^2 = 4k_B T_0^2 G \frac{T_0 G}{\alpha^2 P_{Joule}} \tag{3.17}$$

The energy resolution equation (3.15) can be integrated as an (1/u)atan(x/u) function which results in:

$$\Delta E_{FWHM} = \xi\sqrt{k_B T^2 C} \tag{3.18}$$

where ξ is given by:

$$\xi = \left(\frac{4G}{\alpha^2 \left(G + G_{ETF} \right)} \right)^{1/2} \tag{3.19}$$

When $G_{ETF} >> G$ (extreme ETF regime) and $\alpha >> 1$, the energy resolution is reduced below the $(k_B T^2 C)^{1/2}$ value [Irw 95].

3.3 Composite calorimeter theory

To better simulate the response of a neutron detector in which the sensor chip is glued to the neutron absorber, the single thermal mass is separated into two sub-systems: an absorber with heat capacity C_{abs} at temperature T_{abs}, which is coupled to the TES with heat capacity C_{TES} through a finite thermal conductance G_{abs}. The voltage-biased TES at temperature T_{TES} is thermally connected to the cold bath through the thermal conductance G_{TES}. In the quiescent state, the absorber and the TES are at the same temperature $T_0 > T_{bath}$ due to Joule heating $P_{Joule} = V^2/R$ of the TES.

.

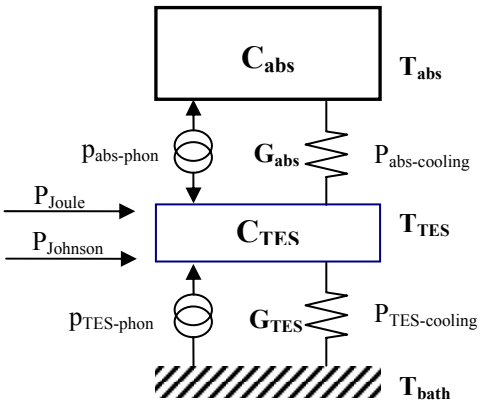

Figure 3.4. Composite calorimeter model with a finite thermal conductance G_{abs} between the absorber and the TES.

In this model, neutron interactions take place in the absorber only, and the excess phonons produced are assumed to instantaneously and uniformly thermalize throughout the volume of the absorber [Bue 94], [Lin 00]. The heat flows from the absorber to the TES through a finite thermal conductance G_{abs}, where it produces a measurable signal by heating the TES and then flows to the cold bath through G_{TES}. Here we focus on the pulse signal formation in the TES and on the energy resolution of the system.

3.4.1 Time-domain analysis

For the composite calorimeter, the power balance equations in the absorber and the TES are:

$$C_{abs}\frac{dT_{abs}}{dt} = -G_{abs}(T_{abs} - T_{TES}) \tag{3.20.a}$$

$$C_{TES}\frac{dT_{TES}}{dt} = -(G_{ETF} + G_{TES})(T_{TES} - T_{bath}) + G_{abs}(T_{abs} - T_{TES}) \tag{3.20.b}$$

The term $-G_{abs}(T_{abs} - T_{TES})$ represents cooling of the absorber to the TES, and the term $-(G_{ETF} + G_{TES})(T_{TES} - T_{bath})$ represents the cooling of the TES to the cold bath by electro-thermal feedback conductance $G_{ETF} = \alpha P_{Joule}/T_0$ and by G_{TES}.

Neutron absorption deposits an energy E_0 in the absorber, so the initial conditions at $t = 0$ are given by:

$$T_{TES}^0 = T_{bath} + P_{Joule}/(G_{ETF} + G_{TES}) \tag{3.21.a}$$

$$T_{abs}^0 = T_{bath} + P_{Joule}/(G_{ETF} + G_{TES}) + E_0/C_{abs} = T_{TES}^0 + E_0/C_{abs} \tag{3.21.b}$$

The system of coupled differential equations can be written in a matrix form as:

$$\frac{\partial}{\partial t}\begin{pmatrix} T_{abs} \\ T_{TES} \end{pmatrix} = \begin{pmatrix} -\frac{G_{abs}}{C_{abs}} & \frac{G_{abs}}{C_{abs}} \\ \frac{G_{abs}}{C_{TES}} & -\frac{G_{TES}+G_{ETF}+G_{abs}}{C_{TES}} \end{pmatrix}\begin{pmatrix} T_{abs} \\ T_{TES} \end{pmatrix} + \begin{pmatrix} 0 \\ (G_{TES}+G_{ETF})T_{bath} \end{pmatrix} \tag{3.22}$$

This matrix equation can be solved analytically for T_{TES} to describe the signal formation as measured by the TES. The general solution of equation (3.22) is a linear combination of the homogenous and the inhomogeneous solutions:

$$\begin{pmatrix} T_{abs} \\ T_{TES} \end{pmatrix} = \begin{pmatrix} T_{abs} \\ T_{TES} \end{pmatrix}_{homogenous} + \begin{pmatrix} c_1^{abs} \\ c_1^{TES} \end{pmatrix} e^{\lambda_1 t} + \begin{pmatrix} c_2^{abs} \\ c_2^{TES} \end{pmatrix} e^{\lambda_2 t} \tag{3.23}$$

The coefficients λ_1 and λ_2, which have units of 1/time, are the eigenvalues of the determinant of the matrix:

$$\begin{vmatrix} -\frac{G_{abs}}{C_{abs}} - \lambda & \frac{G_{abs}}{C_{abs}} \\ \frac{G_{abs}}{C_{TES}} & -\frac{G_{TES}+G_{ETF}+G_{abs}}{C_{TES}} - \lambda \end{vmatrix} = 0 \tag{3.24}$$

They have the values

$$\lambda_{1,2} = -\frac{A \pm \sqrt{A^2 - B}}{2C_{abs}C_{TES}} \tag{3.25}$$

with

$$A = C_{TES}G_{abs} + C_{abs}(G_{abs} + G_{TES} + G_{ETF})$$

$$B = 4C_{TES}C_{abs}(G_{TES} + G_{ETF})G_{abs} \tag{3.26}$$

The constants c_1 and c_2 in equation (3.23) are obtained from the initial conditions equation (3.21) and lead to the full analytical solution

$$T_{TES}(t) = T_{TES}^0 + \frac{E_0 G_{abs}}{\sqrt{A^2 - B}}\left(e^{-\frac{A-\sqrt{A^2-B}}{2C_{abs}C_{TES}}t} - e^{-\frac{A+\sqrt{A^2-B}}{2C_{abs}C_{TES}}t} \right) \tag{3.27}$$

The equation describes a signal waveform with a decay time τ_d and a finite rise time τ_r corresponding to the first and the second exponential. They have the values

$$\tau_{r,d} = 2C_{abs}C_{TES}/\left(A \pm \sqrt{A^2 - B}\right) \tag{3.28}$$

The plus sign corresponds to the rise time τ_r and the minus sign produces the decay time τ_d, such as $\tau_d > \tau_r$. The finite rise time τ_r is due to the finite thermal conductance G_{abs} and reflects the fact that the TES will respond to the temperature rise in the absorber upon neutron detection only after being heated through the finite G_{abs}. By comparison, the signal waveform of the simple models produces an infinitely fast rise time and a finite decay time.

In the experimental section, τ_r and τ_d are measured from the pulses while C_{abs} and C_{TES} are calculated at the operation temperature from the dimensions and the material parameters of the absorber and the TES. In order to speed up the pulse decay and increase the count rate of the detector, we examine the variation of the decay time with the G_{abs} and G_{TES} (Fig. 3.5). The simulations show that τ_d saturates when the thermal conductance ratio G_{abs}/G_{TES} is increased above a limit set by $\tau_d = C_{abs}/(G_{abs} + G_{TES})$, which serves as a bottleneck in the thermal relaxation back to equilibrium. Note that as the thermal conductances are increased to speed up the detector response, the initial assumptions of fast and homogenous energy thermalization will eventually no longer be valid. At lower values of G_{TES}, a stronger coupling between the absorber and TES is necessary to achieve decay time saturation. However, G_{TES} can not be increased indefinitely in order to reduce the pulse duration, as it also increases the phonon noise.

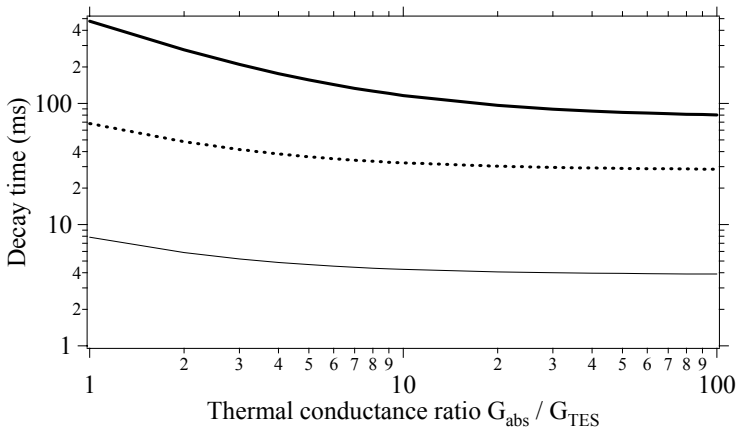

Figure 3.5. Decay time dependence on the thermal conductance ratio G_{abs}/G_{TES} with G_{TES} = 10 nW/K (——), 100 nW/K (- - -), 1000 nW/K (——).

Experimentally, equations (3.26) and (3.28) can be used to extract the thermal conductances G_{abs} and G_{TES} which result in:

$$G_{abs} = \eta \frac{C_{abs} C_{TES}}{\left(C_{abs} + C_{TES}\right)} \frac{\tau_r + \tau_d}{\tau_r \tau_d} \quad \text{and} \quad G_{TES} = \frac{1}{G_{abs}} \frac{C_{abs} C_{TES}}{\tau_r \tau_d} - G_{ETF} \tag{3.29}$$

$$\text{with } \eta = \left(1 - \frac{\tau_r \tau_d}{(\tau_r + \tau_d)^2} \frac{C_{abs} + C_{TES}}{C_{TES}}\right)^{1/2}.$$

In practice, neutron detectors are designed such as $C_{abs} >> C_{TES}$ and $G_{abs} >> G_{TES}$, and equation (3.27) simplifies to:

$$T_{TES}(t) = T^0_{TES} + \frac{E_{total}}{C_{abs}}\left(e^{-t/\tau'_d} - e^{-t/\tau'_r}\right) \tag{3.30}$$

$$\text{with } \tau'_d \approx C_{abs}/\left(G_{TES} + G_{ETF}\right) \text{ and } \tau'_r \approx C_{TES}/G_{abs} \tag{3.31}$$

In this limit, the decay time τ_d reduces to the expression in equation (3.6), and is set by the heat flow from the absorber to the cold bath. As before, while τ_d becomes shorter as G_{ETF} is increased. Similarly, the signal rise time τ_r is shorter than the decay time τ_d due to the strong thermal coupling G_{abs} between the absorber and the TES and the smaller heat capacity C_{TES} of the TES. This is illustrated in Fig. 3.6 for two pulses obtained with

equation (3.27) for typical values C_{TES} = 10 pJ/K, G_{TES} = 1 nW/K, and C_{abs}= 1 nJ/K at 140 mK. The TES has α = 60 and the quiescent bias power is P_{Joule} = 10 pW. The inset shows the same pulses on a logarithmic time scale, with a rise time a factor of 100 smaller than the decay time. The pulse shows that for large G_{abs} both rise and decay times are shortened and the pulse amplitude increases (Fig. 3.6). Because G_{ETF} is in parallel with G_{TES}, it dominates the time scale for pulse decay and determines ultimately the maximum count rate capabilities of the detector.

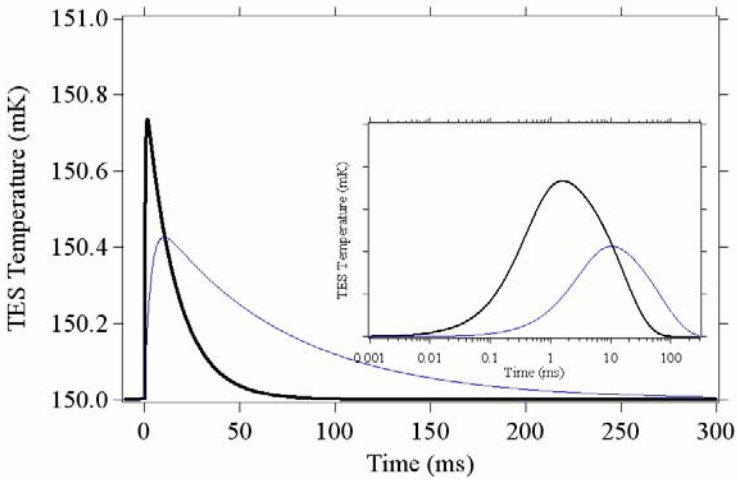

Figure 3.6. Simulated pulse waveforms for the response of a detector to thermal neutrons in a composite ^{6}LiF calorimeter with G_{abs} = 100 nW/K (——) and G_{abs} = 10 nW/K (——).

3.4.2 Frequency-domain analysis

We use the same approach to understand the noise in the composite calorimeter that we have used for the single-thermal mass model. Equations (3.20) are Fourier-transformed and yield:

$$j\omega C_{abs} T_{abs} = -G_{abs}\left(T_{abs} - T_{TES}\right) + p_{abs-phon} \tag{3.32}$$

$$j\omega C_{TES} T_{TES} = \frac{V_n^2}{R} - G_{TES}\left(T_{TES} - T_{bath}\right) + G_{abs}\left(T_{abs} - T_{TES}\right) + I_0 V_n + \mathbf{p}_{abs-phon} + p_{TES-phon}$$

There are now two phonon noise terms, which are introduced in order to take into account the random phonon transport across the two thermal conductances G_{abs} and G_{TES}, with $p^2_{abs\text{-}phon} = 4k_BT^2G_{abs}$ and $p^2_{TES\text{-}phon} = 4k_BT^2G_{TES}$. These two terms, become significant in the noise analysis of the calorimeter. These equations can be solved for $T_{TES}(\omega)$:

$$T_{TES}(\omega) = \frac{\mathbf{p}_{abs-phon} + (I_0V_n + G_{TES}T_{bath} + \mathbf{p}_{TES-phon} + \mathbf{p}_{abs-phon})\dfrac{G_{abs} + j\omega C_{abs}}{G_{abs}}}{(\dfrac{\alpha P_{Joule}}{T_0} + G_{TES} + G_{abs} + j\omega C_{TES})\dfrac{G_{abs} + j\omega C_{abs}}{G_{abs}} - G_{abs}} \tag{3.33}$$

In a more general form, equation (3.33) is written as:

$$T_{TES}(\omega) = \frac{NEP(\omega)}{S(\omega)} \tag{3.34}$$

where NEP(ω) is the noise equivalent power as before and S(ω) is the spectral responsivity of the detector:

$$S(\omega) = G_{TES}\left\{1 + \frac{G_{ETF}}{G_{TES}} + \omega^2\tau_{abs}\tau_{TES} + j\omega\left[\tau_{TES} + \tau_{abs}\left(1 + \frac{G_{ETF} + G_{abs}}{G_{TES}}\right)\right]\right\} \tag{3.35}$$

with $\tau_{TES} = C_{TES}/G_{TES}$ and $\tau_{abs} = C_{abs}/G_{abs}$. In the limits of the simple calorimeter model, when $C_{TES} \rightarrow 0$, $p_{abs\text{-}phon} = 0$ and $G_{abs} \rightarrow \infty$, we obtain $S(\omega) = (G_{ETF} + G_{TES}) + j\omega C_{abs}$, in agreement with equation (3.12).

From equations (3.10) and (3.33), the noise current terms can be regrouped in Johnson and phonon components which add in quadrature to the total noise current. The Johnson noise current is obtained by grouping the terms in V_n and the remaining terms in the equation represent the phonon noise current.

$$i_{Johnson}(\omega) = V_n\left[\frac{1}{R_0} - \frac{\alpha I_0^2}{T_0S(\omega)}\left(1 + j\omega\tau_{abs}\right)\right] \tag{3.36}$$

and

$$i_{phonon}(\omega) = -\frac{\alpha I_0}{T_0}\frac{p_{abs-phon} + \left(p_{TES-phon} + p_{abs-phon} + G_{TES}T_{bath}\right)\left(1 + j\omega\tau_{abs}\right)}{S(\omega)} \tag{3.37}$$

By rearranging equation (3.36), the Johnson noise current results in:

$$i_{Johnson}(\omega) = \frac{V_n}{R_0}\frac{\omega^2\tau_{abs}\tau_{TES} + \alpha P_{Joule}/G_{TES}T_0 - 1}{T_0 S(\omega)} +$$

$$+ j\omega\frac{V_n}{R_0}\frac{\left[\tau_{TES} + \tau_{abs}\left(1 + G_{abs}/G_{TES} - \alpha P_{Joule}/G_{TES}T_0\right)\right]}{T_0 S(\omega)} \tag{3.38}$$

For ω = 0, the minimum value of Johnson noise is obtained as $i_{Johnson}|_{w=0} = \frac{4k_B T_0}{R_0}\frac{G_{TES}}{G_{ETF} + G_{TES}}$, which shows that in the low frequency range, the Johnson noise is reduced when G_{ETF} increases. This corresponds to situations when large values of α or large values of Joule power that increase G_{ETF} are used.

From equation (3.37), the module of the phonon noise current is expressed as:

$$i^2_{phonon}(\omega) = \left(\frac{\alpha I_0}{G_{TES}T_0}\right)^2 \frac{\left(p_{TES-phon} + 2p_{abs-phonon}\right)^2 + \omega^2\tau^2_{abs}\left(p_{TES-phon} + p_{abs-phon} + G_{TES}T_{bath}\right)^2}{|S(\omega)|^2} \tag{3.39}$$

The module of the phonon noise current results in:

$$i^2_{phonon}(\omega) = \frac{4k_B T_0}{R_0}\frac{P_{Joule}\alpha^2}{G_{TES}T_0}\frac{G_{abs}}{G_{TES}}\frac{\left[4 + \frac{G_{TES}}{G_{abs}} + \omega^2\tau^2_{abs}\left(1 + \frac{G_{TES}}{G_{abs}}\right)\right]}{|S(\omega)|^2} \tag{3.40}$$

The phonon noise presents the maximum value in the low frequency range and it has the dominant contribution to the total noise in this region. In the high frequency range ($\omega \rightarrow \infty$) the phonon noise goes to zero, because S(ω) is a function of ω^2 and the nominator in equation (3.40) is a function of ω (Fig. 3.7).

The analytical expressions derived for the current noise components can be compared with the power spectrum of the signal. Equation (3.32) does not include the initial conditions. The signal in this case is obtained by the Fourier-transform of equation (3.27), which results in an expression that depends on the rise and decay times of the pulse:

$$i_{signal}(\omega) = -\frac{\alpha I_0}{T_0}\frac{E_{total}G_{abs}}{\sqrt{A^2 - B}}\left[\frac{\tau_d}{1 + j\omega\tau_d} - \frac{\tau_r}{1 + j\omega\tau_r}\right] \tag{3.41}$$

with the module

$$i^2_{signal}(\omega) = \left(\frac{\alpha I_0}{T_0}\right)^2 \frac{\left(E_{total}G_{abs}\right)^2}{A^2 - B}\frac{\left(\tau_d - \tau_r\right)^2}{\left(1 - \omega^2\tau_d\tau_r\right)^2 + \omega^2\left(\tau_d + \tau_r\right)^2} \tag{3.42}$$

Equation (3.45) is plotted on the same graph comparatively with the total noise current components determined previously with P_{Joule} = 10 pW and G_{abs}/G_{TES} = 10 (Fig. 3.7). For $\tau_r << \tau_d$ (negligible rise time by comparison to τ_d), the frequency spectrum of the signal reduces to that given by equation (3.8) for the simple calorimeter model.

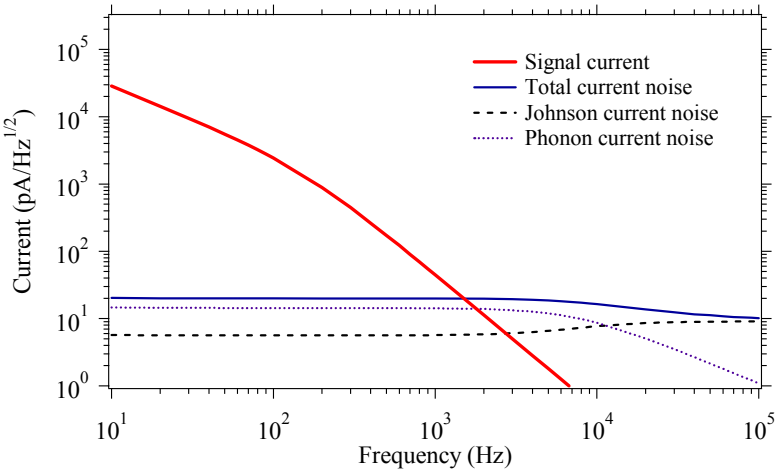

Figure 3.7. Signal and total noise current comparison in a neutron calorimeter. G_{abs}/G_{TES} = 10 at T=140 mK with C_{abs} = 1 nJ/K, C_{TES} = 50 pJ/K.

3.4.3 The energy resolution of a composite calorimeter

An analytical expression for the energy resolution is obtained based on the integral over the noise equivalent power as in equation (3.14). The only difference compared to the simple calorimeter model lies in the complexity of the NEP term. The total current noise is expressed as:

$$i^2_{composite}(\omega) = i^2_{Johnson}(\omega) + i^2_{phonon}(\omega) \tag{3.43}$$

Using equation (3.46) and the expression for $T_{TES}(\omega)$

$$T_{TES}(\omega) = \frac{NEP(\omega)}{S(\omega)} = -\frac{T_0}{I_0\alpha} i_{composite}(\omega) \tag{3.44}$$

it results that NEP(ω) can be expressed as:

$$NEP^2(\omega) = \left(\frac{T_0 S(\omega)}{I_0\alpha}\right)^2 i^2_{composite}(\omega) \tag{3.45}$$

$$NEP^2(\omega) = NEP^2_{phonon}(\omega) + NEP^2_{Johnson}(\omega) \tag{3.46}$$

with

$$NEP^2_{phonon}(\omega) = 4k_B T_0 G_{abs}\left[4 + \frac{G_{TES}}{G_{abs}} + \omega^2\tau^2_{abs}\left(1 + \frac{G_{TES}}{G_{abs}}\right)\right] \tag{3.47}$$

$$NEP^2_{Johnson}(\omega) = 4k_B T_0 \frac{T_0 G^2_{TES}}{G_{ETF}\alpha}\left\{\left(\omega^2\tau_{abs}\tau_{TES} + \frac{G_{ETF}}{G_{TES}} - 1\right)^2 + \omega^2\left[\tau_{TES} + \tau_{abs}\left(1 + \frac{G_{abs} - G_{ETF}}{G_{TES}}\right)\right]^2\right\} \tag{3.48}$$

In order to calculate the energy resolution with the integral in equation (3.15), the terms in equations (3.47) and (3.48) are grouped according to the powers of ω. The NEP(ω) term is then written in a general form as:

$$NEP^2(\omega) = a\omega^4 + b\omega^2 + c \tag{3.49}$$

where the parameters a,b and c are given by:

$$a = 4k_B T_0^2 G_{TES} \frac{G_{TES}}{G_{ETFe}\alpha}(\tau_{abs}\tau_{TES})^2$$

$$b = 4k_B T_0^2 G_{TES} \frac{G_{TES}}{\alpha G_{ETF}}\left[2\tau_{abs}\tau_{TES}\left(\frac{G_{ETF}}{G_{TES}}-1\right)+\left(\tau_{TES}+\tau_{abs}\left(1+\frac{G_{TES}}{G_{abs}}-\frac{G_{ETF}}{G_{TES}}\right)\right)^2\right]+$$

$$+4k_B T_0^2 G_{abs}\left(1+\frac{G_{TES}}{G_{abs}}\right)\tau_{abs}^2$$

$$c = 4k_B T_0^2 G_{abs}\left(4+\frac{G_{TES}}{G_{abs}}\right)+4k_B T_0^2 \frac{G_{TES}}{\alpha}\left(1-\frac{G_{TES}}{G_{EFT}}\right) \tag{3.50}$$

with $\tau_{TES} = C_{TES}/G_{TES}$ and $\tau_{abs} = C_{abs}/G_{abs}$. In the limits of the single thermal mass calorimeter, when $C_{TES} \rightarrow 0$ and $G_{abs} \rightarrow \infty$, the product $\tau_{abs}\tau_{TES} \rightarrow 0$ and the parameter a becomes equal to zero. The parameters b and c take a simpler form:

$$b_1 = 4k_B T_0^2 G_{TES} \frac{G_{TES}}{\alpha G_{ETF}}\left(\tau_{TES}+\tau_{abs}\left(1-\frac{G_{ETF}}{G_{TES}}\right)\right)^2 \tag{3.51}$$

$$c_1 = 16k_B T_0^2 G_{abs} + 4k_B T_0^2 \frac{G_{TES}}{\alpha}\left(1-\frac{G_{TES}}{G_{ETF}}\right) \tag{3.52}$$

In this case, NEP(ω) results in a simple form, i.e. $NEP^2(\omega) = b_1\omega^2 + c_1$, which has the same quadratic frequency dependence as equation (3.16). However, the exact calculation of the energy resolution with NEP(ω) given by equation (3.49) is not always necessary for the composite calorimeter and the term in ω^4 can be neglected since it only plays a role for frequencies above $1/\tau_r$ while most of the signal is at lower frequencies (Fig. 3.8).

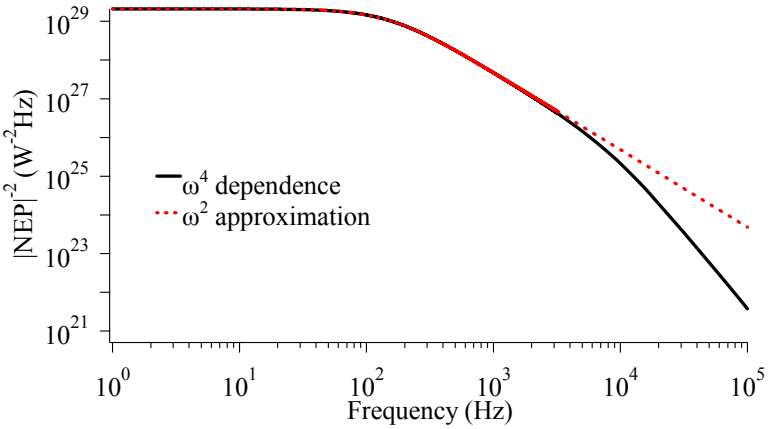

Figure 3.8. Numerical comparison of the energy resolution integrand $1/|NEP|^2$ for the ω^4 dependence and the ω^2 approximation.

The energy resolution is again obtained by integrating over the NEP according to:

$$\frac{1}{\Delta E_{FWHM}^2} = \frac{1}{(2.355)^2}\frac{1}{b}\int_0^\infty \frac{4d\omega}{\omega^2 + \frac{c}{b}} \tag{3.53}$$

The FWHM energy resolution results in:

$$\Delta E_{FWHM}^2 = (2.355)^2 \frac{2}{\pi}\sqrt{bc}\,. \tag{3.54}$$

Equation (3.54) can be written similarly to equation (3.18) as:

$$\Delta E_{FWHM} = 2.355\xi\left(k_B T^2 C_{abs}\right)^{1/2} \tag{3.55}$$

with ξ being a function of the parameters b and c in equation (3.50). A plot of equation (3.55) is presented din Fig. 3.9 as function of C_{abs} for different values of the thermal conductances G_{abs} and G_{TES}. Above $C_{abs} \approx 0.1$ nJ/K, the energy resolution of the composite calorimeter is reduced below $\Delta E_{FWHM} = 2.355\left(k_B T^2 C_{abs}\right)^{1/2}$ because of the electro-thermal feedback.

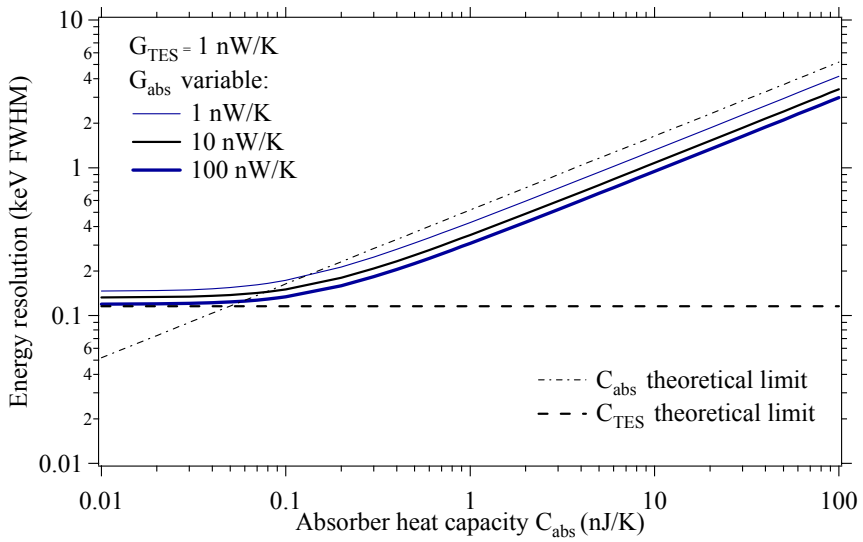

Figure 3.9. Energy resolution as a function of absorber heat capacity for different values of G_{abs} with G_{TES} = 1 nW/K, C_{TES} = 50 p J/K, P_{Joule} = 10 pW at T = 140 mK held constant in this simulation.

When $C_{abs} << C_{TES}$, the energy resolution becomes limited by C_{TES} which becomes the only thermal mass left in the system. In this case, ΔE_{FWHM} levels off and it has a value equal to $2.35\sqrt{4k_B T_0^2 C_{TES}/\alpha}$. When $C_{abs} >> C_{TES}$, ΔE_{FWHM} is directly proportional to $2.355\left(k_B T^2 C_{abs}\right)^{1/2}$, with a correction factor $\alpha^{-1/2} < \xi < 1$. For practical applications, a heat capacity C_{abs} = 1 nJ/K but no larger than 10 nJ/K is optimal for obtaining an energy resolution on the order of 0.5 – 5 keV FWHM corresponding to a temperature rise in the absorber on the order of 0.7 mK, which is within the limits of the transition width of the TES.

The change in energy resolution as a function of the thermal conductance ratio G_{abs}/G_{TES} for constant C_{abs} and C_{TES} is presented in Fig. 3.10 which shows that the energy resolution levels off when $G_{abs}/G_{TES} > 1$. In this range, the energy resolution lies below the $2.355\left(k_B T^2 C_{abs}\right)^{1/2}$ value. For practical purposes, a ratio G_{abs}/G_{TES} = 10 is already sufficient for the design of a composite neutron calorimeter. Conversely, $G_{abs}/G_{TES} < 1$

energy resolution is degraded due to increased phonon noise injected in the TES from G_{TES}.

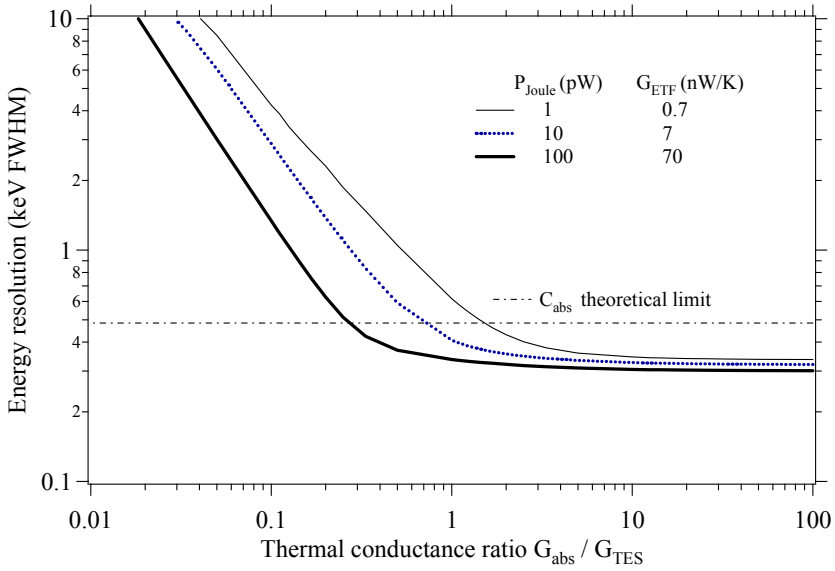

Figure 3.10. Energy resolution as a function of the thermal conductances for different levels of Joule power and thus different degrees of ETF. C_{abs} = 1 nJ/K, C_{TES} = 50 p J/K and G_{TES} = 1 nW/K at T = 140 mK are held constant.

3.4 Optimization of the neutron calorimeter

The design optimization of a fast-neutron detector requires a trade-off between high energy resolution, high detection efficiency and high count rate capabilities. For fast-neutron spectroscopy, one could ideally like to attain:

- An energy resolution on the order of 1 – 10 keV FWHM in order to detect the effect of interaction resonances in the neutron spectrum;
- Detection efficiency of at least a few percent for MeV neutrons
- Count rates well above 10 Hz per pixel.

The three requirements require a tradeoff that depends on the particular application. On one hand, the energy resolution is improved when operating at low temperature T to reduce the heat capacity C_{abs} and with the ξ value in the minimum. The predictions made

based on Fig. 3.9 and Fig. 3.10 show that the theoretical energy resolution can be reduced below 1 keV FWHM.

On the other hand, the intrinsic detection efficiency of a cubic absorber with volume $V = L^3$ is given by $\varepsilon_{int} \approx 1- \exp(-N\sigma L)$, and it must be maximized in order to increase the detection efficiency and the count rate. The resolving power is calculated as $E/\Delta E_{FWHM}$ in which the heat capacity C_{abs} is proportional to the volume of the absorber. Fig. 3.11 shows that in order to increase the resolving power in the fast-neutron region, the volume of the absorber must decrease, which in turn reduces the detection efficiency. At the operation temperature T, the lower the number of moles n, the lower the ΔE. One way to reduce n is with an absorber that has a large value of the molar mass M but the disadvantage is that in general, the atomic number Z of the compound is also large. Elements with high Z such as Ti have large gamma-ray production rates from radiative capture and inelastic scattering and also large μ/ρ photon absorption coefficients which can increase the parasitic gamma-ray self-absorption. An insulator material such as LiF has the property that the heat capacity per unit volume is much lower compared to a metallic compound such as TiB_2 [Kit 99]. A comparison of the heat capacities of metallic TiB_2 and insulating LiF is made in order to understand what material is the best choice from the point of view of the size and efficiency with respect to the energy resolution optimization.

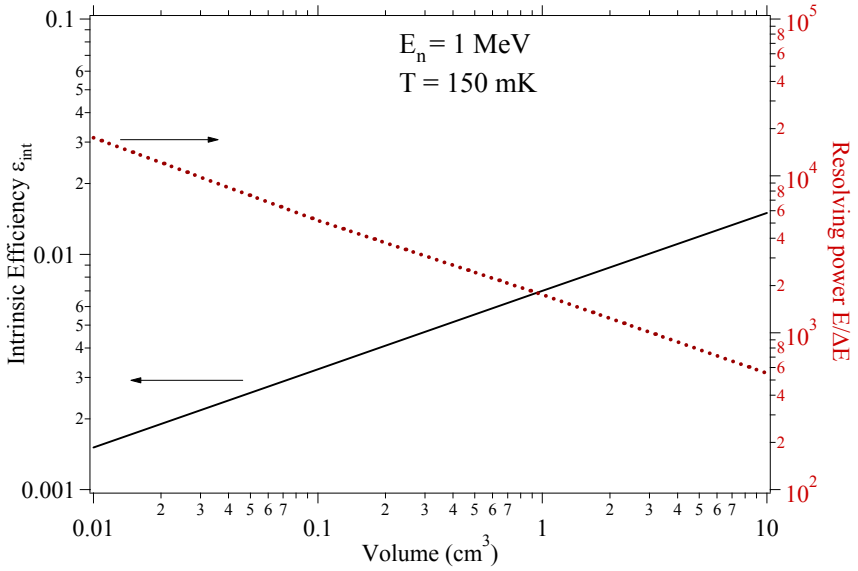

Figure 3.11. Intrinsic detection efficiency (left axis, solid curve) and resolving power (right axis, dotted curve) as a function of absorber volume at T = 150 mK for fast neutrons with E_n = 1 MeV.

The heat capacity of a solid-state absorber has two components, the electronic heat capacity, which varies linearly with the temperature, and the lattice heat capacity, which is described by the Debye's T^3 law [Kit 99]:

$$C_{total} = C_{electron} + C_{lattice} = n\gamma\gamma + 234nR\left(\frac{T}{\theta_D}\right)^3 \tag{3.56}$$

γ is the specific electronic heat capacity which has a finite value in a metal such as TiB_2 but which becomes zero in insulators such as LiF. Thus, the heat capacity of insulators is described purely by the Debye's law, which depends on the number of moles $\eta = m/M$ for a material with molar mass M, on the universal gas constant R and on the Debye temperature of the crystalline lattice θ_D.

Normalized C_{total} to the number of moles results in the total specific heat capacity c_{total} (J/mol·K): which is independent on the amount of material

$$c_{total} = C_{total}/n = \gamma T + \beta T^3 \tag{3.57}$$

The values for β and γ are taken from experimental heat capacity measurement of TiB_2 and LiF crystals [Lan 05].

Table 3.1. Specific thermal parameters of LiF and TiB_2 crystals

	β (mJ/K^2/mol)	**γ (mJ/K^4/mol)**
TiB_2	$3.403\times10^{-3} \pm 0.070\times10^{-3}$	$1.001\times10^{-3} \pm 0.019\times10^{-3}$
LiF	9.187×10^{-6}	0

At the same temperature T, the specific heat capacity of LiF is a factor of about 300 larger than for TiB_2, driven by the β parameter in Table 3.1.

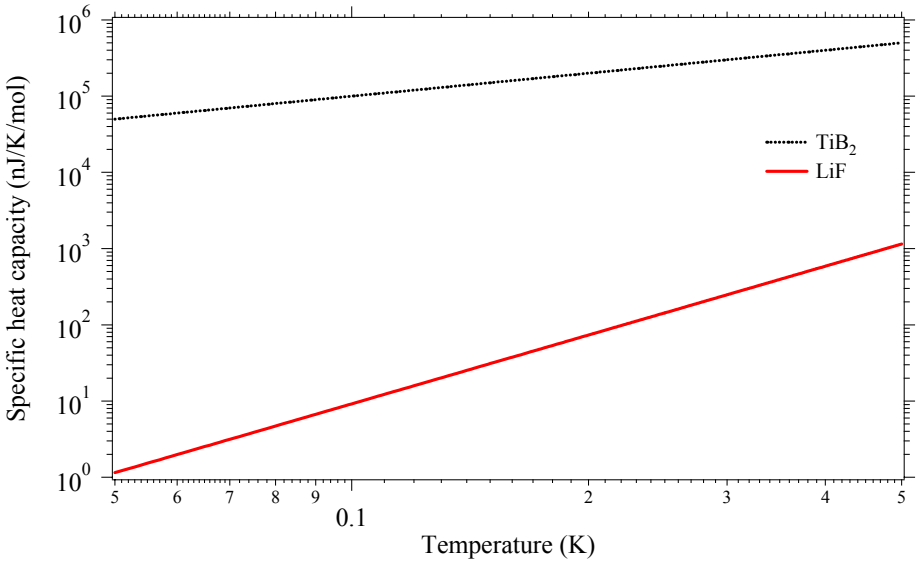

Figure 3.12. Specific heat capacity comparison of TiB_2 and LiF.

Imposing the same heat capacity for both materials, the volume of LiF is related to the volume of TiB_2 with the following expression:

$$\frac{V_{LiF}}{V_{TiB_2}} = \frac{n_{LiF}}{n_{TiB_2}} \frac{M_{LiF}}{M_{TiB_2}} \frac{\rho_{TiB_2}}{\rho_{LiF}} \tag{3.58}$$

The specific heat capacity dependence on temperature of LiF and TiB_2 absorbers is calculated with values for β and γ from Table 3.1.

A numerical example in which the required heat capacity of the absorber is of 1 nJ/K is considered for a theoretical energy resolution of about 0.3 keV FWHM from Fig. 3.9. With C_{abs} = 1 nJ/K, the temperature increase is of about 0.7 mK, which is in the range of the superconducting transition width of the TES sensor. At T = 140 mK, the same heat capacity is obtained with either $n_{TiB2} = 7.1\times10^{-6}$ moles of TiB_2 with a volume of 0.2 mm^3 or with $n_{LiF} = 3.9\times10^{-2}$ moles of LiF with a volume of about 0.7 cm^3. The intrinsic detection efficiency of the 0.7 cm^3 LiF absorber calculated at 1 MeV is a factor of 10 larger than in 0.2 mm^3 TiB_2. Although the theoretical energy resolution of the two materials is identical for the same heat capacity, the LiF absorber has the advantage of higher detection efficiency. This supports the use LiF for fabricating and testing a high detection efficiency calorimetric neutron spectrometer with theoretical energy resolution on the order of a few keV FWHM.

Chapter 4. Experimental Setup

This chapter describes the experimental implementation, the data acquisition system, the cryostat for detector operation at temperatures of 0.1 K and calibration sources.

4.1 TES thermistor fabrication

The microscopic theory of superconductivity developed by Bardeen, Cooper and Schrieffer (BCS) states that below the critical temperature T_c, the electrons can bind in so-called Cooper pairs, due to an attractive force mediated by the polarization of the lattice [Bar 57]. The total binding energy of a Cooper pair $2\Delta = 3.5k_BT_c$ results in an energy gap 2Δ in the density of states at the Fermi energy that is larger than the energy of typical electron-electron or electron-lattice scattering event. As a result, below T_c, the Cooper pairs travel through the lattice without scattering, which translates into zero electrical resistance and hence the phenomenon of superconductivity.

The energy resolution of superconducting calorimeter detectors improve with lower operating temperature i.e. with decreasing critical temperature T_c. An operating temperature around 0.1 K is a good compromise between high energy resolution and ease of operation. Unfortunately, no elemental superconductor has a critical temperature at this range. A method to decrease the T_c of a pure superconducting material such as Mo is to combine it with a metal such as Cu, which does not exhibit superconducting properties. When two such films are deposited on top of each other, the overall T_c is lowered due to the so-called proximity effect [Tin 04]. For use in TES calorimeters, the proximity effect can be produced in Mo/Cu bilayers consisting of a single film of Mo and Cu, or in multilayers consisting of many alternating layers of Mo and Cu. The resulting T_c depends

only on the Mo/Cu thickness ratio and the quality of the interface (Fig. 4.1a) [Mar 00]. Note that Mo and Cu are not the only normal-superconducting material combinations that can be used. Other groups have used other normal-superconductor materials combinations such as Mo/Au, Ir/Au or Al/Ag [Wol 00], [Hoh 99], [Hol 98], Eva 77], [Cha 81]. We use Mo/Cu, because the two materials do not form intermetallic phases and thus remain stable over years of storage and thermal cycling. We favor multilayers over the much simpler bilayers, because T_c and the normal resistance R_n can be adjusted independently (Fig. 4.1b).

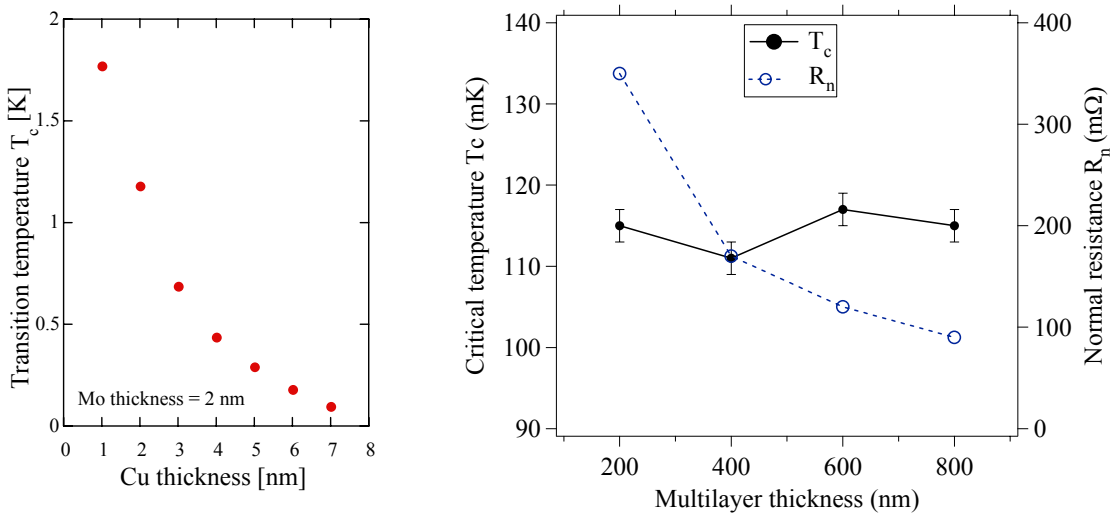

Figure 4.1 a) Dependence of T_c on the thickness of the Cu layer for a multilayer TES. b) Multilayers with different thicknesses have different resistances and the same T_c, provided the Mo/Cu ratio is constant.

The Mo/Cu multilayers are fabricated by standard photolithography at the Lawrence Livermore National Laboratory Microtechnology Center and the Advanced Detector Group. We use a TES with 23 layers of Cu (7 nm each) deposited by magnetron sputtering alternately with 20 layers of Mo (2 nm each) on 0.5 µm of SiN a Si substrate. For our 200 nm Mo/Cu multilayer, the T_c varies between 110 mK – 150 mK and the

normal electrical resistance is R_n = 350 mΩ [Ali 05]. The typical area of the TES is 0.5 mm × 0.5 mm and a top view of the Si chip is shown in Fig. 4.2.

For some TES, the Si underneath is etched away, leaving the TES on a free-standing SiN membrane which sets the thermal conductance G_{TES} to the cold bath. For others, the Si is not etched away, in which case the mounting scheme of the chip with the TES in the cryostat sets the thermal conductance. For devices on a SiN membrane, the mechanical properties of the SiN sets the upper limit of about 5 mg of absorber mass that can be attached to TES 1 (device TES-1 in Fig. 4.2). By comparison, TESs on a solid substrate (device TES-2) can be attached to larger absorbers. Practically, space constraints of the cryostat and concerns about spatial variations of the detector response limit the volume of a single neutron absorber to several cm^3.

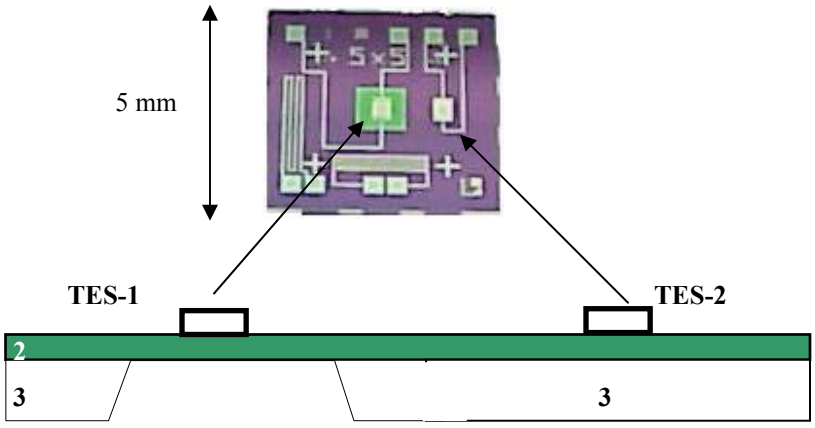

Figure 4.2 Picture of a multilayer Mo/Cu TES chip. The central device (TES 1) is deposited on a SiN membrane (2) and a second device (TES 2) is deposited on a rigid SiN/Si substrate (3).

.

4.2 Fabrication of Neutron Spectrometers

We have fabricated two types of neutron spectrometers using TESs from the chip shown in Fig 4.2. A small TiB_2 absorber with a mass of 2.3 mg whose weight can be supported by the SiN membrane, has been glued with epoxy (Stycast 2850FT) onto the TES. The resulting device and a schematic is presented in Fig. 4.3. The Si chip is glued with silver paint on a alumina chip holder with gold traces for wirebonding to the electronic read-out. The assembly is mounted at the end of a cold finger at 0.1K. The device with the TiB_2 absorber can be modeled as a simple calorimeter as discussed in Section 3.2.

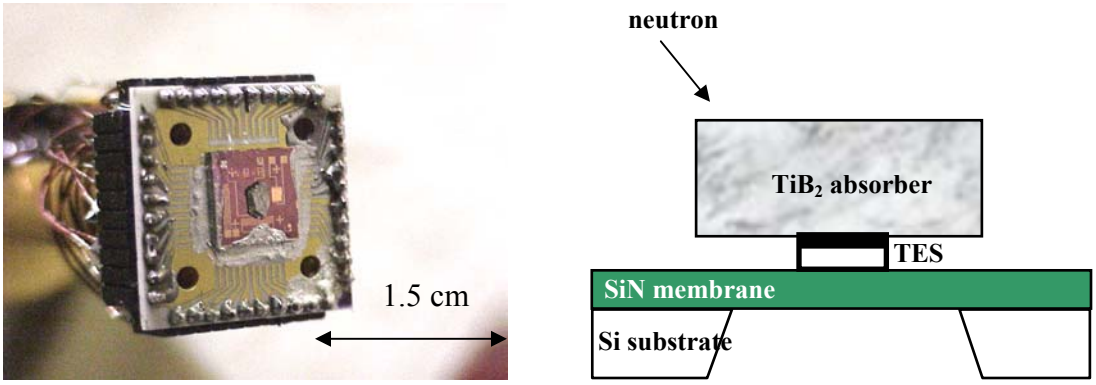

Figure 4.3. Left: TiB_2 absorber (irregular shape in the center) installed on a TES on a SiN membrane. Right: Schematic of TiB_2 detector.

For large volume LiF absorbers, the TES-2 in Fig. 4.2 has been used. In order to reduce the heat capacity of the Si chip, it has been cut to one third of the original chip size in Fig. 4.2. The Si chip has been glued with GE varnish onto the LiF absorber, which creates the G_{abs} interface. G_{TES} is set by the Au bond wire with a diameter of 25 μm and a length of 2 cm, which sets the thermal conductance limit.

Figure 4.4. TES neutron detectors with large volume LiF absorbers and their low-temperature support structure. All absorbers are mounted on screws with spring-loaded Teflon plungers with low thermal conductance. Note the different scale in the two pictures.

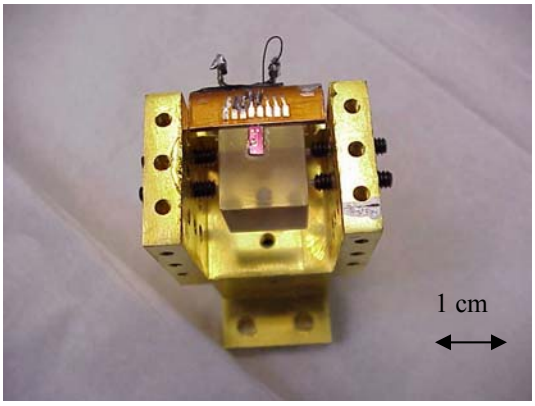

A. Neutron detector with a large natural LiF absorber (3.25 cm^3), with the Si chip with the TES attached with GE varnish. The thermal conductance between the TES and the cold bath is set by the Au wires. The holder can host a crystal of up to 8.5 cm^3 in size.

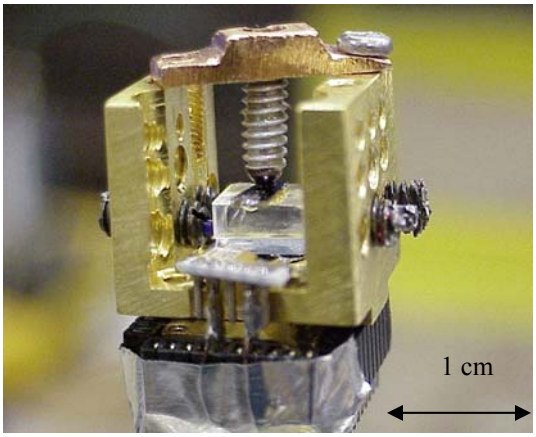

B. Neutron detector with an enriched ^{6}LiF absorber (0.25 cm^3) whose thermal conductance to the cold bath is controlled by an Al screw coated with stycast. This holder can host a crystal of up to 2 cm^3 in size.

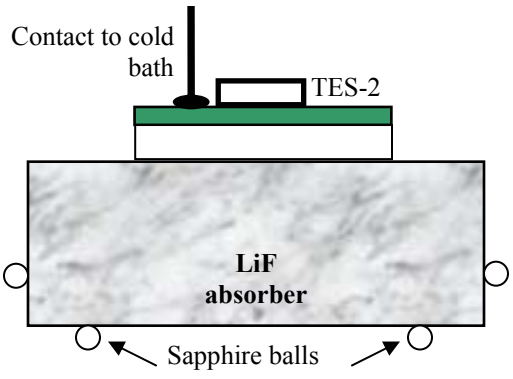

C. Schematic of the detector with the relative position of the TES and the absorber.

To improve the thermal conductances G_{abs} and G_{TES}, especially during cooldown, a second detector design employed an epoxy-coated Al screw to mechanically press the Si

chip against the LiF absorber. Al is a normal metal with high thermal conductance during cooldown, whose conductance decreases significantly below its superconducting transition at 1.1 K. Due to the presence of the Si chip, in both designs with large absorbers, C_{TES} can no longer be neglected by comparison with C_{abs}, in which case, the composite calorimeter model applies.

In order to increase the thermal conductance G_{abs} between absorber and TES for improved energy resolution, we have attempted to deposit Mo/Cu TES bilayers directly onto LiF crystals. For that, Mo strips with thicknesses between 20 and 55 nm were first deposited on LiF through shadow masks, followed by 200 nm of Cu over the central part of the strip.

Figure 4.5 shows comparatively two representative transitions of different TESs. The Mo/Cu bilayers deposited on SiN/Si substrates have narrow transitions with a sensitivity $\alpha \approx 50$, while similar bilayers deposited on a LiF crystal exhibit a wider transition with $\Delta T_c \sim 250$ mK and lower sensitivity $\alpha \approx 5$. Such Mo/Cu bilayer TES cannot detect temperature variations on the order of 1 mK for typical neutron interactions with sufficiently high signal-to-noise ratio.

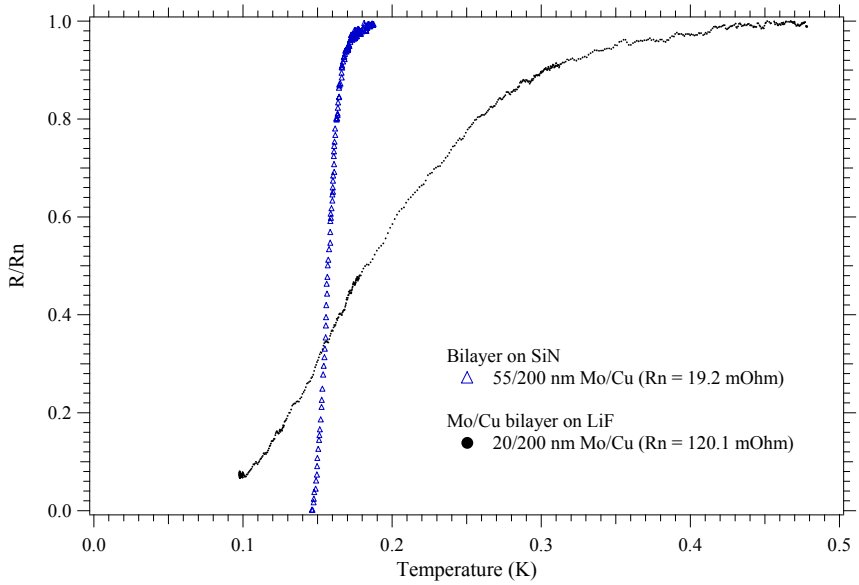

Figure 4.5. Superconducting transition comparison of Mo/Cu bilayers on SiN and on LiF.

The reason for the degraded transition on LiF is due to the surface quality. Even when polished to high optical quality, the surface roughness of the LiF crystals still is on the order of hundreds of nm root-mean-square (RMS) measured by Atomic Force Microscopy (AFM) (Fig. 4.6).

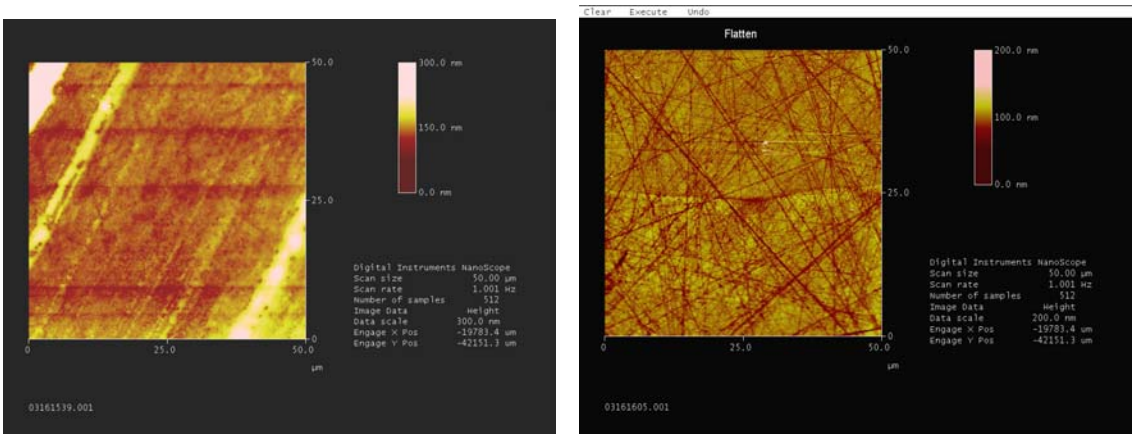

Figure 4.6. AFM measurements of LiF crystal surfaces. Left: LiF crystal polished about 6 years before the date of the measurement shows blurred features due to hygroscopic nature of LiF. Right: LiF crystal polished to optical quality a month before the measurement presents sharp features.

This surface roughness of LiF crystals implies that a Mo film nominally 20 nm thick varies in fact widely in thickness since it follows the polishing grooves and the relief on the LiF surface, resulting in wide variations in Tc due to the proximity effect with the top Cu layer. Additionally, the hygroscopic nature of LiF causes problems with the stability of metal deposition in time (Fig. 4.7). Unfortunately, the attempt to deposit TESs directly on the LiF absorbers was unsuccessful and therefore abandoned.

4.3 TES read-out and electronics circuit

To read out high resolution signals from a low impedance TES, a Superconducting Quantum Interferometer Device (SQUID) amplifier is used to convert the current signals ΔI into voltage output ΔI (Fig. 4.7).

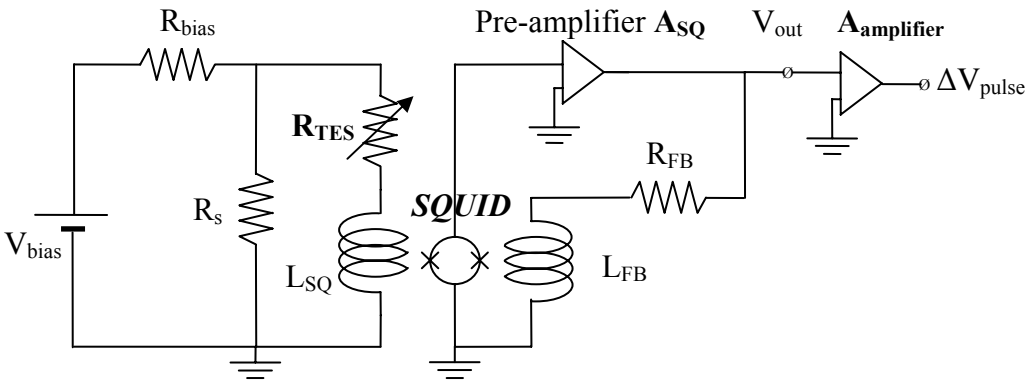

Figure 4.7. Schematic of the electronic read-out circuit of the TES. R_{TES} and R_s are at 0.1 K while V_{bias}, R_{bias}, R_{FB} and A_{pre} are at room temperature. The SQUID amplifier, its input coil L_{SQ} and its feedback coil L_{FB} are ~ 1.2 K.

The SQUID amplifier is a sensitive magnetic flux-to-voltage converter based on the Josephson tunneling effect [Cla 04]. The superconducting 350 nH input coil of the SQUID converts the current into a magnetic flux that is retrieved as a voltage in the

output coil with an amplification factor $A_{SQ} = 43$. The SQUID used in our experiments is a commercial DC SQUID from Supracon AG in Jena, Germany [Sup 06].

A shunt resistor $R_s << R_{TES}$ is placed in parallel with R_{TES} to obtain a constant bias voltage across the TES. R_s and R_{TES} are both operated at 0.1 K while the SQUID preamplifier and its input and feedback coils are operated at ~1 K. The current variation in the TES in response to neutron absorption is converted into a magnetic flux and sensed by the input coil of the SQUID, which is in series with R_{TES} and is operated in feedback locked-loop through R_{TES} and L_{FB}. The $R_{TES}L_{FB}$ circuit acts as a low-pass filter with a cutoff frequency of about 570 kHz which does not affect the signal from the detector. At room temperature, the SQUID preamplifier output pulse is further amplified by a commercial Stanford Research Systems amplifier.

The electrical wiring between the low temperature stage at 0.1 K and higher temperature stages at 1 K and 4.2 K is made with CuNi-clad quad-twist wires with low thermal conductance to reduce heating of the 0.1 K stage.

The current-voltage I(V) curve of the TES circuit is shown in Fig. 4.8 for a set of bath temperatures T_{bath} below T_c. The slope of the curve represents the inverse of the electrical resistance. Qualitatively, when very low V_{bias} of a few μA is applied, the TES is superconducting ($R_{TES} = 0$) and no Joule power is dissipated in the TES. The only non-zero resistances are $R_s = 5$ mΩ and an additional parasitic resistance R_p of a few mΩ coming from the soldering contacts of the wires. At higher V_{bias}, the TES enters the transition region of the TES where R_{TES} and the Joule power increases with T, and the current drops as a result. When the TES becomes normal ($R = R_n$ = constant) the slope is $(\partial I/\partial V)_{normal} = 1/R_n$.

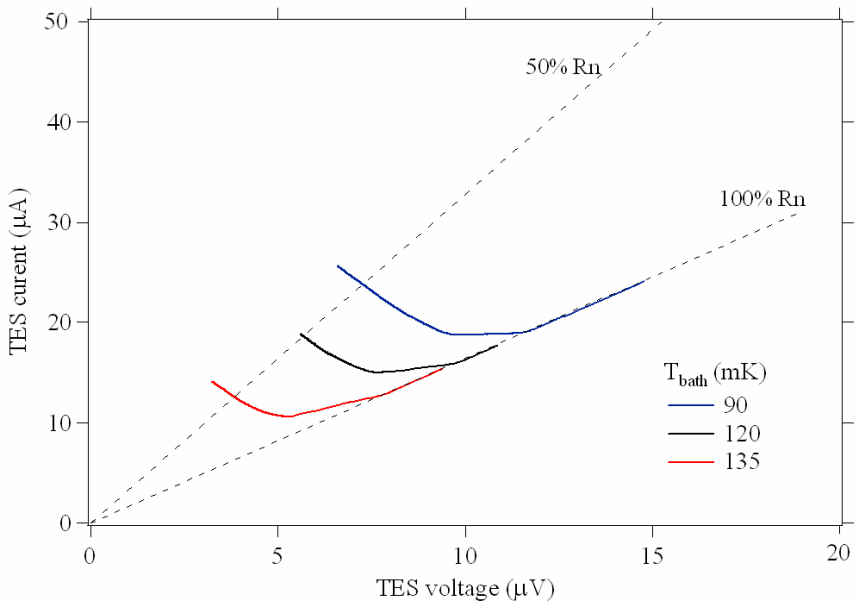

Figure 4.8. I(V) characteristics curve of a TES with T_c = 147.8 mK (Fig. 4.1) for three different values of the bath temperatures.

When T_{bath} increases, less Joule power is needed to bias the TES at the same resistance R in the transition, so that the curves with high I-V values correspond to lower T_{bath} and the curves with low I-V values correspond to higher T_{bath} values.

Each pulse from a detectable neutron interaction event is amplified by the SQUID electronics preamplifier and by the amplifier. Each pulse is then digitized with an Analog-to-Digital Converter installed on a GaGe® data acquisition board and then individually stored on a PC for further analysis (Fig. 4.9).

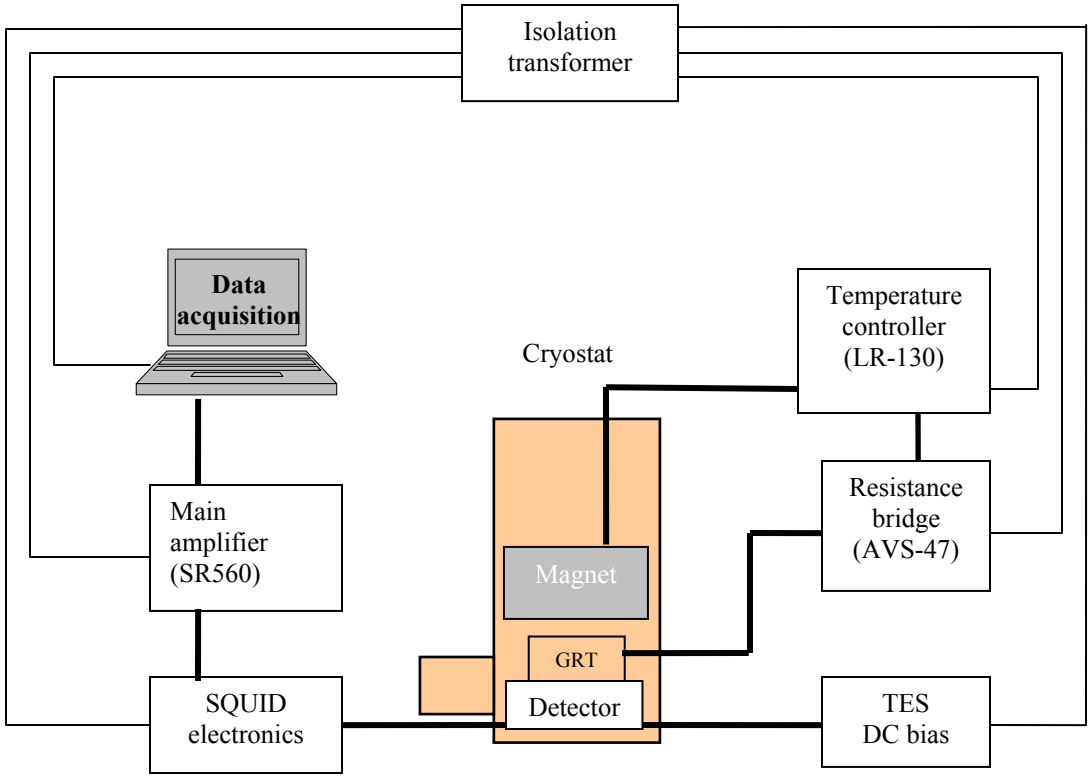

Figure 4.9. Read-out electronics circuit.

To reduce electromagnetic pick-up noise, the 300 K shell of the cryostat serves as a Faraday cage. In addition, the SQUID is mounted inside a superconducting Nb can, and the cryostat is surrounded with multilayer magnetic shielding made of Finemet® from Hitachi Metals [Hit 06]. The SQUID preamplifier box is directly connected to the cryostat and all readout wires inside and outside the cryostat are twisted in pairs to reduce pickup.

4.4 The Adiabatic Demagnetization Refrigerator

The required operating temperature of 0.1 K for the neutron detector obtained using the two-stage adiabatic demagnetization refrigerator (ADR) shown in Fig. 4.10 [Fri 01]. The

cryostat uses a nested design, similar to a Russian doll, with the outer high temperature stages shielding the inner low temperature stages. The cryostat is pre-cooled to 77 K using liquid nitrogen (LN_2) and cooled to 4.2 K with liquid helium (LHe). Two other low temperatures stages for cooling to 1 K and 0.1 K respectively, are mounted on Kevlar strings, and are initially kept at 4.2 K with an electro-mechanical heat switch in the closed position.

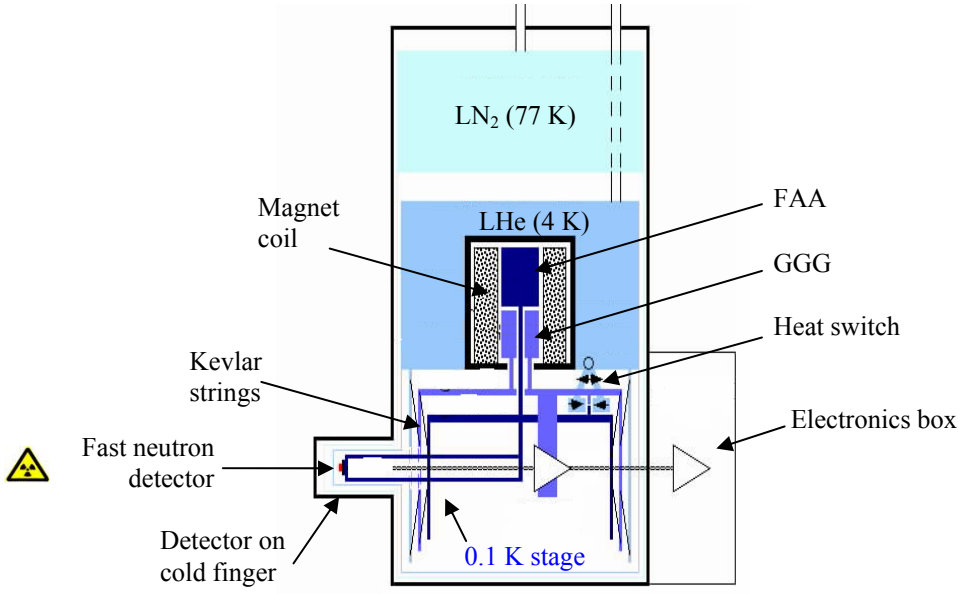

Figure 4.10. Cross section through the cryostat in the normal operation position

Cooling below 4.2 K is obtained with two paramagnets, namely ferric ammonium alum (FAA)[1] and gadolinium gallium garnet (GGG), both surrounded by a high-current superconducting magnet. The FAA pill cools one stage to a temperature of 0.1 K, while the GGG pill is used to cool the second stage to 1 K. Cooling is achieved by isothermal magnetization and adiabatic demagnetization process, as illustrated in Fig. 4.11 [Lou 74],

[1] $Fe_2^{3+}(SO_4)_3(NH_4)_2SO_4{\cdot}24H_2O$

[Pob 96]. A magnetic field of 5 T is applied to the salt pills using a superconducting magnet. This aligns the magnetic moments of the salt pill atoms and reduces their entropy S, with the heat of magnetization being removed isothermally through the closed heat switch. The mechanical heat switch is then opened to thermally decouple the 0.1 K stage from the rest of the cryostat and the magnetic field is slowly reduced adiabatically (S = constant). The minimum bath temperature T_{bath} attained is of about 70 mK, and it can be adjusted and stabilized by controlling the remnant magnetic field of the magnet. The magnetization-demagnetization cycle takes about 1.5 h, and the effective hold time is set by the heat load into the cold stage that determines the time to warm up from T_{bath} to the critical temperature T_c of the TES, which is typically between 12-14 h, after which the cycle has to be repeated.

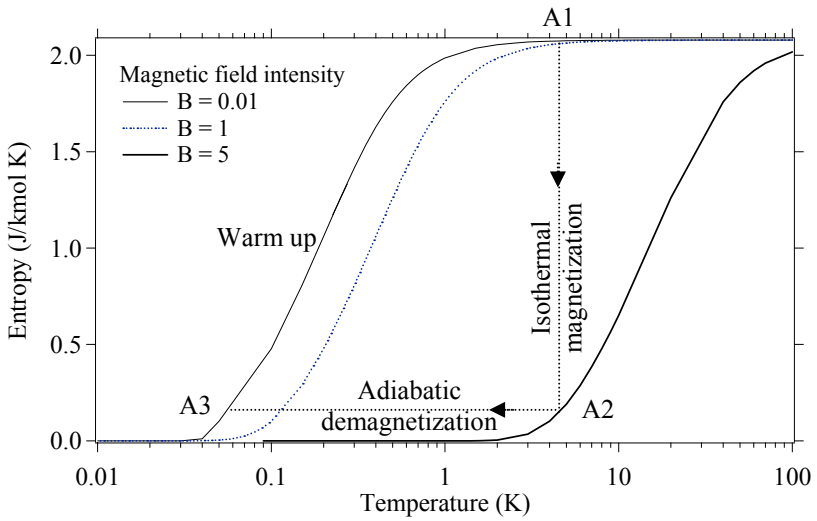

Figure 4.11. Entropy of an FAA salt pill as a function of T and B according to Brillouin function [Pob 96]. Adiabatic magnetization-demagnetization cycle: A1-A2 isothermal magnetization, A2-A3 adiabatic demagnetization, A3-A1 slow warm-up.

Figure 4.12 shows a picture of the interior of the cryostat with the cover lids removed, as viewed from the bottom (cf. Fig. 4.10). Three concentric temperature shields are visible, held during the operation (from outside to the inside) at 300 K, 77 K and 4.2 K

respectively. The central rod is the cold finger, which is part of the 0.1 K stage suspended by Kevlar strings at the four suspension towers. The round structure to the left of the cold finger is the electro-mechanical heat switch used to make and break the thermal contact between the 0.1 K and 1 K stages with the He-cooled thermal reservoir at 4.2 K.

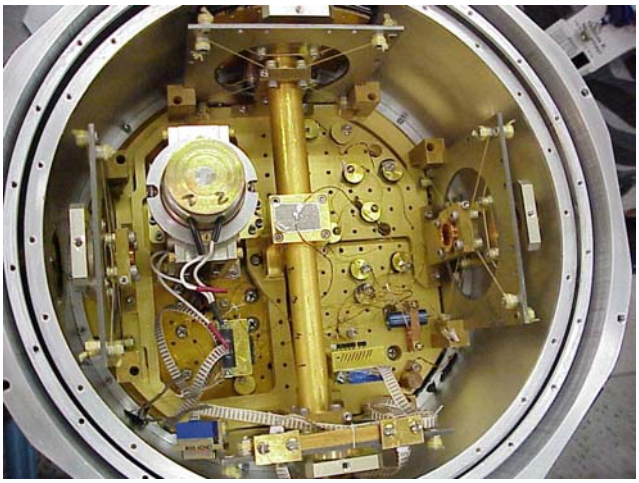

Figure 4.12. Photograph of the interior of the cryostat.

During the TES detector operation, the bath temperature must be regulated to a constant value. This is done with a commercial LR-130 temperature controller. The temperature is measured with a germanium resistance thermometer (GRT) from Lake Shore Cryotronics installed on the 0.1 K stage, using an AVS-47 resistance bridge from Picowatt and operated in the feedback mode with the LR-130 temperature controller [Lak 06], [Pic 06]. With this system, we have measured a temperature stability of the 0.1 K stage between 15 and 22 μK FWHM, which is sufficient to not affect the energy resolution of the spectrometer.

4.5 Neutron sources and shielding

In our experiments we have used ^{252}Cf as a neutron source. The activity of ^{252}Cf source is between a few μCi (class I) to 2 mCi (class IV), which require both neutron and gamma-ray radiation shielding. The neutron shield is made of bags of granulated borated polyethylene. In the configuration used for thermal neutron measurements (Fig. 4.13), 1 to 5 cm thick lead bricks provide gamma-ray shielding, and high-density polyethylene (HDPE) is used to thermalize the neutrons. For fast-neutron spectroscopy, the HDPE block and the lead brick between the source and the detector were removed.

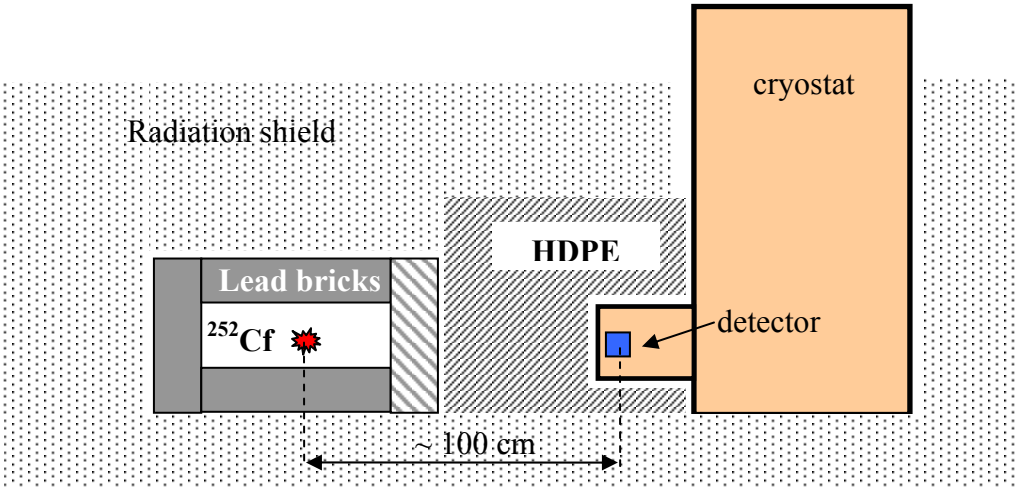

Figure 4.13. Measurement geometry for neutron spectroscopy. The approximate scale of the geometry is shown by the double arrow.

The neutron thermalization and gamma-ray production has been studied with MCNP simulations in the geometry shown in Fig. 4.13, in order to understand the input spectrum and to compare with the experimental results. For tests with heavy shielding and strong thermalization, the spectrum has a long tail that extends into the thermal and cold neutron region. For fast-neutron spectroscopy, the neutron thermalization is lower by a factor of 3. The presence of a sample in between the ^{252}Cf source and the spectrometer also alters the spectrum, which is quantified in the next Chapters on experimental results.

Chapter 5. Experimental results with a prototype TiB_2 device

5.1 Pulse and noise characteristics

We have built a neutron detector using a 2.3 mg TiB_2 absorber attached to a Mo/Cu TES on a SiN membrane (Fig. 4.3). TiB_2 is a metallic compound and even small volumes that can be supported on a SiN membrane have sufficiently high heat capacity that the TES is not driven off the transition when neutron interaction deposits several MeV of energy.

The purpose of this prototype detector is to demonstrate the feasibility of high-resolution neutron detection with a cryogenic detector with an energy resolution of a few keV FWHM.

We have operated this detector at a temperature T_c = 122 mK inside the cryostat and illuminated it with thermal neutrons from a 2 mCi ^{252}Cf neutron source shielded with HDPE as shown in Fig. 4.13. The operation parameters of this detector are summarized in Table 5.1.

Table 5.1 Operation parameters of the TiB_2 neutron spectrometer

Parameter	**Value**
TiB_2 absorber mass m	2.3 mg
Bath temperature T_{bath}	108 mK
Operating temperature T_c	122 mK
TES sensitivity α	70
Absorber heat capacity C_{abs}	3.59 nJ/K
TES heat capacity C_{TES}	10 pJ/K
SiN thermal conductance G_{TES}	1.0 nW/K
Bias resistance R_b	1.0 kΩ
Feedback resistance R_{FB}	1.0 kΩ
Shunt resistance R_s	5.0 mΩ
SQUID amplification A_{SQ}	43

At the operation temperature, C_{abs} = 3.59 nJ/K and C_{TES} = 10 pJ/K is three orders of magnitude smaller than C_{abs}. To examine how the energy resolution of this detector compares with theoretical models, we extract G_{abs} and G_{TES} from the observed I(V)

characteristics and pulse shapes using the simple calorimeter model of Section 3.3.1 in which $G = G_{TES}$ and $C = C_{abs}$. Both the rise and decay of the observed pulse waveforms can be described with single exponential function with τ_r =152 μs and τ_d =74.8 ms (Fig. 5.1).

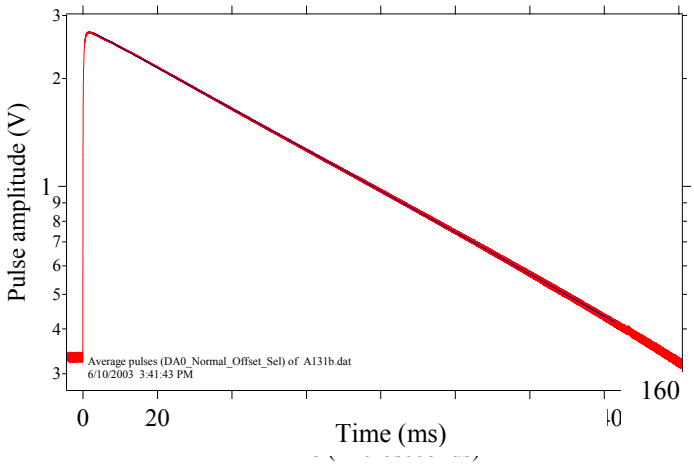

Figure 5.1 Average pulse obtained from a cryogenic neutron detector with a TiB_2 absorber on a logarithmic scale. The rise time fits with a single exponential function with a time constant τ_r =152 μs and the decay time fits a single exponential with a time constant τ_d =74.8 ms.

The electro-thermal feedback thermal conductance is $G_{ETF} = \alpha P_{Joule}/T_0 = 70 \times 60$ pW/122 mK = 34.5 nW/K. In the approximation given by equation (3.31), with $\tau_0 = C_{abs}/G_{TES}$ = 3.59 s, the effective decay time is of τ_d = 101.5 ms. The rise time is estimated with equation (3.28) in the composite calorimeter model to τ_r = 67 μs.

The temperature increase of the absorber is calculated from the pulse amplitude according to:

$$|\Delta T_{TES}| = \frac{V_b}{I_{TES}^2} \frac{\Delta V_{pulse}}{R_{FB} A_{SQ} A_{pre}} \frac{R_s}{R_s + R_b} \tag{5.1}$$

With a pulse amplitude ΔV_{pulse} = 2.2 V, α = 70, an amplification A = 50 and A_{SQ} = 43, we obtain ΔT_{TES} = 0.87 mK. The expected temperature rise from an energy deposition Q = 2.78 MeV in the TiB_2 absorber with C_{abs} = 3.59 nJ/K is 0.1 mK.

Shown in Fig. 5.2, the frequency spectrum of the experimental pulse extends to about 10 kHz due to the fast rise time component on the order of 0.1 ms. At 1 kHz, the theoretical total noise current predicts 35.5 pA/Hz$^{1/2}$, dominated by phonon noise. The experimental noise current at 1 kHz is 68.6 pA/Hz$^{1/2}$. The noise spectrum presents parasitic peaks at harmonics of 60 Hz, i.e. at 240 Hz and 540 Hz, which are due to interference from the power lines and EM pickup. However, the effect of the parasitic peaks is reduced during the optimal filter processing of the pulses.

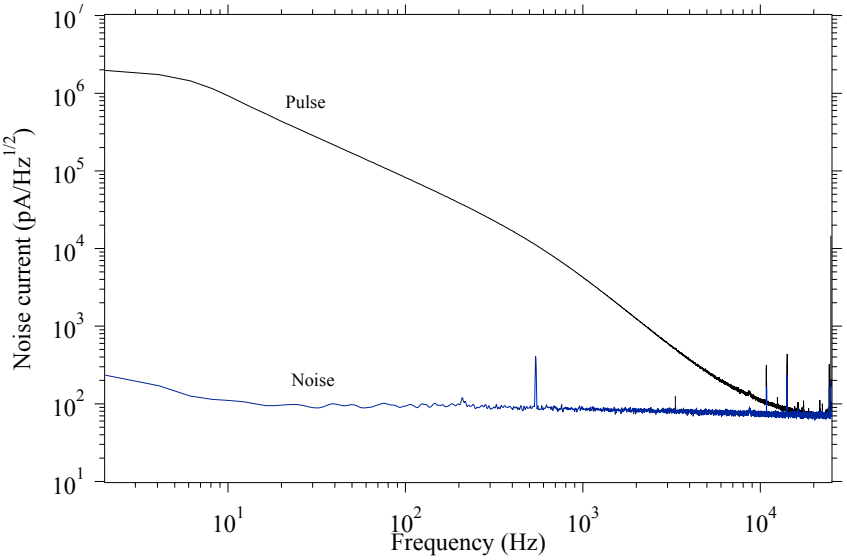

Figure 5.2. Experimental and theoretical pulse and noise current.

5.2 Energy resolution of the TiB_2 device

The experimental spectrum obtained with the TiB_2 detector exposed to thermal neutrons is presented in Fig. 5.3. The spectrum has a total number of 3349 events distributed in 3000 energy bins with a width of 1.1 keV each. Above 1 MeV, the spectrum presents the features expected from the MCNP-Polimi simulation (Fig. 2.26) with the two energy deposition peaks at 2.31 MeV and 2.78 MeV respectively, corresponding to the two channels in $^{10}B(n, \alpha)^7Li$ reaction. The 2.31 MeV peak has an integrated area of 3124 ± 56

counts, whereas the peak at 2.79 MeV has 225 ± 15 counts. The ratio of the number of counts in each peak to the total number of counts is of 96:4, as expected from the branching ratio of the $^{10}B(n, \alpha)^{7}Li$ reaction shown schematically in Fig. 2.1.

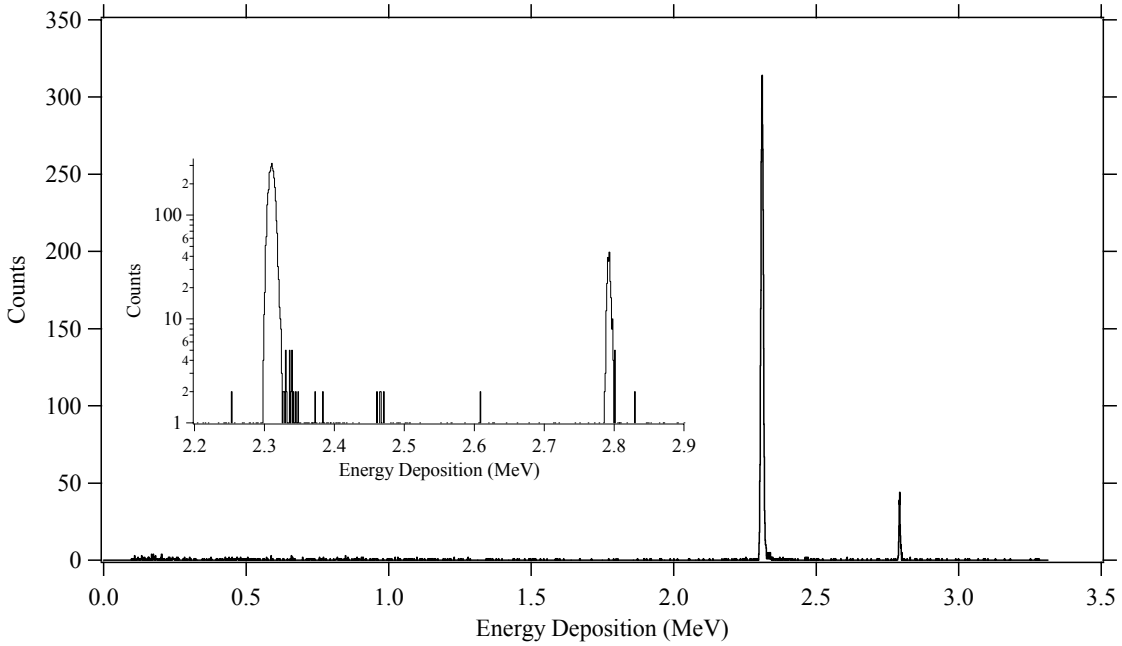

Figure 5.3 Response of the TiB_2 absorber to thermal neutrons. Note the low background and the lack of any other energy lines from capture or inelastic scattering. The inset shows the peak region on a vertical logarithmic scale.

The 2.79 MeV energy deposition line corresponding to the reaction leading to the ground state of ^{7}Li has an energy resolution of 5.5 keV FWHM from the Gaussian fit, which is considered the instrumental energy resolution (Fig. 5.4). The 2.31 MeV energy deposition line corresponding to the reaction that leads to the first excited state of ^{7}Li has an energy resolution of 10.5 keV FWHM [Nie 04].

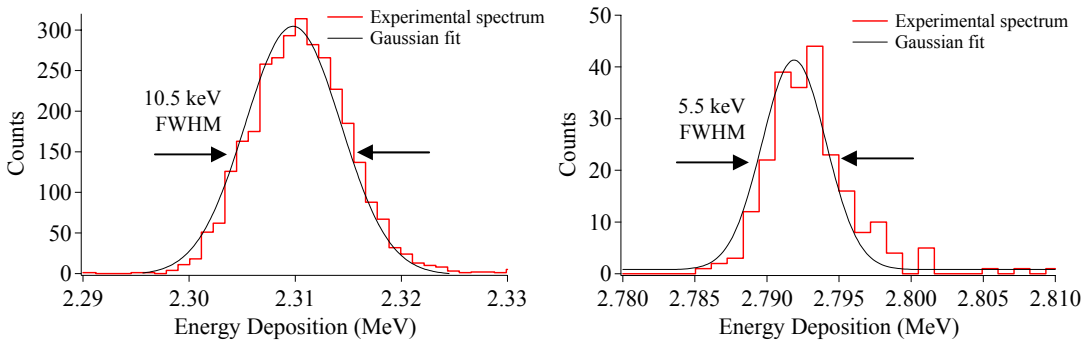

Figure 5.4. TiB_2 absorber response to thermal neutrons (energy deposition lines detail).

The larger width of the 2.31 MeV line is explained by the fact that the 478 keV gamma-ray is emitted from the first excited state of ^{7}Li. The gamma-ray emission produces variations in the energy deposited by the ^{7}Li recoil ion, which results in broader energy line. This broadening effect allows the measurement of the lifetime of the 478 keV energy level, which is described in detail in Section 5.3.

The broadening of the 2.31 MeV line from the instrumental energy resolution is calculated as $\Delta E_{broad} = \sqrt{10.5^2 - 5.5^2} = 8.90$ keV FWHM. Due to the linear energy response (within 2%) of the detector, we assume that the 5.5 keV FWHM instrumental energy resolution is uniform from zero up to 3 MeV.

In order to account for all possible broadening sources of the 2.31 MeV line, we examined the absorption of the neutron capture gamma-rays produced in the $^{48}Ti(n, \gamma)^{49}Ti$ reaction. This is the only reaction in TiB_2 that produces gamma-rays in the energy range about 2.31 MeV. The gamma-rays that can interfere with the 2.31 MeV line are the 2306.45 keV line (reaction cross section $\sigma_\gamma = 2.6$ mbarn) and the 2308.97 keV line ($\sigma_\gamma = 0.9$ mbarn), for which the photoelectric absorption probability in TiB_2 is less than 3×10^{-4} %. By comparison, the $^{10}B(n, \alpha)^{7}Li$ reaction is by far the dominant reaction in the

TiB_2 crystal, with a cross section larger than 4000 barns for thermal neutrons and an (n, α) absorption efficiency practically 100%.

The theoretical energy resolution calculated with $\Delta E_{FWHMy} = 2.355(4k_BT^2C_{abs})^{1/2}$ is 1.57 keV FWHM. By comparison, the simple calorimeter energy resolution equation (3.15) estimates 0.33 keV FWHM. The composite calorimeter model provides a value of 0.71 keV FWHM. However, these values are obtained assuming there is no additional noise interference in the signal. It was shown in Section 5.1 that the experimental noise current is a factor of 2 larger than the expected theoretical noise current. Because the energy resolution is proportional with the integral of the noise current $\Delta E \sim \int i_{total}(\omega)$, the energy resolution is estimated to be a factor of about 2 larger than the estimates made based on theoretical models. Based on this, the expected energy resolution is between 0.6 keV to 3.1 keV FWHM.

These results demonstrate that high energy resolution neutron spectroscopy is possible with cryogenic calorimeters. The next section discusses how the difference in the line widths can be used to extract the lifetime of the first excited energy level of the ^{7}Li nucleus produced in the $^{10}B(n,\alpha)^7Li^*$ reaction.

5.3 Determining the lifetime of the first excited state in ^{7}Li

The purpose of this section is to calculate the lifetime τ of the first excited state in ^{7}Li at 478 keV from the experimentally observed broadening of the spectra in Fig. 5.4 with the Inverse Doppler Shift Attenuation method (IDSA). Originally, the direct DSA method was used for extracting the lifetime τ of an excited energy level from the Doppler broadening of gamma spectra when the stopping power of the recoil nucleus is known. In

this Chapter we apply this theory to the ^{7}Li recoil nucleus for determining τ from the experimental broadening of the neutron spectral lines in Fig. 5.4.

In the case of short-lived nuclear states with lifetimes in the picosecond range, τ is typically measured from the broadening of the spectral features associated with these states, obtained either by photoelectron or by gamma-ray spectroscopy. One particular case is the on-flight emission of a gamma-ray from an excited nucleus traveling through matter, which produces Doppler broadening of the gamma-ray line and the broadening of the recoil nucleus energy. In this case, two independent processes occur simultaneously: a) the nucleus slows down as a result of the interaction with the target material, characterized by an overall slow-down parameter D, and b) the excited state decays with a lifetime τ. As a result, τ and D cannot be obtained simultaneously from the same measurement. Instead, when determining τ, the value of D has to be obtained independently from theoretical models or other experimental measurements. Methods for determining D are based on theoretical calculations of the stopping power and ranges of ions in matter, such as the Lindhardt-Scharff-Schiott (LSS) theory [Lin 63] and the Universal Stopping Power Function [Zie 75]. Alternatively, the work of Neuwirth et al. studies the stopping power and ranges of ^{7}Li ions in borides, considering the lifetime of the 478 keV state as known from other experimental measurements [Hau 74], [Neu 75]. An upper limit of 200 fs for the lifetime of the 478 keV level in ^{7}Li was first determined by photoelectron spectroscopy [Ell 48]. Subsequent precision measurements with Ge spectrometers since early 1960s have determined a lifetime value τ = 103 fs, corresponding to a half-life $t_{1/2} = \tau \times \ln 2 = 73$ fs [Ajz 88]. The technique was also used to determine the electronic stopping power of ^{7}Li ions resulting from ^{10}B(n, α)^{7}Li reaction

in various boron compounds by applying the IDSA method. Other applications of the IDSA method were in non-destructive quantitative and state analysis of trace amounts of boron in the presence of Na and Ni in neutron activation measurements on environmental samples [Sak 96], [Mag 98] and in determining the range of $^{7}Li^{*}$ nuclei in matter in Boron Neutron-Capture Therapy based also on the $^{10}B(n, \alpha)^{7}Li$ reaction [Cod 99].

To a larger extent, the information carried by the Doppler-broadened gamma-ray lines has been used to study of energy levels of exotic nuclei [Fyn 03]. An example is the Gamma-Ray Induced Doppler broadening (GRID) technique that uses the grazing angle in crystal spectrometers with an energy resolution <10 eV to measure the lifetimes of excited states in ^{49}Ti, ^{54}Cr, ^{57}Fe and ^{36}Cl by direct Doppler Shift Attenuation [Bör 93].

5.3.1 Recoil broadening

^{7}Li designates the nucleus in the ground state and $^{7}Li^{*}$ designates the excited nucleus at the 478 keV energy level. By decay, we refer to the de-excitation of the 478 keV energy level to the ground state with the emission of the gamma-ray.

The exothermic $^{10}B(n, \alpha)^{7}Li$ reaction proceeds with 94% probability in the first excited state of $^{7}Li^{*}$ with a reaction energy Q = 2.31 MeV, where $^{7}Li^{*}$ is always emitted with an initial kinetic energy E_0 = 842 keV ($\beta = v/c = 0.016$). The ^{4}He nucleus is always emitted in its ground state with a kinetic energy of 1.46 MeV. With this initial energy, the travel time of an energetic ion through the host crystalline lattice is on the order of hundreds to thousands of fs [Kno 99], [Zie 77]. The 478 keV gamma-ray is emitted on-flight from the first excited level of $^{7}Li^{*}$ which is left in the ^{7}Li ground state afterwards. A large fraction of the 478 keV gamma-rays escape out of the target, their energies can be measured by gamma-ray spectroscopy external to the target system (DSA method). Depending on the

speed v of $^{7}Li^{*}$, at the decay moment, the gamma-ray experiences a Doppler shift in energy ΔE_{γ}, while the recoil nucleus experiences the corresponding kinetic energy variation ΔE_r. Here, c is the speed of light. Both the excited and the de-excited ^{7}Li nuclei continuously transfer energy to the crystalline lattice during the slowdown until they finally stop as neutral atoms. The kinetic energy of the $^{10}B(n, \alpha)^{7}Li$ reaction products is completely deposited in the crystal in a maximum range on the order of 3-4 μm (see Table 2.3). When using a borated material, the total energy deposited in the crystal is $E_{total} = 0.842$ MeV + 1.46 MeV + $\Delta E_r = Q_r + \Delta E_r$. Thus, the broadening of the 2.31 MeV energy deposition line is given by ΔE_r.

The lifetime τ can be determined by comparing the analytical energy distribution for the ^{7}Li recoil nuclei with the experimental measurement of ΔE_r in the crystalline sample. In this experiment, we have adapted the IDSA method to measure the ^{7}Li recoil energy instead of the Doppler broadening of the 478 keV gamma-ray. The recoil energy is derived from the momentum vector diagram in the laboratory system |L| (Fig. 5.5).

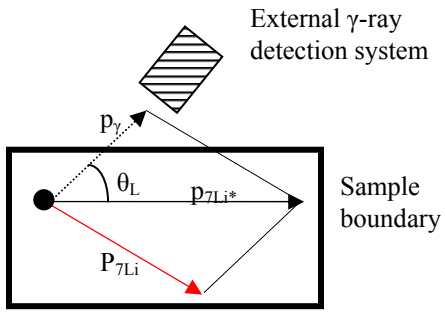

Figure. 5.5. Momentum vector diagram in the laboratory reference frame for energy distribution calculation. The recoil nucleus deposits its kinetic energy within the sample, whereas the gamma-ray escapes out of the sample.

For thermal neutrons, the ^{7}Li ion is initially emitted isotropically, and the direction of the gamma-ray emission or the direction of the ^{7}Li recoil nucleus, are not known.

In terms of kinetic energy, the recoil energy E_r is determined from the conservation of momentum and energy, according to:

$$E_r = E + \frac{E_\gamma^2}{2E_{Li}} - E_\gamma \sqrt{\frac{2E}{E_{Li}}} \cos\theta_L \tag{5.2}$$

where $E_{7Li} = m_{7Li}v^2/2$ is the kinetic energy of the $^7Li^*$ nucleus with a speed v before the recoil, $E_\gamma = 478$ keV is the energy of the gamma-ray, $E_{Li} = 6.55\times10^6$ keV is the rest mass of the ^7Li nucleus, and θ_L is the angle between the initial direction of the $^7Li^*$ momentum and the direction of γ-ray emission in the laboratory system. The energy of the gamma-ray is Doppler-broadened with $\Delta E_\gamma = E_\gamma(v/c)\cos\theta_L$. In our case, we are not measuring the gamma-rays escaping from the sample, but the total energy deposited by the ^7Li nuclei.

In a first approximation, the variation of the energy deposition can be considered in terms of extreme maximum values of the recoil energy E_r, which is obtained for $\cos\theta_L = -1$ and to $\cos\theta_L = +1$:

$$\Delta E_{max}(E) = E_{r,\ \cos\theta=-1} - E_{r,\ \cos\theta=+1} = 2E_\gamma \sqrt{\frac{2E}{E_{Li}}} \tag{5.3}$$

The maximum energy variation of the recoil nucleus broadens the 2.31 MeV line by the decay of the $^7Li^*$ nucleus in the TiB_2 lattice. The maximum broadening $\Delta E^0_{max} = 15.32$ keV is obtained when the decay occurs at the initial kinetic energy of the $^7Li^*$ nucleus $E = E_0 = 842$ keV. Measuring energy fluctuations on the order of ΔE^0_{max} or smaller requires an instrumental energy resolution of comparable magnitude. For an instrumental energy resolution of 5.5 keV FWHM (Fig. 5.4), this type of measurement is feasible. The minimum variation of the recoil energy occurs when the ^7Li nucleus has already been stopped in the crystalline lattice and its kinetic energy equals the thermal energy of the

lattice E = $E_{thermal}$. The recoil broadening in this case is $E_r = E_\gamma^2/(2E_{7Li}) = 17.4$ eV, which is not possible to measure with an energy resolution on the order of a few keV.

When the $^{10}B(n, \alpha)^7Li$ reaction takes place in the target material (crystalline, liquid or gaseous), the ^7Li recoil nucleus deposits its energy either by ionization and excitation of the electrons in the surrounding atoms, for kinetic energies > 50 keV, or by nuclear scattering due to Rutherford-type interactions. The dominant energy loss for $^7Li^*$ is due to electronic interactions [Neu 75] and it creates a time-dependent speed v(t) and kinetic energy E(t) respectively, described by:

$$v(t) = v_0 e^{-t/D} \quad \text{and} \quad E(t) = E_0 e^{-2t/D}. \tag{5.4}$$

Based on equations (5.3) and (5.4), the limits of the time-dependent recoil energy E_r are:

$$E_r(t) = E_0 e^{-2t/D} + \frac{E_\gamma^2}{2E_{Li}} \pm E_\gamma \sqrt{\frac{2E_0}{E_{Li}}} e^{-t/D}, \tag{5.5}$$

and the maximum available energy interval $\Delta E_{max}(t) = E_{r,\ \cos\theta=-1} - E_{r,\ \cos\theta=+1}$ for the recoil energy, based on equations (5.4) and (5.5) results in:

$$\Delta E_{max}(t) = 2E_\gamma \sqrt{\frac{2E_0}{E_{Li}}} e^{-t/D} = \Delta E^0_{max} e^{-t/D}, \tag{5.6}$$

The maximum energy variation given by equation (5.6) is presented in Fig. 5.6. The variation in the recoil energy becomes smaller as the gamma-ray decay occurs later in time.

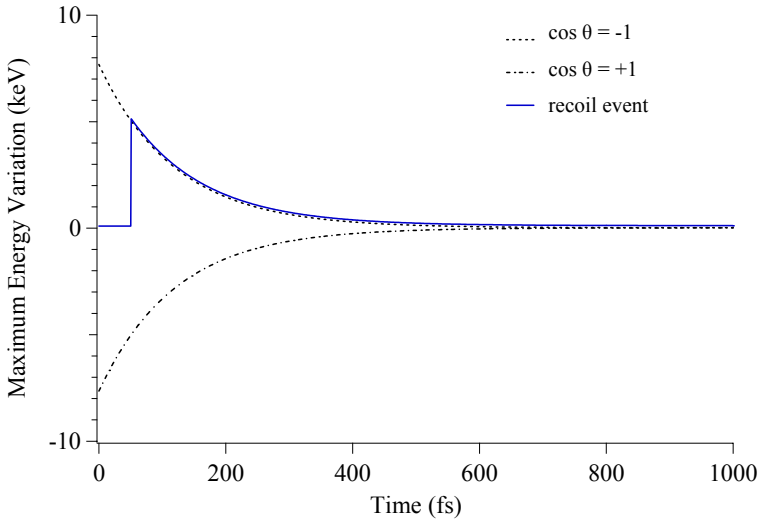

Figure 5.6. Maximum energy variation $\Delta E_{max}(t)$ as a function of time for a single event.

5.3.2 Analytical energy distribution

We assume an initial total number N_0 of $^7Li^*$ nuclei that are slowing down in TiB_2 and decaying with a lifetime τ while traveling through the crystal.

The time interval from the emission of the $^7Li^*$ nucleus ($t_0 = 0$) to the stopping time t_s is discretized in a number $\eta = (t_s - t_0)/\Delta t$ intervals, where $\Delta t = t_i - t_{i-1}$ ($i = 1$ to η) is the elementary time interval (Fig. 5.7). Since $N(t) = N_0 \exp(-t/\tau)$ with the lifetime τ, at the moment t_i, the number of nuclei that decay in the time interval $\Delta t = t_i - t_{i-1}$ is $\Delta N_i = -(N_0/\tau)e^{-t/\tau}\Delta t$, with $\Sigma_i(\Delta N_i) = N_0$. The decay probability in any time interval Δt is constant and the corresponding variations in the recoil energy can be represented by a rectangle with the area proportional to the maximum energy broadening available at the moment t_i (Fig. 5.7).

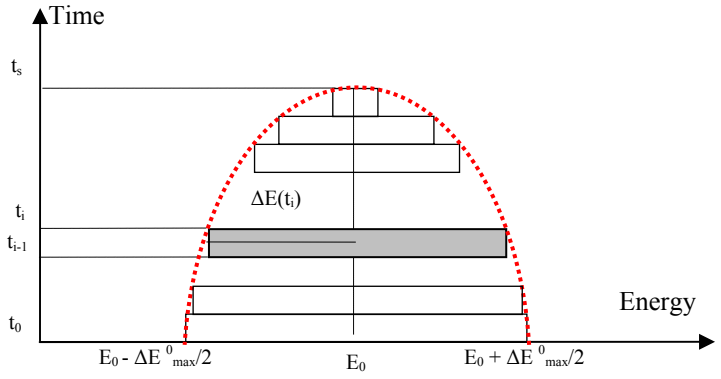

Figure 5.7. Maximum energy variation $\Delta E_{max}(t)$ as a function of time for overall energy distribution.

Based on equation (5.6), the maximum energy variation around E_0 is:

$$| \Delta E_{max}(t_i) | = \frac{1}{2} \Delta E^0_{max} e^{-t_i/D} \tag{5.7}$$

Thus, the elementary energy distribution around $E_0 = 842$ keV in any time interval $\Delta t = t_i - t_{i-1}$ is:

$$f_i(t_i)\Delta t = \frac{\Delta N_i}{|\Delta E_{max}(t_i)|} \tag{5.8}$$

The total energy distribution is obtained by summing all individual energy distributions from the emission of the $^7Li^*$ nuclei at $t_0 = 0$ to the moment of the gamma-ray emission at $t = t_E$:

$$f(E) = \sum_{i=1}^{\eta} f_i(t_i)\Delta t \tag{5.9}$$

After $t = t_E$, no other decay of the same ^7Li nuclide is possible, thus it will not contribute to the energy broadening. When $\Delta t \rightarrow 0$, the summation can be replaced by the integral:

$$f(E) = -\frac{2N_0}{\tau \Delta E^0_{max}} \int_{t=0}^{t=t_E} \exp\left(-\frac{\tau - D}{\tau D}\right) dt \tag{5.10}$$

At the moment t_E of the gamma-ray emission, the maximum available energy variation is $2|\Delta E_{\max}(t_E)| = \Delta E^0_{\max} e^{-t_E/D}$ and the moment of emission t_E can be calculated as:

$$t_E = -D \ln\left(\frac{2|\Delta E_{\max}(t_E)|}{\Delta E^0_{\max}}\right) \tag{5.11}$$

Considering $D = s\tau$, where *s* is a non-dimensional fit parameter (shape factor), the energy distribution given by equation (5.10) becomes:

$$f(E) = \frac{2N_0}{\Delta E^0_{\max}} \frac{s}{s-1}\left[1 - \left(\frac{2|\Delta E_{\max}|}{\Delta E^0_{\max}}\right)^{s-1}\right] \tag{5.12}$$

with ΔE_{max} given by equation (5.6) and ΔE^0_{max} = 15.32 keV. Equation (5.12) represents the line shape contribution to the broadening from the energy distribution of the recoil nuclei. The total analytical shape of the broadened line, such as the one in Fig. 5.4, is obtained by convolving equation (5.12) with the instrumental energy resolution. The expression in equation (5.12) describing the energy distribution of the recoil nuclei is similar to the distribution obtained for Doppler-broadened gamma-rays in [Cat 67], [Kub 00]. The FWHM broadening of equation (5.12) is given by:

$$\Delta E_{FWHM} = \left(\frac{1}{2}\right)^{\frac{1}{s-1}} \Delta E^0_{\max} \tag{5.13}$$

The fit parameter *s* is calculated from equation (5.13), by taking into account the experimental broadening of the line ΔE_{broad} = 8.9 keV. The lifetime of the excited level is calculated then as:

$$\tau = \frac{D}{1 - \dfrac{1}{\log_2\left(\dfrac{\Delta E_{broad}}{\Delta E^0_{\max}}\right)}} \qquad \text{where} \qquad s = 1 - \frac{1}{\log_2\left(\dfrac{\Delta E_{broad}}{\Delta E^0_{\max}}\right)} \tag{5.14}$$

With ΔE_{broad} = 8.90 keV and ΔE^{0}_{max} = 15.32 keV, the fit parameter is s = 2.28. The convolution of equation (5.12) with a Gaussian instrumental energy resolution with 5.5 keV FWHM is in good agreement with the experimental line shape.

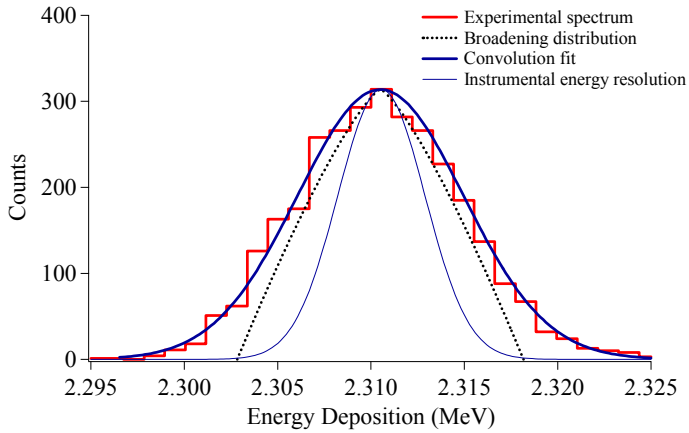

Figure 5.8. Experimental data fit of the 2.31 MeV energy deposition line with the broadening energy distribution convolved with the instrumental energy resolution.

With these results, Fig. 5.8 is now understood as the Gaussian instrumental energy resolution enlarged to 10.5 keV FWHM by the non-Gaussian broadening of the energy distribution of the recoil nuclei. A value of $s = D/\tau > 1$ is consistent with literature values of the time scales for stopping and decay for the ^{7}Li ion, i.e., D is on the order of 10^{-13} s while τ is on the order of 10^{-14} s. In order to determine τ from the experimental results, the value of the slow-down parameter D for the ^{7}Li ions in TiB_2 is calculated with equation (5.4) and the chain rule $v(dE/dx) = (dE/dt)$, where dE/dx is the stopping power of the ion in the absorber material:

$$D = \frac{2E_0}{v\,(dE/dx)} \tag{5.15}$$

The stopping power of ions in solids consists of two terms:

- the energy transferred by the ion to the target electrons (called electronic stopping or inelastic energy loss) that is dominant when the ion velocity is much larger than the Bohr velocity $v_B = e^2/(4\pi\varepsilon_0\hbar) = 0.007c$ of the orbital electrons;
- the energy transferred by the ion to the target nuclei (called nuclear stopping or elastic energy loss) which occurs when v is comparable with v_B [Zie 77]. The nuclear stopping component is usually considered separately because the heavy recoiling target nucleus can be assumed to be unconnected to its lattice during the passage of the ion, and the elastic recoil energy which is transferred to it can be treated as being due to the elastic scattering of two heavy screened particles.

The Bethe-Bloch stopping power equation [Bet 30] for ions traveling with velocity v in a material with the ionization potential I, describes the transfer of energy to the target electrons given by the expression:

$$-\frac{dE}{dx} = \frac{e^4 z^2 nZ}{\varepsilon_0 m_e v^2}\left[\ln\frac{2m_e v^2}{I\left(1-v^2/c^2\right)} - \frac{v^2}{c^2}\right] \tag{5.16}$$

where e is the electron charge, z the charge of the ion, n the number density of target atoms, Z the charge of the target atoms, ε_0 the vacuum permitivity, m_e the electron mass, c the speed of light. The derivation of this equation assumes that the ion velocity v is much larger than the Bohr velocity $v_B = e^2/(4\pi\varepsilon_0\hbar) = 0.007c$ of the orbital electrons and the target is characterized by a mean ionization potential created by immobile electrons which do not change their position relative to the impact parameter. Because the initial velocity of the ^{7}Li ion traveling in TiB_2 is $v_0 = 0.016c$, a factor of 2.1 larger than v_B, the Bethe-Bloch equation does not apply correctly to the calculation of the stopping power of ^{7}Li ions with the initial energy $E_0 = 842$ keV. For example, with an ionization potential I

= 165.5 eV of the TiB_2 target [Ahl 80], the Bethe-Bloch stopping power results in dE/dx ~ 15 eV/cm. With this value, the slowdown parameter D is on the order of 2×10^{-4} s, which results in a lifetime $\tau \approx 10^{-4}$ s, inconsistent with the reference value of 103 fs.

In a different approach, the Lindhardt-Scharff-Schiott (LSS) theory models the transfer of energy to the target nuclei considering the collision kinematics calculated from the atom-atom interatomic potentials [Lin 63]. This model considers all atoms at zero temperature and it can be applied to the relatively slow (by comparison to v_B) ^7Li ions with energies below ~ 1 MeV traveling in TiB_2 [Zie 77]. The slow-down parameter D is calculated directly according to:

$$D = \sum_{1}^{2} n_i \delta_i \tag{5.17}$$

where n_i is the number density for each element in the TiB_2 compound. δ_i is the elemental slow-down parameter calculated by assuming the interaction of the ^7Li ion with each element of the TiB_2 compound in a pure form, namely B and Ti only, as given by:

$$\delta_i = \frac{k_i W_i}{\sqrt{2 C_i M_{^7Li}}} \quad (i=1,2) \qquad W_i = 4\pi \frac{a^2 M_{^7Li} M_i}{(M_{^7Li} + M_i)^2}$$

$$C_i = \frac{a M_i}{Z_{^7Li} Z_i q^2 (M_{^7Li} + M_i)} \qquad k_i = 0.00793 Z_{^7Li}^{1/6} \frac{(Z_{^7Li} Z_i)^{1/2} (A_{^7Li} + A_i)^{3/2}}{(Z_{^7Li}^{2/3} + Z_i^{2/3})^{3/4} A_{^7Li}^{3/2} A_i^{1/2}} \tag{5.18}$$

with Z_i, M_i and A_i being the element number, the atomic mass and atomic number of the *i*-th element. The interatomic distance a is estimated based on the Bohr radius of the hydrogen atom $a_0 = 0.529 \times 10^{-10}$ m:

$$a = 0.8853 a_0 (Z_{^7Li}^{2/3} + Z_i^{2/3})^{-1/2} \tag{5.19}$$

The value obtained from the LSS model for ^{7}Li ions in TiB_2 is D = 252.4 ± 9.6 fs. With this value, we obtain a lifetime of 110 ± 8 fs, which is about 7% larger than the currently evaluated data τ_{ref} = 103 fs found in literature [Fir 96].

In a third approach to calculating the lifetime through the slowdown parameter D in TiB_2, data has been extracted from the measurements of the stopping power by Neuwirth [Neu 75]. This experiment has employed the Inverted Doppler Shift Attenuation method for the determination of the stopping power of excited ^{7}Li nuclei recoiling in matter, assuming that the lifetime of the first excited state is of 115 fs, which was the reference value at the time of the measurement (year 1974). This measurement concluded that stopping power of the Li ions is predominantly due to nuclear stopping interaction below 80 keV and to electronic stopping interactions above 80 keV. A value $(dE/dx)_{exp}$ = 6237 ± 52 MeV/cm has been obtained at the Bohr velocity v_B for Li ions traveling in TiB_2. According to equation (5.4) and to the chain rule $v(dE/dx) = (dE/dt)$, the stopping power at the velocity v = 0.016c of the ^{7}Li ion is $dE/dx = v/v_B(dE/dx)_{exp}$. By this formula, the slowdown parameter is D = 559 ± 61 fs from which the lifetime is 242 ± 26 fs, within a factor of 2 of the current reference lifetime value of 103 fs (Table 5.2).

Table 5.2. Comparison of lifetime τ and half-life $t_{1/2}$ from experimental data and stopping power calculations (reference value $\tau_{ref} = 1.03\times10^{-13}$ s).

Theory or Experiment	**D (s)**	**τ (s)**	**$t_{1/2}$ (s)**	**τ/τ_{ref}**
Bethe-Bloch	2×10^{-4}	1×10^{-4}	6.9×10^{-5}	10^{7}
LSS	2.52×10^{-13}	1.10×10^{-13}	7.6×10^{-14}	1.05
Neuwirth et al.	5.59×10^{-13}	2.42×10^{-13}	1.6×10^{-13}	2.34

Chapter 6. Experimental results with LiF devices

This Chapter presents the results obtained for neutron spectrometers with natural and enriched LiF absorbers, which are used for fast-neutron spectroscopy. We have experimented with two diferent LiF absorbers, mounted as in Fig. 4.4 in the setup in Fig. 6.1, with the temperature sensor (TES) glued on the top of the absorber and reffered to as LiF-1, LiF-2A and LiF-2B. Device LiF-1 uses a natural LiF absorber, while devices LiF-2A and LiF-2B use the same enriched ^{6}LiF absorber and the same TES sensor but are treated separately because they have different thermal parameters (Table 6.1).

Table 6.1. Physical parameters and mounting of the LiF crystal absorbers

Device name	Volume (cm^3)	^{6}Li enrichment (%)	Description
LiF-1	0.8	7.2 (natural)	TES glued on top, Au wire cooling path
LiF-2A	0.2	92	TES glued on top, pressure contact cooling path (low mechanical tension)
LiF-2B	0.2	92	TES glued on top, pressure contact cooling path (high mechanical tension)

MCNP simulations have been used to understand the response of the absorbers to an external neutron flux in two different geometries derived from the experimental setup presented in Fig. 4.13. As described in Chapter 2, when using a LiF absorber for fast-neutron spectroscopy, the external neutron flux must be reduced as much as possible in order to increase the efficiency in the energy range above 50 keV. This approach is the opposite of the type of shielding used for neutron thermalization used to characterize the energy resolution of the TiB_2 detector. When simulating with MCNP the heavy neutron shielding in Fig. 4.13, about 55% of the detected events are due to neutrons with energy below 50 keV which results in a prominent thermal peak that reduces the efficiency in the fast-neutron region. However, because a complete reduction of the thermal neutron peak

is not possible, the goal is to have only about 10% of the detected events coming from neutrons below 50 keV. An MCNP simulation of the actual experimental setup which is presented schematically in Fig. 6.1, shows that the number of neutrons detected in the energy range below 50 keV is reduced to about 18% when removing the neutron thermalizing materials around the detector (HDPE and radiation shielding). The ^{252}Cf source is placed inside the 'sample', which consists of lead or aluminum blocks with thickness of 5 cm to 10 cm. The squares inside the cryostat indicate the position of the LiF absorbers with only one crystal used at the time.

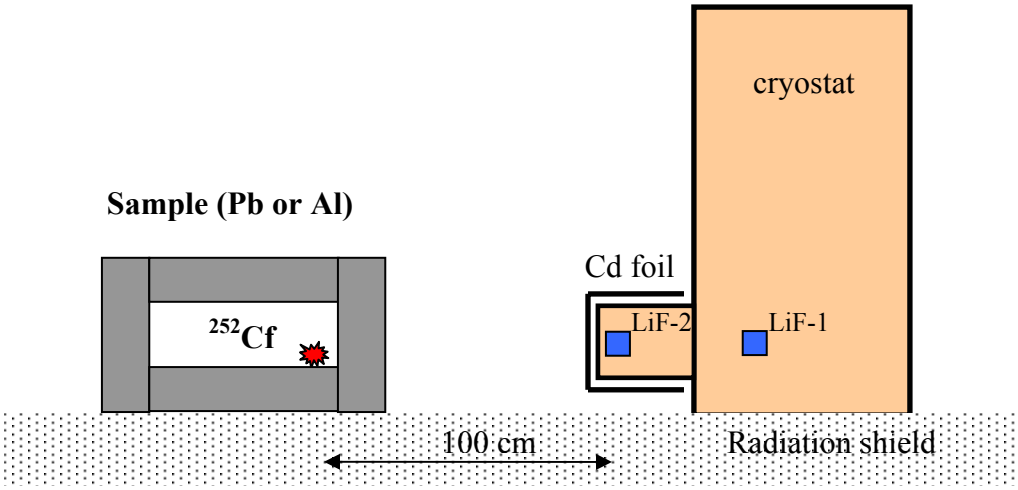

Figure 6.1. Measurement geometry with LiF absorbers.

The Cd foil presented in Fig. 6.1 has a thickness of 2 mm and it was used in order to absorb external neutrons with energies below the cut-off edge at 0.3 eV.

6.1 Results from the natural LiF-1 neutron detector

The LiF-1 device uses a 1 cm × 2 cm × 0.4 cm LiF absorber with natural isotopic composition and is installed inside the cryostat (Fig. 6.1) rather than on the cold finger. The device is tested with a ^{252}Cf source with an activity of about 0.2 μCi (Fig. 6.2). The

source is positioned at 20 cm from the absorber, resulting in a solid angle of 7.9×10^{-5} sr, and an expected count rate of 0.5 Hz. Since the absorber is more efficient to thermal neutrons, the observed count rate for events above the thermal peak is ~ 0.2 Hz. No Cd foil is used in this experiment in order to detect the thermal component of the neutron spectrum. The parameters of device LiF-1 are summarized in Table 6.2.

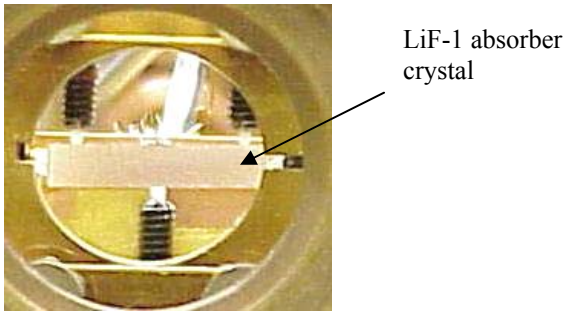

Figure 6.2. View of the LiF-1 device through the cryostat porthole before closing. The Teflon spring plunger holders are visible in the top and at the bottom of the crystal.

Table 6.2 Operation parameters of the natural LiF-1 device

Parameter	**Value**
LiF-1 absorber mass m	2.1 g
Bath temperature T_{bath}	110 mK
Operating temperature T_0	143 mK
TES sensitivity α	70
Absorber heat capacity C_{abs}	1.2 nJ/K
TES heat capacity C_{TES}	13 pJ/K
G_{TES} thermal conductance G_{TES}	2.6 nW/K
Bias resistance R_b	1.0 kΩ
Feedback resistance R_{FB}	1.0 kΩ
Shunt resistance R_s	5.0 mΩ
SQUID amplification A_{SQ}	43

Pulses obtained from the LiF-1 device have a single exponential decay time with a value of 13.5 ± 0.4 ms (Fig. 6.3). This value of the decay time allows for a count rate of pulses of ~ 5 Hz when using optimum filtering. The tail of the pulse is affected by the AC-coupling of the readout. The experimental rise time (0.77 ± 0.03 ms) is a factor of 2 larger than the theoretical rise time calculated for ballistic phonons traveling with a

velocity v ~ 4000 m/s inside the LiF absorber which reflects the finite phonon transmission probability across the absorber – Si chip interface.

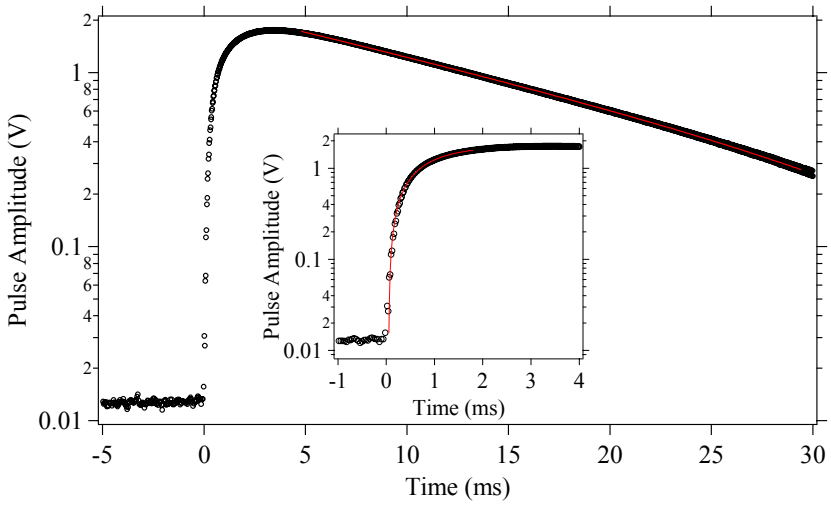

Figure 6.3. Average experimental pulse obtained with the LiF-1 device. The solid curve is a fit with single exponential function. The inset shows the rise time fit with a single exponential curve.

The observed white noise level at 1 kHz is 52 pA/Hz$^{1/2}$ (Fig. 6.4), somewhat higher than the expected noise level of 31 pA/Hz$^{1/2}$ according to the parameters in Table 6.2.

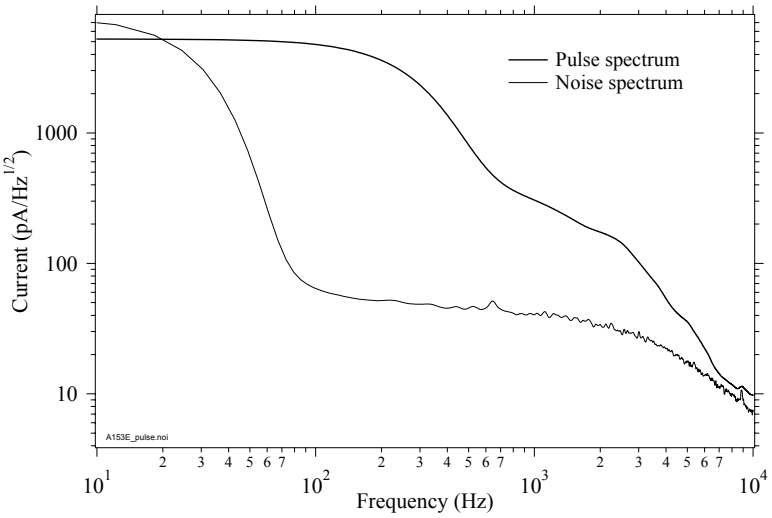

Figure 6.4 Noise and signal frequency spectra obtained with the LiF-1 device.

The LiF-1 device was first tested with the 0.2 μCi ^{252}Cf source without neutron thermalizing materials in the vicinity of the cryostat at a distance of 20 cm from the absorber, located at the outside wall of the cryostat. In this case, a count rate of 2-3 counts per minute was obtained, which is too low for a good detector characterization. To increase the thermal neutron flux, 15 cm of HDPE were subsequently added between the source and the cryostat. The expected distribution of the neutron absorption in the LiF-1 device was simulated with MCNP with the F6 tally normalized per energy bin. Figure 6.5 shows the maximum neutron flux below 1 eV, corresponding to quasithermal energies. Only a fraction of about 10^{-5} of the total neutron population is present in the 0.1 – 1 eV region. However, the incomplete neutron thermalization is revealed by the extension of the neutron distribution to ~ 40 keV, which broadens the high-energy portion of the observed thermal peak.

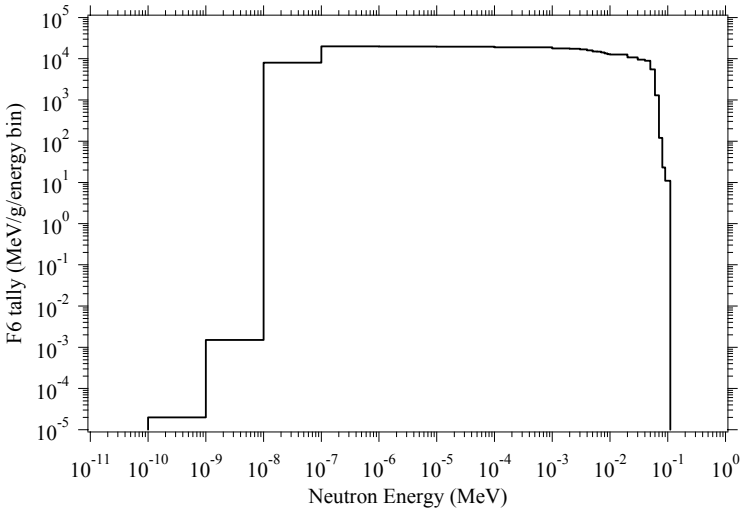

Figure 6.5. MCNP-simulated neutron energy distribution in the measurement geometry of the LiF-1 device

The expected theoretical count rate for thermal neutrons is about 0.5 Hz whereas for 240 keV neutrons it is a factor of 100 less. The natural isotopic composition of the LiF crystal and the low solid angle result in a count rate of about 0.2 Hz due to thermal neutrons

while the count rate for 240 KeV neutrons is a factor ~ 100 less. Because of the low detection efficiency above 50 keV (on the order of 10^{-4} %), the experimental spectrum only shows two major features (Fig. 6.6):

- the thermal peak at the Q-value of the (n, α) reaction centered at 4.782 MeV.
- low-energy events due to gamma rays, neutron recoil, and scattering that extends up to about 2.5 MeV.

The peak at 4.782 MeV is fit with a Gaussian function with a FWHM of 16 keV. The lower half of the peak extends about 42 keV below the Q-value and is predominately due to energy loss at the surface mechanism presented in Chapter 2. The upper half of the peak is asymmetric and it results from incomplete neutron thermalization, which extends about 55 keV above the Q-value. The MCNP simulation in Fig. 6.5 is convolved with the 16 keV energy resolution, which approximates the upper part of the peak.

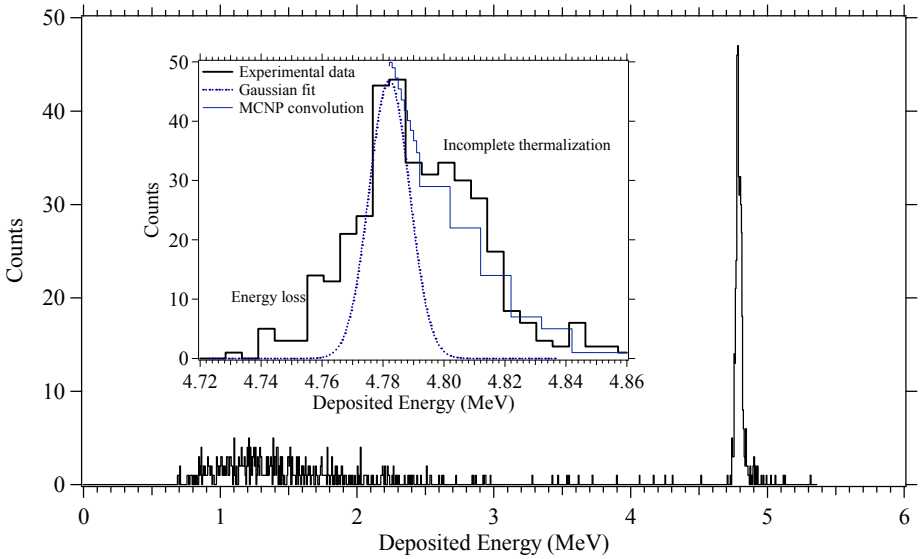

Figure 6.6. Experimental neutron spectrum obtained with the LiF-1 device. The inset shows the peak structure, with the dotted line representing the Gaussian fit of the data and the thin solid line being the MCNP simulation in Fig. 6.5 convolved with the energy resolution.

The thermal peak and the low energy gamma-rays and recoil events are about 2.5 MeV apart, which demonstrates good discrimination between neutron absorption and scattering events that can be obtained with this instrument.

The total FWHM of the thermal peak contains contributions from different independent effects which add in quadrature:

$$\Delta E^2_{FWHM} = \Delta E^2_{theoretical} + \Delta E^2_{el} + \Delta E^2_{SNSE} + \Delta E^2_{thermal} + \Delta E^2_{position} + ... \quad (6.1)$$

a. The theoretical energy resolution of the device $\Delta E_{theoretical}$ = 0.55 keV FWHM, as calculated according to equation (3.55) for the composite calorimeter with the parameters from Table 6.1. Its contribution is negligible.

b. The electronic noise of the readout ΔE_{el} = 1.2 keV FWHM can be obtained from the convolution of an average pulse with the measured baseline noise. In this setup it is negligible too.

c. The energy loss at the surface, ΔE_{SNSE}. The FWHM value corresponding to the lower half of the peak is obtained from the MCNP simulation (Fig 6.5) and the values for energy spread presented in Table 2.4. The lower half of the peak is estimated at FWHM = 96 ± 13 keV, which corresponds to an energy spread of 48 ± 6.5 keV below the Q-value. The FWHM is a factor of two larger than the experimentally observed broadening. This discrepancy likely originates in errors made with the MCNP simulation in the 10^{-10} – 10^{-9} MeV energy interval. Still, this suggests that energy loss due to scintillation may be a dominant contribution to the energy resolution of the device [Mar 93].

d. The broadening of the thermal peak due to incomplete neutron thermalization $\Delta E_{thermal}$ (Fig. 6.5). In this experiment, the non–thermal low energy component of the

input neutron spectrum from the ^{252}Cf source, which in total extends ~ 55 - 60 keV above the Q-value.

e. The energy loss in the absorber due to position dependence, $\Delta E_{position}$. Since neutron absorption in different parts of the LiF crystal produces signals with different rise times due to the finite phonon speed, this value can be estimated by plotting the pulse amplitude versus pulse rise time (Fig. 6.7). In a first approximation, the distance D from the interaction position to the temperature sensor is proportional to the rise time τ_r, i.e., $D \approx v_{phonon} \times \tau_r$. If the pulse amplitude decreases with τ_r, this is indicative of energy loss in the absorber. In this experiment, the slope is zero suggesting that for this device the broadening due to position dependence of the response is negligible.

f. Finally, some part of the energy of the reaction products may be trapped in long-lived metastable electronic impurity states. Also, some fraction of the reaction energy may cause lattice damage in the LiF crystal. The magnitude of these effects is difficult to estimate and may ultimately limit the attainable energy resolution.

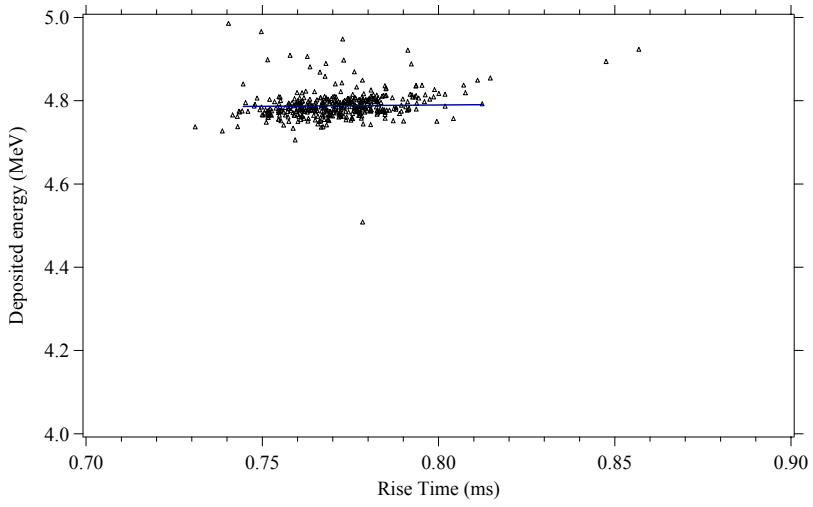

Figure 6.7. Deposited energy as a function of pulse rise time. The solid line is a linear fit to the data points, whose slope is zero within the uncertainty of the measurement.

6.2 Testing the LiF-2 device

The LiF-2 device is the generic name given to the enriched 0.7 cm × 0.7 cm × 0.4 cm LiF absorber with a volume of 0.2 cm^3. Two diferent sets of thermal coupling parameters have been used in experiments, which resulted in device LiF-2A and LiF-2B respectively (Table 6.3). The LiF-2 device is enriched to 92% in ^{6}Li, which by comparison with natural isotopic composition allows a factor of 12 increase in detection eficiency per unit volume of crystal. Because the LiF-2 device has 4 times smaller volume than LiF-1 but an enrichment which is 12 times larger, the effective gain in the eficiency is of a factor of 3. In addition, the LiF-2 device is installed at the end of the cold finger, which results in a solid angle of 1.5×10^{-5} sr for a source located at 50 cm, which is at least a factor of 5 larger than for the LiF-1 device. Thus, the overall gain in the eficiency for LiF-2 device is about a factor of 15. The expected count rate from a source activity of about 30 μCi is about 2.4 Hz. Note that the thermal conductances were different in LiF-2A and LiF-2B due to different mechanical pressure of the mounting scheme (Fig. 4.4.B).

Table 6.3 Operation parameters of the LiF-2 devices

Parameter	Value
LiF-2 absorber mass m	0.528 g
Bath temperature T_{bath}	108 mK
Operating temperature T_0	132 mK
TES sensitivity α	70
Absorber heat capacity C_{abs}	0.23 nJ/K
TES heat capacity C_{TES}	15 pJ/K
G_{TES} thermal conductance G_{TES}	10 – 20 nW/K
Bias resistance R_b	1.0 kΩ
Feedback resistance R_{FB}	1.0 kΩ
Shunt resistance R_s	5.0 mΩ
SQUID amplification A_{SQ}	43

Pulses from LiF-2A device exhibit a single exponential decay time of 17.3 ms. When increasing the mechanical tension of the Al screw to make LiF-2B device, the rise time decreases by a factor of 10, and the signal decay time decreases to 10.4 ms since both

G_{abs} and G_{TES} are increased (Table 6.4). This is the direct result of a better thermal coupling between the LiF absorber, the TES and the cold bath. The values for G_{abs} and G_{TES} are obtained according to equation (3.29). The thermal coupling is not only stronger in LiF-2B, but the signal is now best described by a double exponential function, with two components of 2.1 ms and 10.6 ms (Fig. 6.8).

Table 6.4. Thermal parameter comparison of the LiF-2A and LiF-2B devices.

Device	Decay time τ_d (ms)	Rise time τ_r (ms)	G_{abs} (nW/K)	G_{TES} (nW/K)	G_{abs} / G_{TES}
LiF-2A	22.3	1.120	32.4	10.4	3.1
LiF-2B	10.6 (long) 2.1 (short)	0.166	70.4	17.3	4.0

The presence of two exponential decay time in LiF-2B device suggests that ballistic phonons are initially detected, which cause the short decay time as they thermalize to energies of ~ k_BT. The 1/e rise time τ_r is set by phonon propagation inside the absorber with width W = 0.4 cm and the phonon transport across the absorber-sensor (TES) interface, $\tau_r \approx W/v_{ph} + (C_{Si+TES} + C_{LiF})/G_{abs}$. A ballistic phonon speed $v_{ballistic} = 4.9\times10^3$ m/s causes the energy to spread throughout the crystal within a few μs [Bro 95] [Pro 95]. The thermal coupling $1/G_{abs} = 1/G_K + 1/G_v$ between the absorber and the temperature sensor is due to the Kapitza boundary resistance $G_K = 1.6\times10^{-3}T^3A$ across the contact area A = 4 mm^2, plus the thermal conductivity of the GE varnish G_v = 105 μW/K [And 70]. The theoretical rise time in LiF-2B is $\tau_{r,theory}$ = 28 μs, a factor of 5 less than the smallest experimental value in Table 6.4. This is be due to a finite phonon transmission coefficient across the GE varnish used to glue the TES sensor onto the LiF absorber, as suggested by the reduction with a factor of 10 of τ_r when tightening the Al screw and by the shorter τ_r for events absorbed in the temperature sensor.

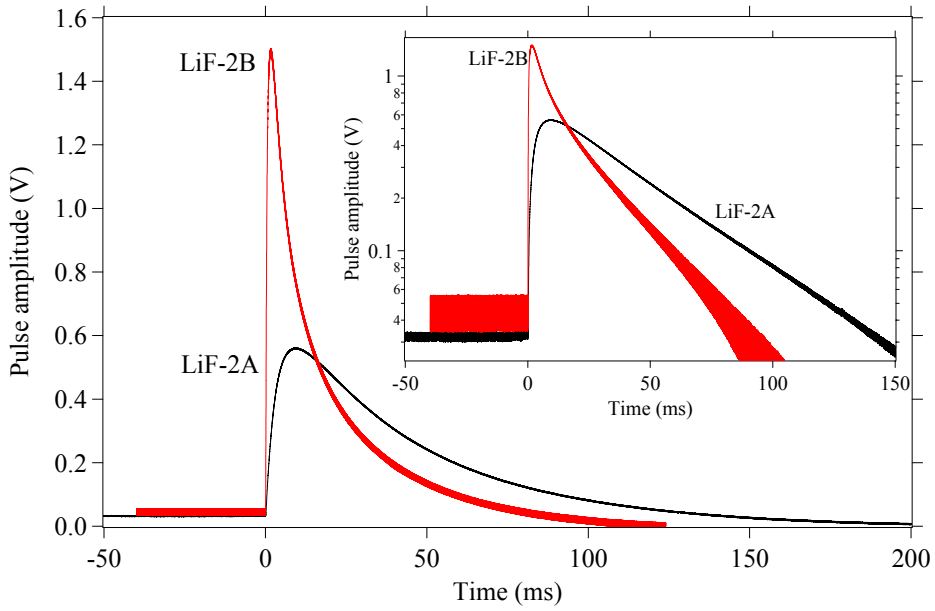

Figure 6.8. Comparison of the experimental pulses from devices LiF-2A (single exponential curve) and LiF-2B (double exponential curve). The inset shows pulses on a semi-logarithmic scale.

We can also determine G_{abs} by irradiating the detector with gamma-rays of known energy from a ^{57}Co source. The gamma rays interact with higher probability in the Si substrate of the temperature sensor (TES) and then decay to the absorber which acts as a cold bath, with a decay time $\tau_{d,gamma} \approx C_{TES}/G_{abs}$. For $\tau_{d,gamma} \approx 1$ ms obtained experimentally, we obtain $G_{abs} \approx 12.5$ nW/K and thus $\tau_d \approx 11$ ms, in agreement with the observations.

The detection of gamma-rays by the Si substrate of the temperature sensor during neutron measurements can not be completely avoided. Even with good external gamma-ray shielding, gamma-rays are still produced by the neutron interaction with the material in the cryostat, mostly Cu, Al, and stainless steel, and with ^{19}F inside the LiF absorber, which has rather large (n, gamma) and (n, inelastic) cross section by comparison with ^{6}Li and ^{7}Li (Fig. 2.6). At 100 keV, the photoelectric absorption coefficient of Si is $(\mu/\rho)_{Si} = 2.5\times10^{-2}$ cm^2/g, while for LiF is $(\mu/\rho)_{LiF} = 3.3\times10^{-3}$ cm^2/g, which makes the gamma-ray

absorption in the Si substrate with $C_{TES} << C_{abs}$ a factor of 6 more efficient than in LiF [XCO 06]. Gamma-rays with energies on the order of 100 keV produce a temperature rise in the Si chip on the order of 1 mK, comparable with the temperature rise of the neutron absorber upon an (n, α) reaction in LiF. The comparison in Fig. 6.9 shows a gamma-ray pulse absorbed in the Si substrate (τ_r = 0.092 ms, τ_d =1.3 ms) along with a neutron pulse (τ_r = 1.1 ms, τ_d = 22.3 ms) detected in the ^{6}LiF absorber. The differences in pulse shape allow easy discrimination between gamma events in Si and neutron events in LiF, thereby reducing the effects of gamma-rays on fast-neutron spectra.

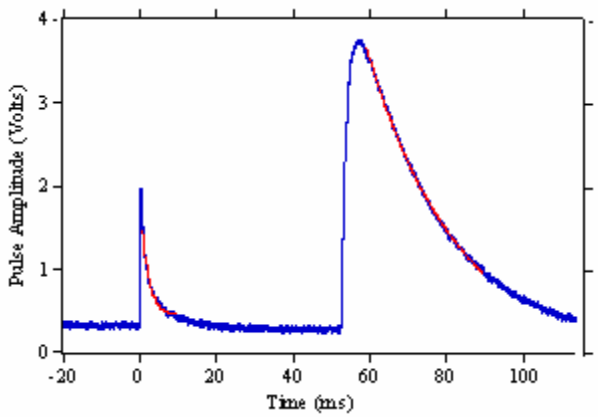

Figure 6.9. Comparison of gamma-ray pulse (left) and neutron pulse (right) in the LiF-2 device.

6.2.1 Experimental neutron spectra with LiF-2 device

Fast-neutron spectra obtained with 2 μCi ^{252}Cf source shielded with 1 cm of Pb were obtained with devices LiF-2A and LiF-2B for two different values of G_{TES} and G_{abs} (Fig. 4.4 and Table 6.4). The MCNP simulation of the detector response in this geometry shows a thermal peak with a FWHM 26 keV (Fig. 6.10).

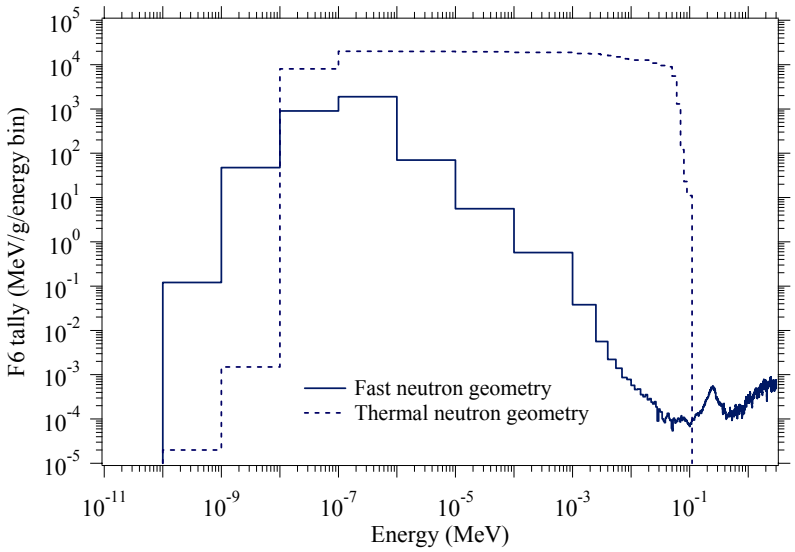

Figure 6.10. MCNP simulation of the energy distribution in LiF-2 device. For comparison, the energy distribution for LiF-1 is shown as a dotted line.

The incomplete neutron thermalization in the surrounding materials extends the thermal peak to about 45 keV. In the thermal energy range, the neutron distribution extends down to about 0.1 meV.

The thermal peak measured with LiF-2A and LiF-2B has a width ΔE_{FWHM} = 55 keV and ΔE_{FWHM} = 59 keV respectively, with an electronic noise of 2.5 keV (Fig. 6.11). In order to detect fast neutrons, no HDPE has been used in the vicinity of the source in this measurement, and the Cd foil was placed around the detector cold finger as shown in Fig. 6.1. For both LiF-2A and LiF-2B devices, the data is taken with low trigger level, and the energy events below 3 MeV represent 56% of the total events and 68% respectively. A gap of about 2 MeV is visible in the two spectra between the elastic scattering events and neutron capture events with energies above the Q-value of the (n,α) reaction at 4.782 MeV. Above this energy, the absorption peak above E_n = 240 keV ($E_{deposited}$ = 5.02 MeV) is visible. Energy deposition events up to $E_{deposited}$ ~ 9 MeV are detected for neutrons with

energies up to E_n ~ 4 MeV. Both spectra show the features expected from the *MCNP-Polimi* simulation (Fig. 2.25), which includes a low-energy tail, that extends to ~ 2.3 MeV. The experimental thermal neutron peak has a smaller amplitude than the simulated peak, because of the broadened spectrometer response.

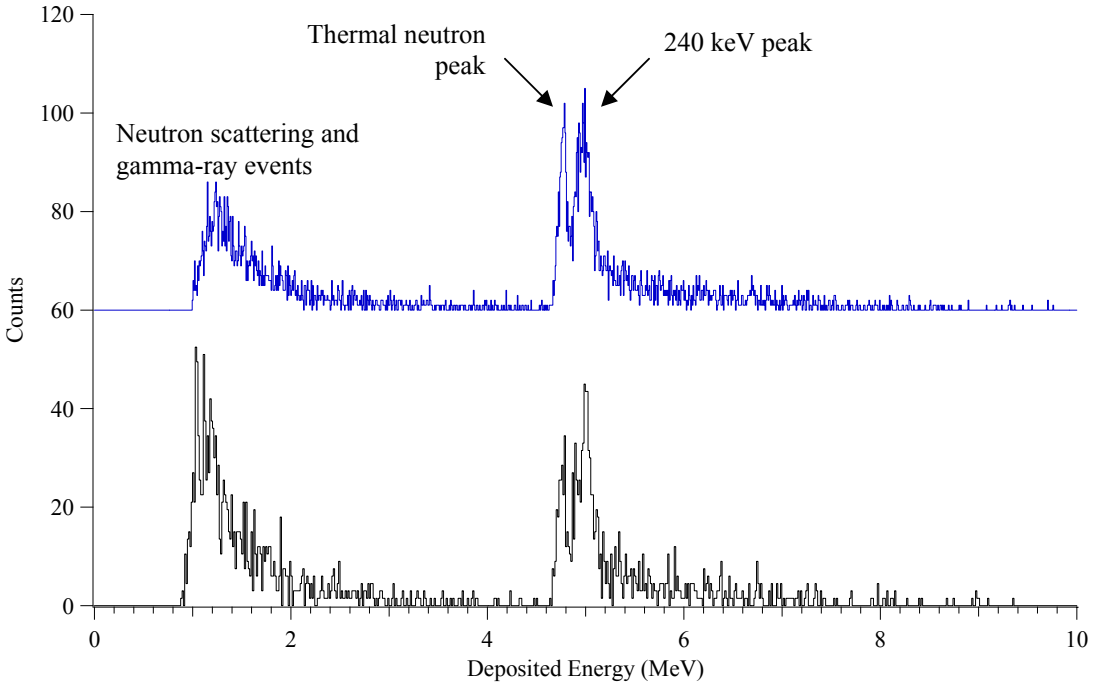

Figure 6.11. Response to ^{252}Cf for detectors with different thermal coupling between LiF and Si chip and TES. Top – LiF-2A device, Bottom – LiF-2B device. The top spectrum is shifted by 60 counts for clarity.

In the next set of experiments, detector LiF-2B was irradiated by a ^{252}Cf source with an activity of 350 μCi shielded with 5 cm of Pb in the the experimental setup is presented in Fig. 6.1. The experimental spectrum with energy bins 2.5 keV wide is compared to the MCNP simulation in Fig 6.12. The calibration of the spectrum includes the origin and the thermal peak. The thermal peak in the MNCP simulation has FWHM of 26 keV and its base extends to 42 keV above the Q-value. The width of the experimental thermal peak fit with a Gaussian is of 88 keV FWHM. The lower half of the peak extends 138 keV

below the Q-value due to energy loss, while the upper half of the peak extends 83 keV above the Q-value due to incomplete neutron thermalization. The errors associated with the 2.5 keV energy bins in the (n, α) peak corresponding to E_n ~ 240 keV are about 18%, which is not sufficient for visualizing spectral features.

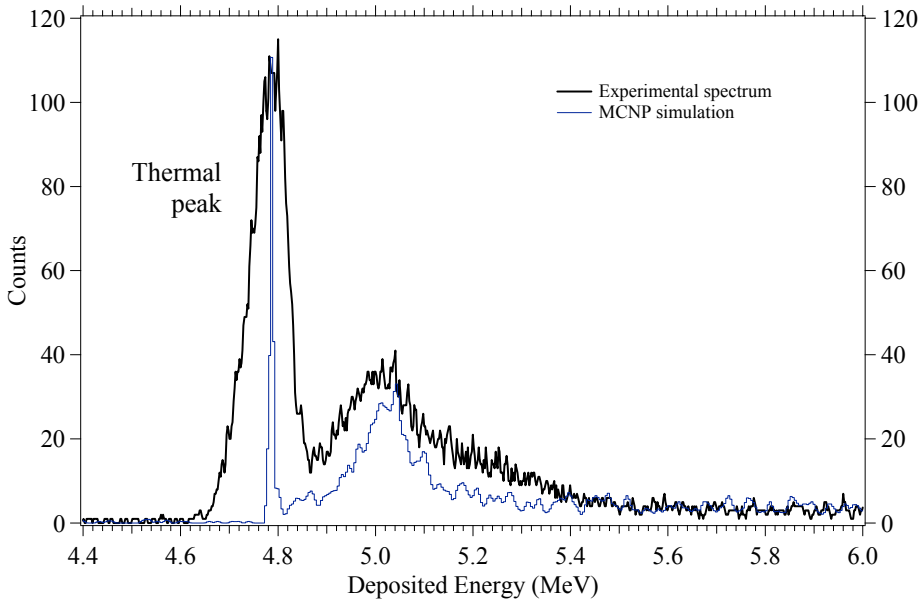

Figure 6.12. Experimental fast-neutron spectrum compared with MCNP simulation. The energy bin are 2.5 keV wide. For clarity, no error bars are included.

The counting statistics of the thermal peak improves to relative errors < 3% when the energy bins are increased from 2.5 keV as in Fig. 6.12 to 15 keV in Fig. 6.13. However, a few measured features seem to correspond to the structure expected from the MCNP simulation, such as the dip at 4.9 MeV which corresponds to neutron loss by inelastic interaction with the first excited state in ^{19}F at 109 keV, with a threshold at E_n = 116 keV. The dip at $E_{deposited}$ ~ 5.1 MeV in the resonant peak corresponds to En =

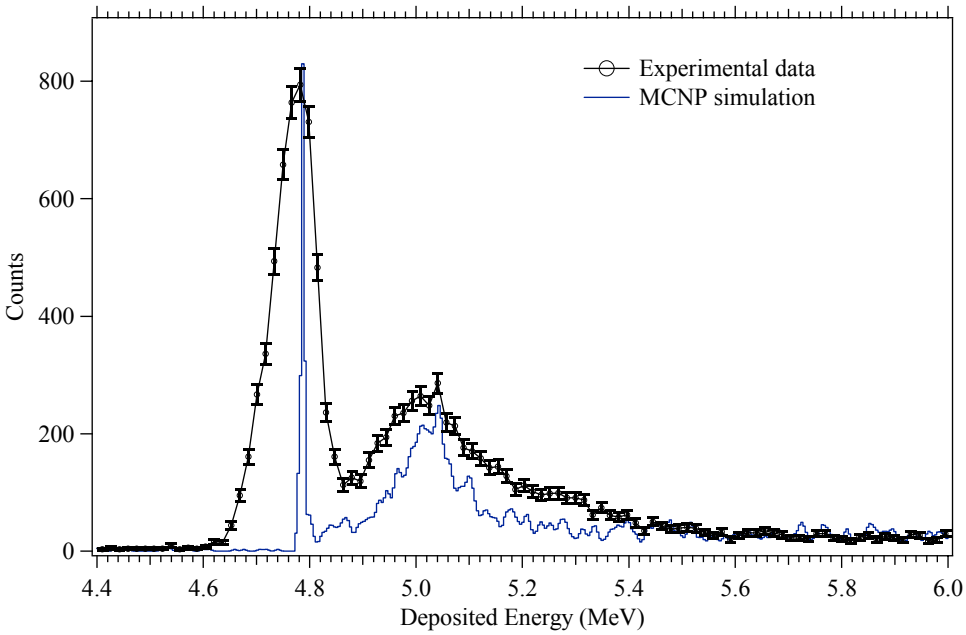

Figure 6.13. Experimental fast-neutron spectrum with error bars included. The energy bins are 15 keV wide with errors < 3% per energy bin..

6.2.2 Fast-neutron spectrum deconvolution

This section presents the reconstruction of the neutron spectrum incident upon the ^{6}LiF absorber from the spectrum in Fig. 6.13 and the 3-D response matrix from the MCNP simulation (Fig. 2.23). The neutron source term as seen by the ^{6}LiF absorber is calculated according to equation (2.13) by inverting the response matrix R(E). The projection on the deposited energy axis corresponds to the actual measurement. The inverse of the response matrix multiplied with the experimental spectrum reconstructs the incident neutron spectrum (Fig. 6.14).

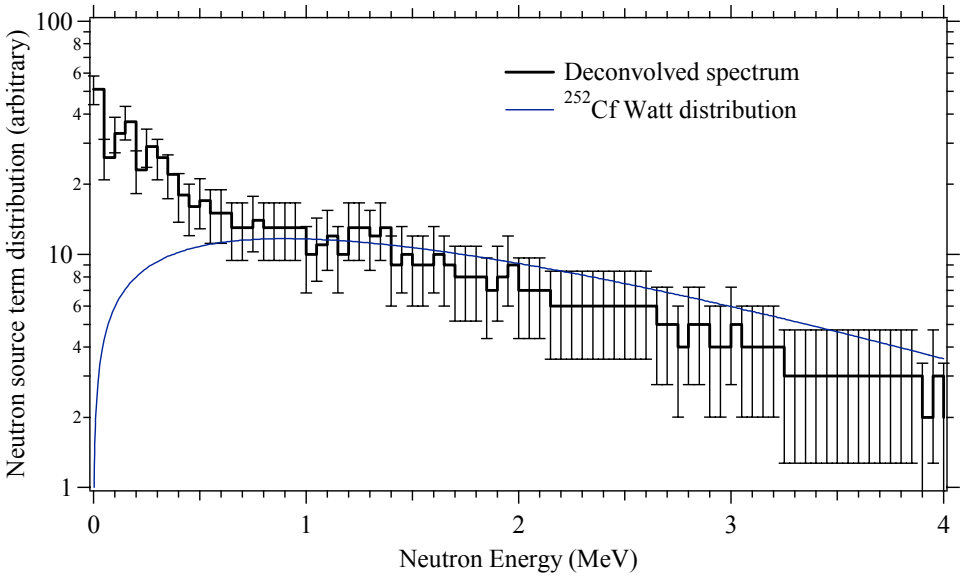

Figure 6.14. Reconstructed incident neutron spectrum as seen by the ^{6}LiF absorber. The solid line represents the initial Watt distribution of the ^{252}Cf source, given by equation (2.11).

The reconstructed spectrum has an overall energy distribution that partially resembles the original Watt distribution above 0.7 MeV. Below this energy, the spectrum is altered due to the presence of scattering materials around the absorber, with the effect of neutron thermalization more visible below 500 keV.

Chapter 7. Conclusions

The results in this dissertation demonstrate the possibility of fast-neutron spectroscopy with compact cryogenic spectrometers with high-energy resolution, broadband efficiency, and a simple response function. The instruments have, for example, the potential to detect light elements in actinide matrices through their nuclear scattering resonances or to identify the neutron scattering signatures of low-Z compounds.

High energy resolution cryogenic detectors are finding applications in laboratory or other controlled settings for the detection of fast neutrons. The resolution of these devices can enable the identification of neutron sources and possible also the source's chemical form and its surrounding shielding by observation of absorption and transmission resonances.

Direct measurement of the kinetic energy of the neutron with ^{10}B and ^{6}Li-loaded compounds can be inferred trough the response matrix of the neutron absorber. Due to the complex nature of neutron interaction in the absorber and in the surrounding materials, the deconvolution of the experimental spectra is aided by Monte Carlo simulations.

Although not likely to become field instrument, the spectrometer can be made transportable, and improvements in refrigeration techniques, such as the use of mechanical pulse tube coolers to replace the liquid cryogens may well further that end.

The use of fast digital signal processors with algorithms that can process piled-up pulses on-line will increase the count rate of the instrument to ~ 100 counts/s per pixel. When combined with an array of neutron detectors, the neutron spectrometer should be able to reach count rates of at least 1000 counts/s in the MeV range, with no degradation in

energy resolution. This will further increase the sensibility of the instrument and increase the range of applications.

Bibliography

[Ahl 80] S. P. Ahlen, *Rev. Mod. Phys.* **52**, 121-173 (1980)

[Ajz 88] F. Ajzenberg-Selove, *Nuc. Phys. A* **490,** 1-225 (1988)

[Ake 04] D. S. Akerib et al. (CDMS Collaboration), *Phys. Rev. Lett.* **93** (21) (2004)

[Alb 97] D. F. Albright, W. Berkhout, *Plutonium and Highly Enriched Uranium 1996: World Inventories, Capabilities and Policies,* Stockholm International Peace Research Institute, Oxford University Press, (1997)

[Ali 05] Z. A. Ali, O. B. Drury et al., *IEEE T. Appl. Supercon.* **15** (2): 526 (2005)

[And 42] D. H. Andrews, W. F. Brucksch et al. *Phys. Rev.* **13** 281 (1942)

[And 49] D. H. Andrews, R. D. Fowler et al. *Phys. Rev.* **76** 154 (1949)

[And 70] A. C. Anderson, R. E. Peterson, *Cryogenics* **10**, 430 (1970)

[Bar 57] J. Bardeen, L. N. Cooper, J. R. Schrieffer, *Phys. Rev.* **106**, 162 (1957)

[Bei 03] P. Beiersdorfer, *Annu. Rev. Astron. Astrophys.* **41**: 343-390 (2003)

[Bel 05] Z. Bell, S. A. Carpenter, S. S. Cristy, et al., *Phys. Stat. Sol. (C)* **2**, No. 5, 1592–1605 (2005)

[Bet 30] H. A. Bethe, *Ann. Phys.* (Leipz.) **5**, 325 (1930)

[Bir 64] J. B. Birks, *The Theory and Practice of Scintillation Counting*, Macmillan, New York, 1964

[Bör 93] H. G. Börner, J. Jolie, *J. Phys. G: Nucl. Part. Phys.* **19** 217-248 (1993)

[Bri 93] J. F. Briesmeister (Ed.), Report LA-12625-M, Los Alamos National Laboratory, (1993)

[Bro 02] F. D. Brooks, H. Klein, *Nucl. Inst. Meth. A* **476** 1-11 (2002)

[Bro 85] W. E. Bron, (Ed.), *Nonequilibrium Phonon Dynamics*, NATO ASI Series, Series B: Physics Vol. 124, Plenum Press, New York, (1985)

[Bue 94] M. Buehler, E. Umlauf, J. C. Mather, *Nucl. Inst. Meth.* **346**, 225 (1994)

[Cat 67] A.L. Catz, S. Amiel, *Nucl. Phys. A* **92** 222-232(1967)

[Cha 81] M. M. Chaudhri, J. K. Wells, A. Stephens, *Phil. Mag. A* **43** (3), 643-664 (1981)

[Cha 32] J. Chadwick, *Proc. R. Soc.* (London) **136** 692 (1932)

[Che 02] G. Chen, R. Lanza, *IEEE Trans. Nucl. Sci*. **49** (4), 1919-1924 (2002)

[Cho 00] D. T. Chow, M. A. Lindeman, et al. *Nucl. Instrum. Meth. A* **444** 196-200 (2000)

[Cho 01] D. T. Chow, M. L. van den Berg et al. *IEEE T. Appl. Supercon*. **11** (1): 743-746 (2001)

[Cie 83] S. Cierjacks (Ed.), *Neutron Sources for Basic Physics and Applications*, Pergamon Press, (1983)

[Cla 04] J. Clarke, A. I. Braginski (Eds.), *The SQUID Handbook Vol. 1 - Fundamentals and Technology of SQUIDs and SQUID Systems*, Wiley-VCH Verlag GmbH (2004)

[Cod 99] J. A. Coderre, G. M. Morris, *Radiat. Res.* **151** (1): 1-18 (1999)

[Col 98] N. Colonna, G. Tagliente, *Nucl. Instrum. Meth. A* **416** 109 (1998)

[Cun 02] M. F. Cunningham, J. N. Ullom et al. *Appl. Phys. Lett.* **81**, 159 (2002)

[Cur 03] P. Curie, A. C. Laborde, *R. Hebd. Séanc. Acad. Sci. Paris* **136**, 673-675 (1903)

[Dru 84] A. Drukier, L. Stodolsky, *Phys. Rev. D*, **30** 11 (1984)

[Dud 76] J. J. Duderstadt, L. J. Hamilton, *Nuclear Reactor Analysis*, John Wiley & Sons, (1976)

[Dzo 04] S. N. Dzhosyuk, C.E. H. Mattoni, D. N. McKinsey, et al. *Nucl. Instrum. Meth. B* **217** 457-470 (2004)

[Ell 48] R. G. Elliott, R. E. Bell, *Phys. Rev.* **74** 12 (1948)

[END 06] Evaluated Nuclear Data Files (ENDF/B-VI.8) from National Nuclear Data Center, Brookhaven National Laboratory, http://www.nndc.bnl.gov/

[Eva 77] A. G. Evans, T. R. Wilshaw, *J. Mater. Sci.* **12**, 97-116 (1977)

[Fab 03] Ch. W. Fabjan, F. Gianotti, *Rev. Mod. Phys.* **75**, (2003)

[Fir 96] R. B. Firestone, V. S. Shirley, *Table of Isotopes*, 8th Ed. Wiley, New York, (1996); also see http://ie.lbl.gov/toi/

[Fri 01] S. Friedrich, O. B. Drury et al. *Nucl. Inst. Meth. A* **467**, 1117 (2001)

[Fyn 03] H. O. U. Fynbo, *Nucl. Inst. Meth. B* **207** 275-282 (2003)

[Goo 85] M.W. Goodman, E. Witten, *Phys. Rev. D*, **31** 12 (1985)

[Goe 39] A. Goetz, *Phys. Rev.* **55,** 1270–1271 (1939)

[Goz 95] T. Gozani, *Nucl. Inst. Meth. B* **99** 743-747 (1995)

[Hau 06] I. D. Hau, T. Niedermayr, O. B. Drury et al., *Nucl. Inst. Meth. A* **559** 745-747 *(*2006*)*

[Hau 74] U. Hauser, W. Neuwirth, W. Pietsch et al., *Z. Physik* **269**: 181-188 (1974)

[Hit 06] http://www.hitachi-metals.co.jp/e/prod/prod02/p02_22.html

[Hoh 99] J. Hohne, M. Altmann, G. Angloher et al., *X-ray Spectrom.,* **28**, 396 (1999)

[Hol 73] C. E. Holcombe et al., *High Temp. Sci.* **5**, 349 (1973)

[Hol 98] W. Holmes, J. M. Gildemeister et al., *Appl. Phys. Lett.* **72** (18): 2250 (1998)

[How 81] R. J. Howerton, *Thresholds and Q-values of Nuclear Reactions Induced by Neutrons, Protons, Deuterons, Tritons,* ^{3}*He ions, Alpha Particles and Photons,* Lawrence Livermore National Laboratory report UCRL-50400, V24 (1981)

[Irw 95] K. D. Irwin, *Appl. Phys. Lett.* **66**, 1998 (1995)

[Irw 96] K. D. Irwin, Ph.D. Thesis, Stanford University, (1996)

[Kit 99] C. Kittel, *Introduction to Solid State Physics*, 5th Ed. J. Wiley & Sons, New York, 1999

[Kno 99] G. F. Knoll, *Radiation Detection and Measurement*, 3rd Ed., John Wiley & Sons, New York, (1999)

[Kub 00] M. K. Kubo, Y. Sakai, *J. Nucl. Rad. Sci.,* **2** (1), 83-85, (2000)

[Lak 06] http://www.lakeshore.com/temp/sen/smindex.html

[Lam 66] J. R. Lamarsh, *Introduction to Nuclear Reactor Theory*, Addison-Wesley (1966)

[Lan 05] B.E. Lang, M.H. Donaldson et al., *J. Nucl. Mater.* **347,** 125-133 (2005)

[Lee 98] S. F. Lee, J. M. Gildemeister et al*., J. Appl. Optics* **37** (16): 3391-3397 (1998)

[Lid 99] D. R. Lide (Ed.), *CRC Handbook of Chemistry and Physics*, CRC Press, New York (1999)

[Lin 00] M. A. Lindeman, Ph.D. Thesis, University of California, Davis, (2000)

[Lin 63] J. Lindhard, M. Scharff, H. E. Schiott, *Mat. Fys. Medd. Dan. Vid. Selsk.* **33**, 1 (1963)

[Lou 74] O. V. Lounasmaa, *Experimental Principles and Methods Below 1 K*, Academic, London, (1974)

[Lov 95] R. Loveman, J. Bendahan, T. Gozani et al., *Nucl. Inst. Meth. B* **99** 765-768 (1995)

[Low 61] F. J. Low*, J. Opt. Soc. Amer*., **51**, 11 (1961)

[Mag 98] M. Magara, C, Yonezawa, *Nucl. Inst. Meth. A* **411** 130-136 (1998)

[Mar 00] J. M. Martinis, G.C. Hilton, K.D. Irwin et al., *Nucl. Inst. Meth.* **444**, 23-27 (2000)

[Mar 93] P. de Marcillac, N. Coron et al., *Nucl. Inst. Meth. A* **337**, 95-100 (1993)

[Mat 82] J. C. Mather, *Appl. Optics*, **21**, 1125 (1982)

[Mos 84] S. H. Moseley, J. C. Mather, D. McCammon, *J. Appl. Phys.* **56**, 1257 (1984)

[Neu 75] W. Neuwirth, W. Pietsch, W. Richter et al., *Z. Physik* **275** (3): 209-214 (1975)

[Nie 04] T. Niedermayr, I. D. Hau, T. Myiazaki et al., *Nucl. Inst. Meth.* **520**, 70 (2004)

[Peu 00] A. J. Peurrung, *Nucl. Inst. Meth. A* **443**, 400-415 (2000)

[Pic 06] http://www.picowatt.fi/

[Pob 96] F. Pobell, *Matter and Methods at Low Temperatures*, 2nd Ed., Springer Verlag, Berlin (1996)

[Pol 04] V. Polushkin, *Nuclear Electronics: Superconducting Detectors and Processing Techniques*, J. Wiley & Sons, Ltd. (2004)

[Poz 03] S. A. Pozzi, E. Padovani, M. Marsegura, *Nucl. Inst. Meth. A* **513/3** 550-558 (2003)

[Pre 87] K. Pretzl, N. Schmitz, L. Stodolsky (Eds.). *Low-Temperature Detectors for Neutrinos and Dark Matter*, Springer, Berlin (1987)

[Pro 95] F. Pröbst, M. Frank, S. Cooper et al., *J. Low Temp. Phys.* **100**, 69 (1995)

[Rei 91] D. Reilly, N. Ensslin, H. Smith, Jr., (Eds.) *Passive Nondestructive Assay of Nuclear Materials,* NUREG/CR-5550, LA-UR-90-732, U.S. Nuclear Regulatory Commission, Washington D.C. (1991)

[Sad 99] B. Sadoulet, *Nucl. Phys. B-Proc Sup* **77**: 389-397 (1999)

[Sak 94] Y. Sakai, C. Yonezawa et. al., *Nucl. Inst. Meth. A* **353** 699-701(1994)

[Sak 96] Y. Sakai, C. Yonezawa et. al., *Radiochimica Acta* **72**, 45-49 (1996)

[Shu 00] J. K. Shultis, R. E. Faw, *Radiation Shielding*, American Nuclear Society (2000)

[Sil 02] C. S. Silver, J. Beeman, et al., *Nucl. Inst. Meth. A* **485**, 615-623 (2002)

[Sim 35] F. Simon, *Nature* **135** 173 (1935)

[Sup 06] www.suparacon.com

[Tay 97] J. R. Taylor, *An Introduction to Error Analysis*, 2nd Ed., University Science Books, Sausalito, CA (1997)

[Ter 04] S. Terracol, T. Miyazaki, U. Morita et al., *Nucl. Inst. Meth. A* **520** (1-3): 300-302 (2004)

[Tha 67] P. D. Thacher, *Phys. Rev.* **156** (3), 975-988 (1967)

[Tin 04] M. Tinkham, *Introduction to Superconductivity*, 2nd Ed., Dover Publications, (2004)

[Ull 03] J. N. Ullom, M. R. Cunningham, T. Miyazaki et al*., IEEE Trans. Appl. Supercond.* **13** (2): 643-648 (2003)

[Wol 00] D. A. Wollman, S. W. Nam,et al., *Nucl. Instr. Meth. A,* **444**, 145, (2000)

[XCO 06] XCOM: Photon Cross Sections Database, NIST Standard Reference Database 8 http://physics.nist.gov/PhysRefData/Xcom/html/xcom1.html

[Zie 77] J. F. Ziegler, *The Stopping and Ranges of Ions in Matter*, Pergamon Press, New York, (1977)